REVIEW

Check for updates

Opportunities and challenges for emerging inorganic chalcogenide–silicon tandem solar cells†

Vijay C. Karade, [iD] [ab] Mingrui He,[c] Zhaoning Song, [iD] [a] Abasi Abudulimu,[a] Yeonwoo Park,[b] Donghoon Song, [iD] [de] Yanfa Yan, [iD] [a] Jin Hyeok Kim, [iD] [f] Randy J. Ellingson,[a] Jae Ho Yun,*[b] Xiaojing Hao,[c] Seung Wook Shin*[g] and Mahesh P. Suryawanshi [iD] *[c]

This review highlights the promise of emerging inorganic chalcogenide–silicon (Si) tandem solar cells (TSCs) to overcome the power conversion efficiency (PCE) and long-term stability limitations of single-junction solar cells, advancing them toward early commercialization. First, we cover the fundamentals of TSCs, including basic concepts, design considerations, and key requirements. The unique optoelectronic properties of proven and emerging chalcogenide absorber materials are then thoroughly examined to evaluate whether they are suitable candidates for the top cell in tandem configurations. Furthermore, we highlight the critical factors that limit PCE when compared to III–V-, Si-, and perovskite-based tandem and single-junction solar cells. In light of limitations, we discuss the challenges and solutions for the fabrication process, device performance, long-term stability, and outdoor testing of chalcogenide–Si TSCs. Finally, we provide perspectives on future research directions and potential pathways for the early commercialization of these emerging inorganic chalcogenide–Si tandem technologies.

Broader context

Photovoltaics (PV) offers a promising solution to the challenges of replacing traditional fossil fuel with renewable energy and increasing energy demands in the near future. Although various single-junction PVs (*i.e.*, Si) are widely installed in the world, their power conversion efficiency (PCE) faces the theoretical limitation. In this regard, tandem solar cells (TSCs) are attractive for new pathways to overcome these limitations. Unfortunately, the well developed III–V-Si and perovskite-Si TSCs have critical issues such as elemental scarcity, high costs, instability in an air atmosphere, and toxicity despite their high PCE. On the other hand, emerging inorganic metal–chalcogenide materials have excellent advantages as the top cell in TSCs, including cost-effectiveness, non- or lower-toxicity, tunable and excellent optoelectronic properties, and long-term stability in an air atmosphere. However, few investigations of emerging inorganic metal chalcogenide-Si TSCs have been reported. This review addresses a significant gap in the literature by providing a comprehensive overview of the advancements, potential, and challenges of using emerging inorganic chalcogenide materials as a top cell in Si-based tandem solar cells.

1. Introduction

The growing global demand for renewable energy necessitates continuous advancements in solar cell (SC) technologies and the photovoltaic (PV) market. Over the years, significant progress has been made in highly efficient single-junction SCs (*e.g.*, silicon (Si), CdTe, and Cu(In,Ga)Se$_2$ (CIGSe)), enabling them to convert sunlight into useful energy more effectively.[1,2]

[a] *Department of Physics and Astronomy and Wright Center for Photovoltaics Innovation and Commercialization, The University of Toledo, 2801 W. Bancroft Street, Toledo, OH, 43606, USA*

[b] *Department of Energy Engineering, Korea Institute of Energy Technology (KENTECH), Naju 522132, Republic of Korea. E-mail: jhyun@kentech.ac.kr*

[c] *School of Photovoltaic and Renewable Energy Engineering, University of New South Wales, Sydney, New South Wales 2052, Australia. E-mail: m.suryawanshi@unsw.edu.au*

[d] *Department of Chemical Engineering, Sunchon National University, Suncheon 57922, Republic of Korea*

[e] *School of Materials Science and Engineering, Georgia Institute of Technology, North Ave NW, Atlanta, Georgia 30332, USA*

[f] *Optoelectronics Convergence Research Center and Department of Materials Science and Engineering, Chonnam National University, Gwangju 61186, Republic of Korea*

[g] *Future Agricultural Research Division, Rural Research Institute, Korea Rural Community Corporation, Ansan-si 15634, Republic of Korea. E-mail: swshin1211@gmail.com*

This journal is © The Royal Society of Chemistry 2025

Energy Environ. Sci., 2025, **18**, 6899–6933 | **6899**

However, these conventional single-junction SCs, have a theoretical maximum power conversion efficiency (PCE) limit of around 33.7% for a band gap energy (E_g) of 1.34 eV.[3] To overcome this limitation, "tandem SCs (TSCs)" have emerged as a promising solution, utilizing multiple absorber layers, each optimized for a specific range of the solar spectrum.[4,5] In tandem configurations, the top cell has a wider E_g, with each subsequent cell having a progressively narrower E_g,[6] enabling the better utilization of sunlight and hence higher PCE. In this regard, TSCs offer the potential to overcome the PCE limits of single-junction SCs and drive solar energy technology to new heights.[7]

Currently, commercialized III–V-based TSCs (GaAs-based compounds) have excellent PCEs of 47.1%.[8] However, their high costs and complex manufacturing processes prevent scale production.[9] In this context, perovskite (PSK)-based TSCs, such as PSK-Si, PSK-inorganic (*i.e.*, CIGSe or CdTe), and PSK–PSK, are attracting attention because of their high PCE, low cost, process compatibility, and tunable E_g.[10–15] To date, the highest reported PCE for two-terminal (2T) and four-terminal (4T) PSK-CIGSe TSCs are approximately 24.6[16] and 29.9%,[17] respectively. In contrast, PSK-Si TSCs have achieved much higher PCEs of 34.6% (2T) and 30.35% (4T).[18–20] This demonstrates that Si is the most suitable bottom absorber material due to its low cost, reliability (minimum 80% warranty with initial peak performance lasting up to 30–35 years), and well-established commercial fabrication process.[21–24] However, there are substantial

Vijay C. Karade

Dr Vijay C. Karade is currently a postdoctoral researcher at the University of Toledo, affiliated with the Department of Physics and Astronomy and PVIC. His research focuses on chalcogenide-based thin-film photovoltaics and tandem solar cells. He earned his Ph.D. in Materials Science and Engineering from Chonnam National University, South Korea, specializing in kesterite-based solar cells, and later pursued postdoctoral research at KENTECH on CIGS-perovskite tandem cells. With expertise in thin-film deposition, device fabrication, and performance optimization, he works to advance next-generation solar technologies.

Jae Ho Yun

Prof. Jae Ho Yun is currently a professor in the Department of Energy Engineering at KENTECH, South Korea. Previously, he served as the director of the PV division at the Korea Institute of Energy Research (KIER), where he pioneered solar cells, modules, and system technologies. During his tenure, he developed world-class flexible thin-film solar cells and successfully transferred them to industry. He has founded multiple research-based spin-off companies and currently focuses on high-efficiency flexible tandem solar cells and next-generation photovoltaic systems for distributed renewable energy. His work advances carbon neutrality and sustainable energy solutions.

Seung Wook Shin

Dr Seung Wook Shin is a senior researcher professor at the Rural Research Institute, Korea Rural Community Corporation. His work focuses on the synthesis and characterization of inorganic energy conversion materials and their applications, including thin-film solar cells and photoelectrochemical water-splitting devices.

Mahesh P. Suryawanshi

Dr Mahesh P. Suryawanshi is an ARC DECRA Fellow and lecturer at the School of Photovoltaic and Renewable Energy Engineering, UNSW Sydney. He has received multiple prestigious awards, including a Doctoral Exchange Scholarship (2012), the Brain-Korea (BK-21) Postdoctoral Fellowship (2016–2019), the Early Career Researcher Award (2019–2021) from Ministry of Spain and the European Commission, and the Australian Research Council's Discovery Early Career Researcher Award (DECRA) (2021–2024). Since 2021, he leads a research group that focuses on the nanoscale design and development of functional materials, exploring their structure-optoelectronic properties through experiments and modeling for solar energy conversion and catalysis applications.
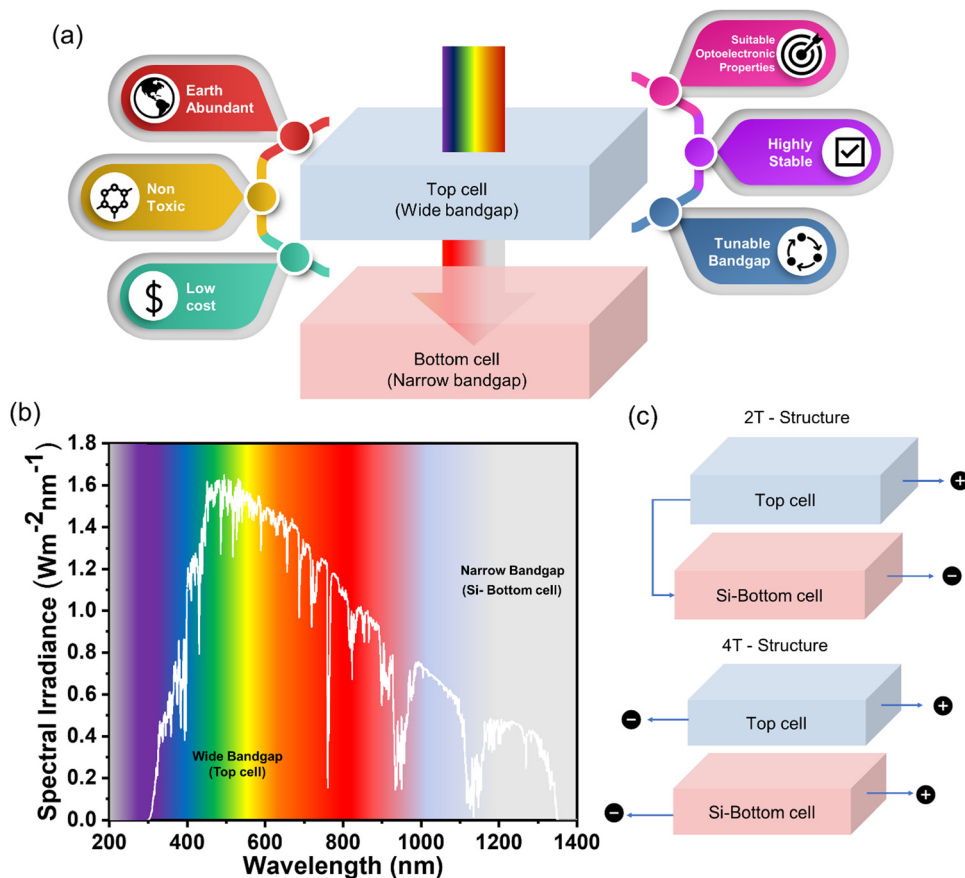
6900 | *Energy Environ. Sci.*, 2025, **18**, 6899–6933

This journal is © The Royal Society of Chemistry 2025

Fig. 1 (a) Schematic of a TSC consisting of emerging chalcogenide-based wide E_g absorber layer as top cell and narrow E_g bottom cell (*i.e.*, Si), (b) spectral irradiance under AM 1.5G for narrow E_g top cell and Si bottom cell for tandem configuration and (c) schematic of connection in 2T and 4T chalcogenide top cell-Si device structure.

concerns about the long-term stability and reliability of PSK-Si-based TSCs, notably light-induced phase segregation in bromine (Br)-rich PSKs.[25,26] More critically, the high PCE PSK SCs contain lead (Pb), which severely limits their future commercialization. Despite several attempts to address this issue, effective strategies remain inadequate. Exploring alternative materials and strategies is crucial for overcoming these constraints and realizing the full potential of TSCs.

The inorganic chalcogenide absorber materials offer intrinsic long-term stability and durability, making them attractive candidates for top cells in Si-based TSC development.[27,28] These materials have excellent optoelectronic properties, tunable E_g, and high thermal, chemical, and environmental stability, making them suitable for long-term solar energy harvesting applications (Fig. 1(a)).[27–30] CIGSe and CdTe single-junction SCs with E_g (1.1–1.5 eV) have achieved PCEs of over 23% and are commercially available.[19,31] However, the scarcity of indium (In), gallium (Ga), and tellurium (Te), as well as the toxicity of cadmium (Cd) necessitates the development of new chalcogenide-based absorber materials that use low-cost, less toxic, and earth-abundant elements.[28,29,32] Integrating these emerging absorber materials with Si SCs offers promising solutions to the limitations of current TSC configurations. To produce high PCE TSCs, the top cell should have an E_g of

1.6–2.0 eV with PCE of >16% to exceed the 25% PCE mark of single junction Si SCs.[33] However, the current highest PCEs reported for emerging inorganic wide E_g SCs such as Cu(In,Ga)S$_2$ (CIGS) and CuGaSe (CGSe) are 16.9 and 11.9%,[34] respectively, which fall short of the requirements, whilst others have achieved PCEs of 10% or lower.[28,29,31,35] Despite promising results, there have been few research articles and reviews on inorganic chalcogenide–Si TSCs published.

This comprehensive review highlights the current state of the art in emerging inorganic chalcogenide–Si TSCs, with a focus on fabrication, high PCE, and long-term stability challenges. We highlight advancements and challenges in III–V, PSK, CIGSe, and Si-based TSCs, as well as the optoelectronic properties of proven and emerging chalcogenide absorber materials. Moreover, we discuss current achievements, challenges, and opportunities for chalcogenide–Si TSCs. Finally, we provide perspectives and further research directions for the early commercialization of these promising emerging inorganic chalcogenide–Si TSCs technologies.

2. Principles of TSCs

The tandem concept is designed on the principle of maximum utilization of light, where the carrier losses caused by the

This journal is © The Royal Society of Chemistry 2025

Energy Environ. Sci., 2025, **18**, 6899–6933 | **6901**

thermalization process and absorption loss below the E_g can be minimized.[36,37] Briefly, it can be achieved by integrating or stacking two or more absorber layers on top of each other with different E_g values, typically wider at the top and narrower at the bottom (Fig. 1(b)). In the case of chalcogenide–Si TSCs, the wide E_g chalcogenide absorber layer can absorb high-energy photons (typically ultraviolet visible (UV) region) from the solar spectrum, while transmitting low-energy photons (i.e., visible-infrared) efficiently harvested by the Si bottom cell (Fig. 1(b)). Generally, TSC configurations are categorized based on terminal configuration and integration techniques, such as 2T and 4T.[7] In 2T configuration, the top cell is directly fabricated over the bottom cell, which allows a direct series connection of two sub-cells, whereas in 4T top cell is fabricated independently and stacked over the bottom cell (Fig. 1(c)). They are optically coupled but are electrically isolated. In 2T TSCs, the current matching is required as the same current flows through the two sub-cells connected in series, while in 4T it is not required as they are electrically isolated. Theoretically, both 2T and 4T Si-based TSCs with an E_g of 1.1–1.2 eV can achieve PCEs > 45%.[38]

For a sustainable future, TSCs must exhibit commercial viability, scalability, ease of processing, low cost, and use earth-abundant and non-toxic elements.[2,39] They must be robust against environmental conditions such as temperature and humidity, ensuring long-term performance stability. Moreover, while fabricating the TSC devices, interconnecting techniques, optical design, E_g, stacking orders, and fabrication process must be seriously considered.[7,40] Particularly, there must be a suitable recombination layer (RL) to enable efficient charge transport between the monolithically integrated top and bottom cells, while maintaining light management features like anti-reflection (AR), surface texturing, and plasmonics.[41,42] Choosing a suitable E_g and device configuration allows for the realization of maximum tandem efficiency.[6,37] The low defect density in the top absorber layer is also crucial, along with achieving maximum current density and voltage (J–V) output through proper serial electrical interconnection between the two cells.[43] Additional details on E_g selection, current matching criteria, and the foundation of TSCs can be found in earlier reports,[5–7,44] and a detailed discussion concerning chalcogenide top cells can be found in Section 5.

3. Promising chalcogenide absorber materials

This section reviews the unique optoelectronic properties and recent progress of single-junction SCs in proven wide E_g chalcogenides, including CIGS, CGSe, CuInS$_2$, Cu$_2$ZnSn(S,Se)$_4$ (CZTSSe), and Sb$_2$(S,Se)$_3$. Additionally, it covers emerging inorganic chalcogenide compounds such as SnS, GeSe, AgBiS$_2$, CuBi(S,Se)$_2$, BaZrS$_3$, SrZrS$_3$, and Ba$_3$ZrS$_7$. A summary of their optoelectrical properties and device parameters is provided in Tables 1 and 2.

3.1. Proven shalcogenides

3.1.1. Stibnite: (Sb$_2$(S,Se)$_3$). Stibnite-based Sb$_2$(S,Se)$_3$ exhibits an orthorhombic and highly anisotropic structure that carries unique optoelectronic properties.[27,61] It benefits from a binary composition that minimizes phase segregation and defect complexity, contributing to its structural and chemical stability.[61] Structurally, both Sb$_2$S$_3$ and Sb$_2$Se$_3$ features unique (Sb$_4$S(e)$_6$) ribbons-like configuration, with 1D ribbons along the [001] orientation (Fig. 2(a)). This anisotropic property enables efficient charge carrier transport along the ribbon axis, while transport among adjacent ribbons occurs via hopping mechanisms.[62,63] Consequently, films oriented along non-zero hkl ($hk1 \neq 0$) planes have demonstrated higher PCEs than those oriented along hkl = 0 planes.[64] One of the key advantages of Sb$_2$S$_3$ is the presence of stereochemical active lone-pair electrons, which significantly influence its electronic structure and lead to a high absorption coefficient >10^5 cm^{-1} (see Table 1).[27] It exhibits quasi-direct-indirect E_g transition between 1.6–1.7 eV and it occurs with approximately 0.08 eV.[65,66] Through Se incorporation, the E_g can be tuned from 0.9–1.0 eV (pure Sb$_2$Se$_3$) to 1.6–1.7 eV (pure Sb$_2$S$_3$), making it highly suitable for TSCs applications.[27] It can be synthesized using various deposition techniques, including chemical bath deposition (CBD), hydrothermal, spin coating, thermal evaporation (TE), atomic layer deposition (ALD), and spray pyrolysis.[67–71] Among them, the recent report based on a multi-sulfur source-based CBD technique demonstrated nearly 8% PCE for the Sb$_2$S$_3$ single-junction SCs.[67] Utilization of a multi-sulfur source expedited the bath reaction and hydrolysis process and thereby overall absorber quality including its optoelectronic properties. Similarly, a modified hydrothermal deposition of Sb$_2$S$_3$ in the

Table 1 Summarized fundamental optoelectronic properties of proven and emerging inorganic chalcogenides-based compounds. (Band gap energy: E_g, indirect E_g: *, Direct E_g: **, absorption coefficient: α, carrier concentration (acceptor): N_A, minority carrier lifetime (electron): τ_n, carrier mobility (hole): μ_h, conductivity (hole): σ_h)

Materials	Crystal structure	E_g (eV)	α (cm^{-1})	N_A (cm^{-3})	τ (ns)	μ_h (cm^2 V^{-1} s^{-1})	σ_h (S cm^{-1})
CIGS(e)[45,46]	Chalcopyrite	1.0–1.7**	10^4–10^5	10^{14}–10^{18}	20–50	10–100	1–10^{-2}
CZTS(e)[47]	Kesterite	1.0–1.5**	10^4–10^5	10^{14}–10^{18}	5–10	7	10^{-2}–10^{-3}
Sb$_2$S(e)$_3$[48]	Orthorhombic	1.0–1.7*	10^4–10^5	10^{17}–10^{19}	—	10–42	10^{-5}–10^{-7}
GeS(e)[49]	Orthorhombic	1.14–1.7*	10^4–10^5	10^{17}–10^{19}	—	128	1–10^{-7}
SnS[50,51]	Orthorhombic	1.1**	10^4–10^6	10^{13}–10^{15}	—	10–15	10^{-3}–10^{-1}
AgBiS$_2$[52,53]	Hexagonal Cubic	1.07* 0.8**	10^5–10^7	10^{14}–10^{19}	—	0.07–1.1	0.2–1
NaBiS$_2$[54]	Hexagonal Cubic	1.2–1.5*	10^3–10^4	10^{14}–10^{19}	—	0.03–0.29	10^{-6}–10^{-5}
BaZrS$_3$[55,56]	Hexagonal Cubic	1.3–2.2*	10^4–10^6	10^{17}–10^{20}	—	30–40	2.9

6902 | *Energy Environ. Sci.*, 2025, **18**, 6899–6933

This journal is © The Royal Society of Chemistry 2025

Table 2 Device parameters of champion cells from emerging chalcogenide and established PV technologies along with their E_g. Note: The tabulated data is collected from the reported recent efficiency tables for different PV[31,57–59]

Absorber	E_g (eV)	V_{oc} (mV)	J_{sc} (mA cm^{-2})	FF (%)	PCE (%)
AgBiS$_2$	1.30	518	27.2	72.4	10.2
AgBiS$_2$	1.39	495	27.1	68.4	9.2
CGSe	1.62	1017	17.5	67.0	11.9[34]
CIGS	1.60	954	24.8	71.5	16.9
CIS	1.60	729	21.8	71.7	11.4
CZGS	1.45	625	24.4	55.7	8.5
CZTS	1.55	749	23.4	68.9	13.2
CZTSSe	1.09	530	38.4	74.0	15.1
CZTSSe-Ag	1.10	565	35.4	70.3	14.1
CZTSSe-Ge	1.12	527	32.3	72.3	12.3
GeS	1.70	530	8.30	31.0	1.3
SnS	1.25	339	25.8	55.0	4.8[60]
Sb$_2$(S,Se)$_3$	1.35	551	26.0	70.1	10.1
Sb$_2$(S,Se)$_3$	1.44	631	25.3	67.4	10.8
Sb$_2$(S,Se)$_3$	1.54	673	23.7	66.8	10.7
Sb$_2$S$_3$	1.73	757	17.4	60.5	8.0
Sb$_2$S$_3$	1.80	711	16.1	65.0	7.5
Sb$_2$Se$_3$	1.23	467	33.5	67.6	10.6
Sb$_2$Se$_3$	1.38	474	27.7	62.2	8.1
c-Si	1.11	745	42.3	86.7	27.4
GaAs	1.42	1127	29.8	86.7	29.1
Perovskite	1.53	1193	26.5	84.5	26.7
CdTe	—	904	31.6	80.6	23.1
CIGSe	1.13	767	38.3	80.5	23.6

presence of the ethylenediaminetetraacetic acid disodium salt (Na$_2$EDTA) in combination with SnO$_2$/CdS double buffer layers

delivered 8.26% PCE.[72] Despite these advancements, Sb$_2$S$_3$ still faces challenges related to its relatively high carrier concentrations and defect density which can negatively impact device performance. It has relatively low carrier mobility (0.1–1 cm^2 V^{-1} s^{-1} in Table 1), limiting efficient charge transport, while deep-level defects such as sulfur (S)/ selenium (Se) vacancies or Sb–S/Se antisites which act as non-radiative recombination centers, reducing carrier lifetime. The highest reported PCE to date stands at 10.81% for Sb$_2$(S,Se)$_3$ (E_g = 1.44 eV), highlighting the potential of E_g engineering in optimizing performance.[73] Further efforts in passivation strategies, interface engineering, and composition tuning are necessary for advancing Sb$_2$S$_3$-TSCs.

3.1.2. Chalcopyrite: CIGS and CGSe. Chalcopyrite-based compounds (*i.e.*, CIGSe with E_g of 1.1–1.2 eV) are well-known and commercialized absorber materials for SCs due to their outstanding optoelectronic properties, long-term stability, and remarkable PCE of 23.6%.[57,74] Chalcopyrite-based compounds have a high absorption coefficient $>10^5$ cm^{-1} in visible to near-infrared regions, allowing them to efficiently convert sunlight into electrical energy. Chalcopyrites possess a long minority carrier lifetime greater than 20–30 ns and a high carrier mobility of 10–100 cm^2 V^{-1} s^{-1} (Table 1), allowing efficient carrier transport across the absorber layer. The E_g of the Cu-III-VI$_2$ materials system with chalcopyrite crystal structure (Fig. 2(b)) can be tuned from 1.04 to 1.68 eV by replacing 'In'
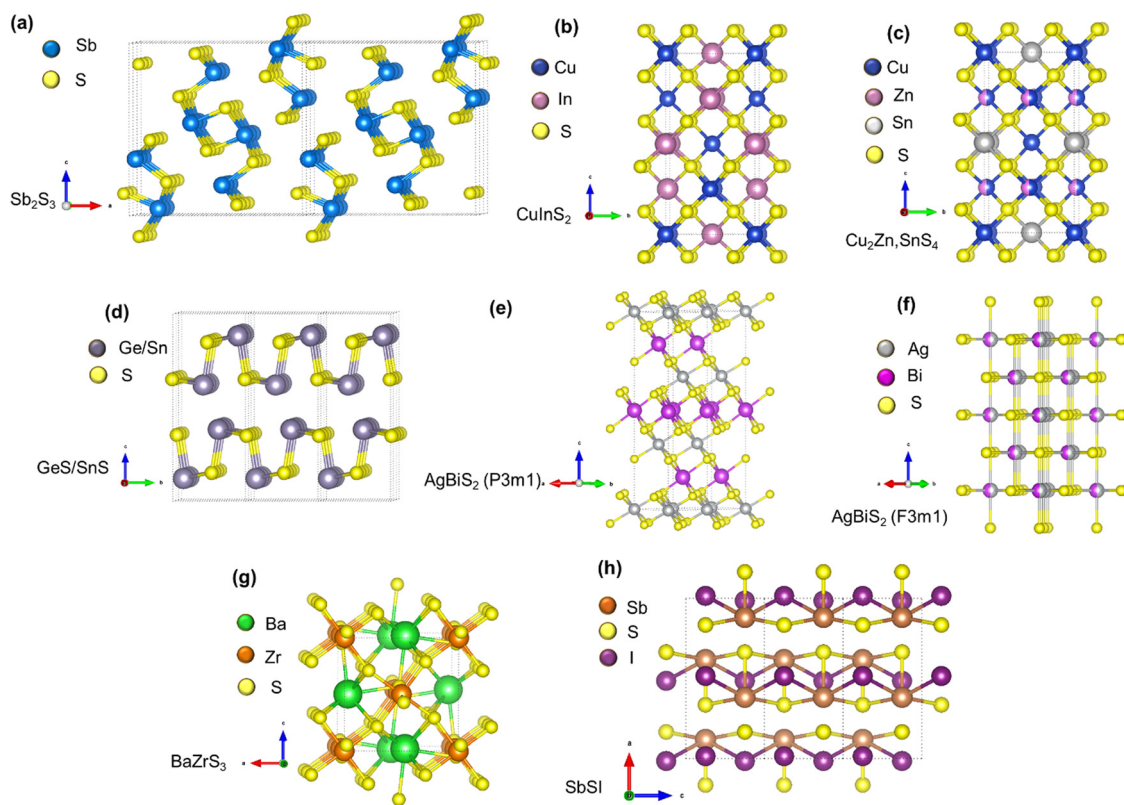

Fig. 2 Atomic crystal structures for the different chalcogenide-based absorber layers, (a) Sb$_2$S$_3$ (*Pnma*), (b) CuInS$_2$, (c) Cu$_2$ZnSnS$_4$, (d) SnS/GeS (*Pnma*), (e) AgBiS$_2$ (*P3m1*), (f) AgBiS$_2$ (*F3m1*), (g) BaZrS$_3$, and (h) SbSI chalcohalaide, respectively. All crystal structures were created with VESTA software based on crystallographic information file from the inorganic crystal structure database (ICSD).

This journal is © The Royal Society of Chemistry 2025

Energy Environ. Sci., 2025, **18**, 6899–6933 | **6903**

with 'Ga' in CuInSe$_2$ to CGSe.[75] With the addition of 'S', it can be further increased to 2.5 eV for CuGaS$_2$. Alternatively, substituting silver (Ag) for copper (Cu) and aluminum (Al) for 'In' opens new pathways for increasing E_g. Nevertheless, chalcopyrite-based single-junction SCs have been extensively studied and well developed; yet the PCE of CIGS and CGSe single-junction SCs with wider E_g is significantly lower than that of others (see Table 2). Shukla and co-workers have reported PCE over 15% with an E_g of 1.6 eV for CIGS single-junction SCs by engineering Cu-composition, using a Zn(O,S) buffer with a higher conduction band (CB) edge, and Ga grading.[76] By benefiting from all these strategies, rare interface recombination gets reduced and the activation energy of recombination gets closer to E_g. It results in much lower interface carrier recombination and open circuit voltage (V_{oc}) loss, delivering over 900 mV of V_{oc}. Ishizuka and co-workers reported CGSe single-junction SCs with >10% PCE by a three-stage co-evaporation process with various metal flux ratios.[77] It was found that Se/Ga flux ratio is critical in determining the properties of the absorber layer, alkali distribution profiles, and device performance.

3.1.3. Kesterite: (CXT(S,Se)$_4$)-based compounds. The chalcopyrite-based compounds with wide E_g have outstanding optoelectronic properties and show high PCE, but the high cost of the rare earth In and Ga elements remains a concern. In this regard, earth-abundant elements-based kesterite compounds have gained enormous attention as promising the next generation light absorber materials. The poplar kesterite-based CZTS(e) compound is derived by replacing group III elements in the CIGS(e) structure with zinc (Zn) and tin (Sn) (see Fig. 2(c)).[78] It exhibits intrinsic p-type conductivity, tunable direct E_g ranging from 1.0 eV for pure Se-based CZTSe to 1.5 eV for pure S-based CZTS, high absorption coefficient >10^5 cm^{-1} in the UV region, carrier mobility of 50 cm^2 V^{-1} s^{-1} as well as three-dimensional symmetry of carrier transport (see Table 1). Unlike CIGSe compounds, CZTS has a relatively higher defect density and related defect clusters owing to the nearly similar ionic radii of Cu$^+$ and Zn^{2+} and its multi-element nature, leading to a shorter minority carrier lifetime (Table 1).[79] In this regard, the current PCE of CZTSSe single-junction SCs with narrow E_g reached only 15.1% using the solution process, which is inferior to that of CIGSe and CdTe single-junction SCs.[31] A recent study utilizing machine learning techniques screened over 1800 compounds and identified around 200 compounds with optical E_g ranging from 1.2 to 2.7 eV.[80] Despite numerous first-principal calculation studies proposing the development of emerging kesterite-based compounds, only a few have been successfully fabricated. Successful fabrication in CXTS involved manganese (Mn), magnesium (Mg), iron (Fe), nickel (Ni), cobalt (Co), barium (Ba), and strontium (Sr) substituted at X = Zn in CZTS giving new absorbers such as Cu$_2$CdSnS$_4$, Cu$_2$MnSnS$_4$, Cu$_2$FeSnS$_4$, Cu$_2$CoSnS$_4$, and Cu$_2$NiSnS$_4$, and replacing 'Sn' with germanium (Ge) and 'Si' in Cu$_2$ZnGeS$_4$ and Cu$_2$ZnSiS$_4$. Hao's group has demonstrated over 11% PCE for the Cu$_2$ZnSnS$_4$ (CZTS) single-junction SCs with E_g = 1.5 eV and V_{oc} of 730 mV with heterojunction heat treatment.[81] It was found that the heat treatment accelerated the elemental inter-diffusion (Cd atoms in CdS buffer occupy Zn or Cu lattice and Na in kesterite), resulting in a favorable band alignment and thereby, reduced non-radiative recombination. Recently, this PCE was further boosted to 13.2% with V_{oc} of 749 mV and a short circuit current density (J_{sc}) of 23.40 mA cm^{-2}.[31] Furthermore, the successfully developed wide E_g kesterite with partially and/or full substitutions such as Ag$_2$ZnSnS$_4$ (6.28%),[82] Cu$_2$CdSnS$_4$ (10%),[83] and Cu$_2$BaSnS$_4$ (2%) have been extensively reported; however, their PCEs are still lower.

3.2. Emerging chalcogenides

3.2.1. Group IV metal binary chalcogenides. In recent years, significant efforts have been made in the development of group IV metal chalcogenides (metal = Ge and Sn, and chalcogen = S and Se) as important candidates for absorbers due to their optimal E_g, high absorption coefficient, earth abundance of constituent elements, and the lack of competing phases.[84–89] These materials exhibit different crystal phases, including hexagonal and orthorhombic structures due to the diverse oxidation states of the constituent metals and chalcogen elements. For instance, Sn-based chalcogenides can manifest as native p-type SnS in an orthorhombic lattice owing to the favorable enthalpy associated with the formation of Sn vacancies, thereby generating shallow acceptors.[90] In this configuration, Sn atoms with an oxidation state of +2 are bonded to three S ions, forming puckered Sn–S layers interconnected by weak van der Waals forces, characterized by the space group *Pnma* (see Fig. 2(d)).[50,91–94] Conversely, Sn–chalcogenides also adopt two-dimensional hexagonal unit cells with Sn in an oxidation state of +4, resulting in a native n-type semiconductor. Each layer in this arrangement comprises a Sn atom monolayer sandwiched between two layers of S atoms, represented by the space group *P3m*1.[95] Furthermore, Ge–chalcogenides, except for GeSe$_2$, exhibit orthorhombic crystal structures (*Pnma*) with a predominant p-type semiconductor behavior.[96] GeSe and SnS, members of the group IV metal chalcogenides family, are considered highly suitable absorbers for TFSCs due to their favorable optoelectronic and structural properties, as well as their simple binary chemical composition, which can be readily controlled during synthesis. Although considerable efficiencies have been achieved for their single junction SCs, namely 4.82% for SnS[60] and ~5.2% for GeSe,[97] there are still numerous challenges that need to be addressed to see their potential as promising absorbers for TFSCs.

3.2.2. I–V–VI$_2$ ternary chalcogenides. I–V–VI$_2$ ternary chalcogenides such as AgBiS$_2$ and NaBiS$_2$ are potential perovskite-inspired compounds that have attracted tremendous interest recently.[98–101] One of the widely investigated materials, AgBiS$_2$ has shown its promise as an absorber in TFSCs due to its outstanding optoelectronic properties, including an optimal E_g of 1–1.3 eV, a high absorption coefficient of 10^5 cm^{-1} and a high mobility of 2.7 cm^2 V^{-1} s^{-1}.[102–104] AgBiS$_2$ exhibits hexagonal and cubic phases, with respective indirect and direct E_g

6904 | *Energy Environ. Sci.*, 2025, **18**, 6899–6933

This journal is © The Royal Society of Chemistry 2025

of approximately 1.07 and 0.8 eV, respectively.[105,106] Among these phases, the hexagonal structure, known as matildite, is particularly promising due to its semiconducting nature and high stability, even at lower temperatures ranging from 25 to 120 °C. Matildite adopts a $P3m1$ with combining macron space group structure and demonstrating notable stability (Fig. 2(e)).[91] Conversely, the cubic phase, referred to as schapbachite, exhibits metallic behavior and possesses a face-centered cubic structure in the $F3m1$ (Fig. 2(f)) with a combined macron m space group, akin to the rock salt metallic structure. Schapbachite remains stable at higher temperatures, while it is metastable at room temperature.[107,108] The cationic and anionic distribution in these materials, explained by Glatz et al.[109] reveals distinct structural characteristics. Matildite exhibits a narrow indirect E_g, making it suitable for PV applications, whereas schapbachite lacks an E_g, rendering it inadequate for such applications. The cationic disorder in $AgBiS_2$ influences its optical properties, particularly the E_g, which can be thermally controlled. The E_g reduction induced by cationic disorder enables tunability in the photoactivity of $AgBiS_2$, making it a promising PV candidate.[99,110,111] Additionally, $AgBiS_2$ exhibits ordered-disordered transitions at the nanoscale under different temperatures, leading to enhanced thermal stability. Additionally, proper tuning of the crystal structure alters the E_g and absorption coefficient, making $AgBiS_2$ an excellent PV absorber.[112,113] The hexagonal structure of $AgBiS_2$ demonstrates superior PV performance over the cubic structure, indicating its potential for achieving high PCE. Recently, Li et al.[114] reported a promising record PCE of 10.2% for $AgBiS_2$-based TFSCs with vapor-assisted sub-micron grain-based thin film. Though further research is needed to explore the electronic and structural properties of $AgBiS_2$ to enhance its PV performance.

Another promising material in this class is $NaBiS_2$, which comprises earth-abundant, cost-effective, and non-toxic elements. $NaBiS_2$ exhibits a high absorption coefficient exceeding 10^5 cm^{-1} at and beyond its pseudo-direct E_g of 1.4 eV.[54,115–117] This leads to a calculated spectroscopic limited maximum efficiency of 26% under 1 Sun illumination conditions.[118] $NaBiS_2$ shares a cation-disordered phase (space group: $Fm3m$) similar to $AgBiS_2$,[119] where Na$^+$ and Bi^{3+} cations can randomly occupy the same crystallographic lattice site due to their similar ionic radii. It has been shown that free electrons and holes generated after photoexcitation could be localized to varying degrees at Bi^{3+}- and Na$^+$-rich clusters, respectively.[118,120] Na$^+$ clusters induce S-3p states just above the valence band maximum (VBM), leading to strong hole localization and the formation of small polarons. Consequently, the sum mobility of $NaBiS_2$ nanocrystal films significantly decreases from 0.29 to 0.03 cm^2 V^{-1} s^{-1} within 1 ps after photoexcitation.[98] These favorable optoelectronic properties of $NaBiS_2$ stem from its high density of states (DOS) in the upper VB and the pseudo-direct nature of the E_g. However, the spectator character of Na$^+$ also results in the formation of localized s–p states above the VBM, particularly at Na$^+$-rich clusters due to an inhomogeneous cation distribution.[98] These localized states cause strong hole

self-trapping, resulting in a slow relaxation process lasting several microseconds, unaffected by post-annealing treatment. Despite the reduction in sum mobility by almost an order of magnitude within a few picoseconds due to charge-carrier localization, the strong absorption and long-lived photogenerated charge carriers suggest the potential use of $NaBiS_2$ in ultrathin single-junction SCs and possibly as top cell absorber materials in Si TSCs.

3.2.3. Chalcogenide PSK. The exploration of lead-free PSK-inspired materials has extended beyond halides to include chalcogenide PSKs such as $BaZrS_3$, $SrZrS_3$, $BaHfS_3$, and $SrHfS_3$, along with Ti-, Zr-, and Hf-based counterparts.[56,121–123] These materials have garnered attention due to their low disorder, with Urbach energies of 18-34 meV,[124] high thermal and environmental stability, and high absorption coefficients ($>10^5$ cm^{-1}).[125] Moreover, chalcogenide PSKs offer promising defect tolerance and E_g typically in the range between 1.6 to 2 eV, making them suitable as top cells in Si-based tandem PVs.[126] Structural variations in chalcogenide PSKs influence BX_6 octahedral connectivity, where corner-sharing BX_6 octahedra define PSK structures.[127] These typically adopt GdFeO$_3$-type (space group Pnma) and YScS$_3$-type (space group $Pna21$) structures, alongside non-PSK configurations with an edge- or face-sharing BX_6 octahedra (Fig. 2(g)).[128,129] While the ABX_3 chemical formula is commonly associated with PSKs, not all such compounds exhibit true PSK crystal structures.

Chalcogenide PSKs also exhibit remarkable light absorption. Their band edges, dominated by sulfur 3p valence and transition metal d conduction states, result in a high joint DOS,[56,124] leading to a rapid absorption coefficient rise ($>10^5$ cm^{-1}) within 0.3–0.5 eV above the onset.[130,131] Comparison with established PV materials shows absorption coefficients up to an order of magnitude higher.[132,133] While charge transport studies remain limited, computational results suggest low effective masses for electrons and holes due to dispersive band edges.[131] Experimentally, electron and hole mobilities of 13.7 and 9.4 cm^2 V^{-1} s^{-1}, respectively, are comparable to other direct E_g inorganic semiconductors,[133–136] indicating their potential for TFSCs, including single-junction and Si-tandem configurations.

3.2.4. Metal chalcohalides. Inspired by the chalcogenide's stability and halide perovskite's excellent optoelectronic properties, a new class of inorganic semiconductors, chalcohalides, has emerged. These materials follow the general formula $M_aX_bY_c$, where M represents metal cations and/or their combinations, X and Y are the chalcogenide and halide anions, and a, b, and c define their composition.[137,138] Common metal cations (M) include Ag, Cu, Sn, Sb, and Pb, while X= S, Se, Te, and Y = Cl, Br, and I. Ag_3SI and Ag_3SBr, among the first reported chalcohalides, were developed as solid electrolytes, though their potential in TFSCs remains unexplored.[139] Theoretically predicated structures such as $Pb_4S_3Br_2$, $Sn_5S_4Cl_2$, $Cd_5S_4Cl_2$, Sn_4SF_6, and Cd_4SF_6, exhibit tunable E_g through halide and chalcogenide composition similar to PSK.[138,140]

Additionally, V–VI–VII pnictogen chalcohalides such as SbSI and BiSI have been investigated for optoelectronic

This journal is © The Royal Society of Chemistry 2025

Energy Environ. Sci., 2025, **18**, 6899–6933 | **6905**

applications.[141] These materials crystallize in an orthorhombic *Pnma* space group, forming a 1D ribbon-like structure along the *c*-axis (Fig. 2(h)). Covalent bonding along the ribbons and weak van der Waals interactions between them yield electronic and carrier transport properties comparable to binary Sb_2S_3.[141,142] BiSY- and SbSY-based chalcohalides exhibit theoretically predicted E_g values of 1.6–1.87 eV and 2.1–2.3 eV, with experimental values of 1.9 and 2.1 eV, except for the iodide variant.[138,140,143,144] SbSI demonstrates high carrier mobility ranging from 50–100 V^{-1} s^{-1} and electrical conductivity 10^{-7} Ω^{-1} cm^{-1}.[145,146] These properties, along with their tunable compositions and structural diversity, position chalcohalides as promising candidates for next-generation optoelectronic and PV applications, including single-junction and tandem SCs.

4. Opportunities and challenges

4.1. Silicon as suitable bottom cells

Si SCs stand as a mature, commercially developed PV technology, and with crystalline Si (c-Si) it dominates the PV market with a substantial share.[147] Homojunction SCs (HJS), Si heterojunction SCs (SHJ), and c-Si based tandems are gaining market momentum, according to the latest report by the International Technology Roadmap for Photovoltaics (ITRPV) (Fig. 3).[148]

Recently, LONGi has set a new world record with 27.3% for heterojunction back contact cells and 22.7% for passivation emitter rear contact (PERC) modules.[149,150] It shows PCE of single-junction Si SCs is approaching the theoretical limit of $\sim 29.4\%$ along with growing production.[151] Despite facing challenges in module PCE and capital expenditure, Si remains a preferred TSC material choice due to its long-term operational stability, developed and scalable processing techniques, the second most abundant element in the Earth's crust, and non-toxicity.[152] Though, some inherent limitations come from spectral losses due to the inability to absorb infrared photons with energy $< E_g$ and thermalization losses of high energy photons, restraining their PCE.[153] The successful integration of Si with wide E_g materials as a top cell offers an opportunity for efficient light harvesting and exceptional performance.

The present section gives a brief overview of technological development in Si-based single-junction SCs. Based on device technology it can be classified into diffusion-based HJS and SHJ. An HJS includes Al back surface field (Al-BSF) cells, PERC, Tunnel Oxide Passivated Contact (TOPCon) and integrated back contact (IBC) as shown in Fig. 4.

Al-BSF. The Al-BSF-based Si-SCs are the first to dominate the Si market in the 21st century. The typical Al-BSF fabrication involves initial cleaning and chemical texturing of the Si wafer, high-temperature diffusion of phosphorous (P) from the
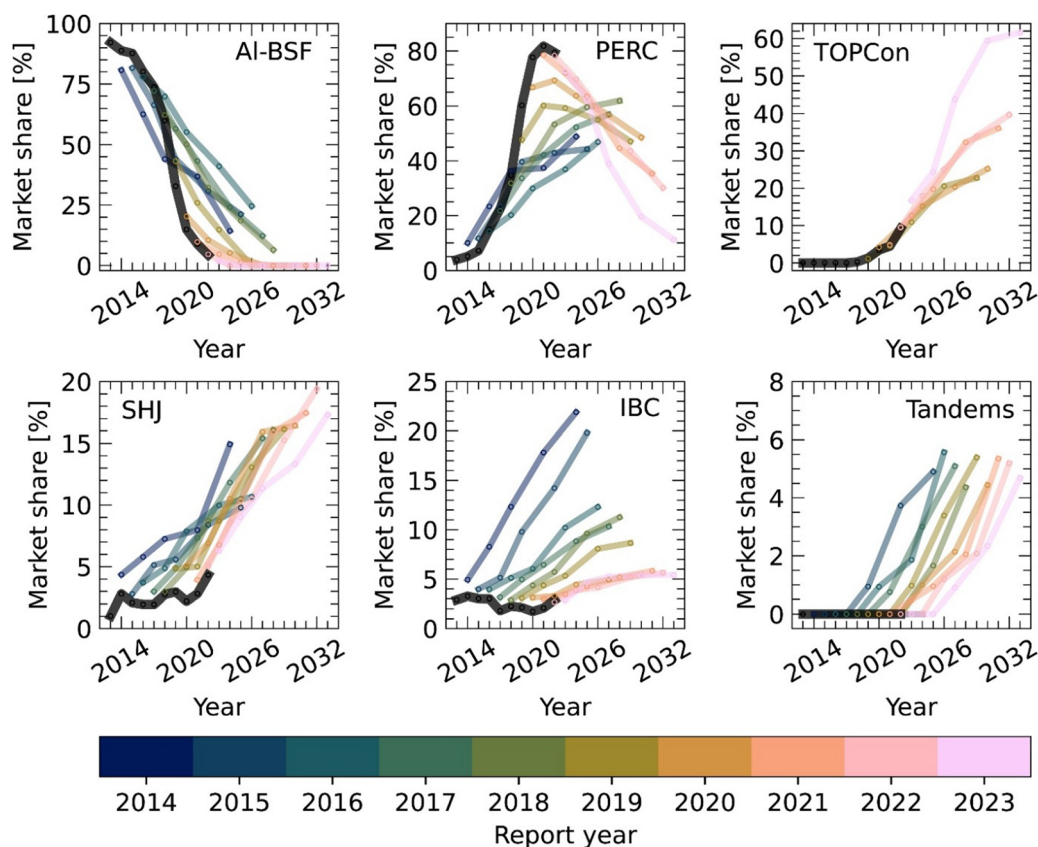

Fig. 3 Predicted market capture of different c-Si SCs technologies based on the annual report produced by the International Technology Roadmap for Photovoltaics (ITRPV).[148] Reproduced with permission, Copyright 2023, Cell press.
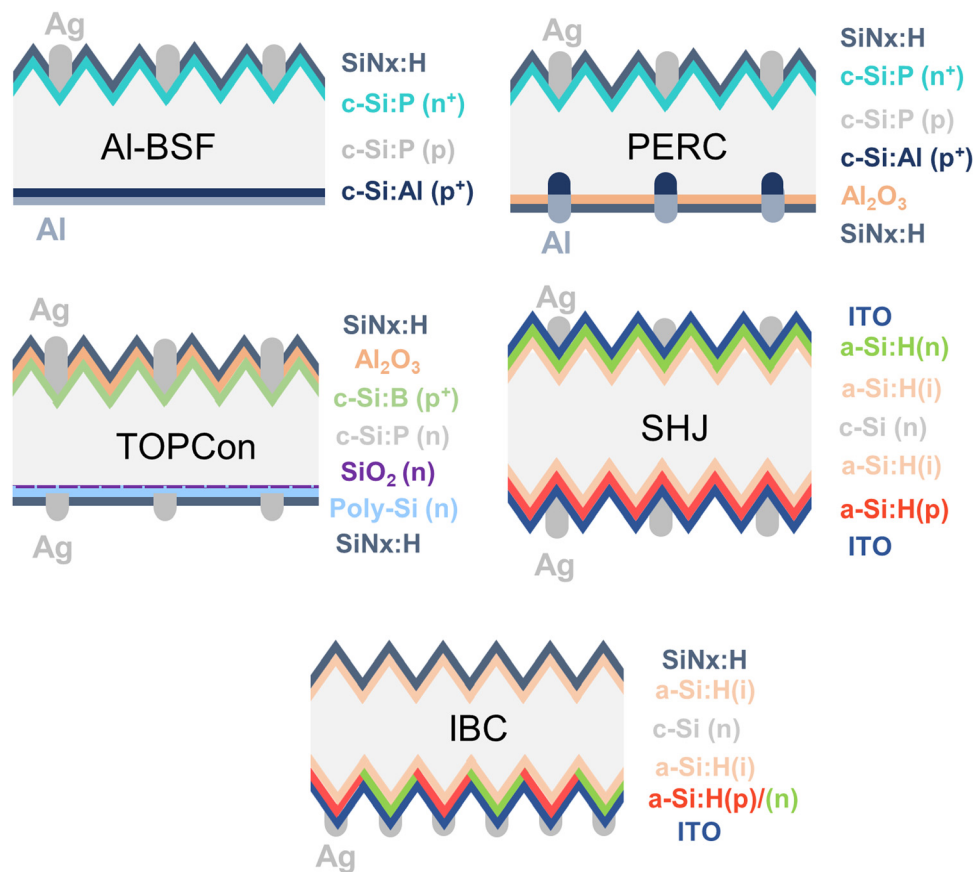
Fig. 4 Different c-Si SCs architectures for Al-BSF, PERC, TOPCon, SHJ and IBC.

emitter, application of hydrogenated silicon nitride (SiN$_x$:H) as passivation and the AR coating layer, and then finally making Ag fingers at the top and fully covered Al back contacts *via* screen printing contact process.[154] The top Al back contact firing process at elevated temperatures (700–800 °C) causes the diffusion of Al$^+$ which acts as a p-type dopant. It creates a p$^+$ surface, which is also referred to as Al-BSF that provides field-effect passivation. During the contact firing process, the Hydrogen (H) gets released from the SiN$_x$:H front region and passivates the bulk as well as surface defects. However, due to the unpassivated back interface and dominant recombination losses, it failed to achieve further higher PCE. The simplicity of the process caused them to dominate the market with a competitive PCE of 20% and V_{oc} about 650 mV reported in 2017.

PERC. PERC technology came with an application of a dielectric passivation layer to overcome the recombination at the rear interface.[155] The divided strip cell and localized contact along with different dielectric passivation layers such as Silicon oxide (SiO$_x$), SiN$_x$, and aluminum oxide (AlO$_x$) provided a further boost in development and PCE. A major breakthrough in PERC came when SiO$_2$ was replaced with AlO$_x$. It creates strong BSF for electrons and strongly repels them to suppress recombination at the back surface. The localized contacts with laser processing, internal reflections, reduced Ag finger size

with low series resistance (R_s), and application of AlO$_x$ BSF layer with plasma enhanced CVD provided PERC technology mass production capacity like Al-BSF while maintaining higher PCE. The major gain in $V_{oc} > 700$ mV and J_{sc} due to reduced recombination at the back with passivation and internal reflection, respectively, delivered a promising PCE of 23% for PERC at the production level. This small technological development in PERC caused a dramatic decline in the recent market share of Al-BSF and a gain for PERC as shown in Fig. 3. However, the PERC SCs suffered V_{oc} loss and stagnated at 700–720 mV. The dominant recombination at the junction, caused by high phosphorus diffusion near the emitter, the direct contact between the metal and Si, and the presence of unpassivated dangling bonds, limits the PCE and V_{oc}.

TOPCon. TOPCon SCs have been developed to overcome the abovementioned challenges through technological advancements in tunneling oxide and passivated back contact. Various thin oxide and metal oxide tunneling layers in combination with polycrystalline Si (poly-Si) efficiently passivate the surface, extract the charge carriers, and remove the need for heavy doping at the rear side. The tunneling layer allows only one type of carrier to pass through it, whereas the poly-Si layer, which is in contact with the metal, pins the Fermi level and effectively reduces the recombination at the rear interface. The TOPCon cells can be fabricated with both p- and n-type wafers,

This journal is © The Royal Society of Chemistry 2025

Energy Environ. Sci., 2025, **18**, 6899–6933 | **6907**

but majorly they are available on n-type which has a tunneling oxide layer and n$^+$ doped poly-Si.[156] The junction is formed by boron (B) doping at the front to create a p$^+$ region, while it is also coated with a dielectric hydrogenated SiN$_x$ layer that acts as an AR coating. The use of c-Si/SiO$_x$ with a well-controlled tunneling oxide layer provides the chemical as well as efficient field effect passivation, delivering ~26% of PCE. Higher minority carrier lifetime enables to achieve >720 mV of V_{oc} with a boost in the fill factor (FF). The TOPCon currently faces challenges with the front recombination coming from the low base doping of B over P.

SHJ. SHJ SCs also possess simple fabrication technology where the hydrogenated amorphous silicon (a-Si:H) provides excellent passivation of dangling bonds at the c-Si/a-Si:H interface. The major technological difference between the SHJ and other HJS is that it does not involve doping in c-Si *via* a thermal diffusion process that forms junctions. So, the carrier separation or selectivity in SHJ is driven by a-Si layers. Consequently, SHJ does not include the metal contact firing process, instead, it has screen-printed contact, putting the overall fabrication well below 250 °C. Furthermore, it exhibits a hydrogenated intrinsic Silicon (i-Si:H) with a-Si:H which passivates the dangling bond and interfacial defects. Since the doped amorphous nature of a-Si comes with poor conductivity, owing to low carrier mobility the transparent conducting oxide (TCO) needs to be integrated to achieve an effective collection of carriers across the metal contact. SHJ SCs, which are also referred to as HIT cells, have two additional advantages *i.e.*, (i) they can act as a bifacial module giving additional PCE benefit to the whole cell and (ii) exhibit a thin wafer size. With this SC architecture, the SHJ achieved an impressive PCE of 27%, with an excellent FF of 86% and more than 750 mV of V_{oc}. However, due to the expensive fabrication tool, incompatibility in transferring the production line of PERC/TOPCon to SHJ, and an additional gas safety facility hindering SHJ from achieving a large market share. In addition, the multiple doped a-Si and i-Si:H layers and dual TCO contact with indium tin oxide (ITO) cause a lot of parasitic absorption losses limiting J_{sc} in the SHJ.[157,158]

IBC. Compared to conventional Si SCs, the IBC technology integrates p- or n-type contacts at the back interface region. Consequently, it does not provide a shadowing effect or any reflection losses coming with front metal contact, which lowers the J_{sc}. It also has relatively low overall R$_s$ in the cell due to the absence of front contact, thus it provides higher J_{sc} and FF in the SCs. The front region can be made with an analogous device stack as SHJ or TOPCon having a front passivation layer and AR coating. In contrast, the p- or n-type contact can be made using laser ablation or wet chemical methods at the back. As most of the carriers get collected across the rare interface region, high-quality c-Si with a longer bulk carrier lifetime is required, to achieve a high PCE. It can be fabricated with both p- and n-type absorber layers.[159]

4.2. Tandem configuration and best Si bottom cell selection

In terms of device stacking, the typical chalcogenide absorber layers can be fabricated in both n–p and p–n device configurations, defined by the fabrication sequence of the semiconductor thin films, (*i.e.*, whether the n-type emitter is deposited before or after the p-type chalcogenide absorber). Materials such as Sb$_2$S$_3$, GeS, and AgBiS$_2$ have demonstrated higher PCE in the supertartrate (n–p) configuration, while materials like CXTS, CTS, and CGS have shown better performance in the substrate (p–n) configuration. Therefore, similar to PSK-Si TSCs, one should be cautious while deciding on the absorber polarity, Si polarity, and p–n junction location.[159,160] In the bottom Si SCs, the choice of Si wafer type mainly determines the junction location (p-type wafer: front junction and n-type wafer: rear junction) and studies in PSK-Si TSCs have shown that this switching of junction location can affect the overall tandem PCE.[160,161] Materials like Sb$_2$S$_3$, chalcogenide PSK, and AgBiS$_2$ sometimes utilize 2,2′,7,7′-tetrakis[*N,N*-di(4-methoxyphenyl)amino]-9,9′-spirobifluorene (Spiro-OMeTAD) as the hole transport layer (HTL), which can be a concern due to their parasitic absorption losses in n–p device stacking in 2T and 4T TSCs. Further, the bare Si wafer exhibits higher reflection; thus in SCs their reflection is generally minimized by texturing the front surface with the alkaline/acidic solution and applying the SiN$_x$ ARC layer. However, it's a fact that on such nano to micron-sized pyramids rough surface fabrication of a continuous and thin top wide-E_g chalcogenide absorber layer with good adhesion is quite challenging. Moreover, the chalcogenide absorber layer also comes with different surface roughness based on the fabrication process (Table S1 and Note 1, ESI†) can cause a large leakage current in TSCs. Thus, it is necessary to apply suitable deposition processes like solution, vacuum, or hybrid techniques that can provide high surface coverage, better adhesion, and minimal leakage current. Moreover, the use of suitable RLs, seed layer for chalcogenide growth, and ALD passivation strategies can also be applied which can passivate interface defects and minimize leakage current. A detailed discussion of these strategies can be found in Sections 5.1 to 5.4. Herein, we provided a possible 2T TSCs design architecture for emerging absorber materials considering different Si-based technologies as shown in Fig. 5.

In bottom cell fabrication, the PERC SCs are mostly fabricated with p-type wafers, while TOPCon SCs use n-type wafers; thus the junction/emitter can be formed by thermal diffusion of B or P, respectively. Due to higher costs, and high B thermal diffusion temperature, the n-type wafer remains costly, though theoretical PCE limits are the same for Si SCs. So, having n-type or p-type of PERC or TOPCon does not technically limit the theoretically achievable TSCs PCE. Recently, Messmer et al.[24] proposed four different bottom cell designs with TCO as RLs and a poly-Si tunneling layer of around 20–30 nm for PERC and TOPCon. Their simulation study also revealed that the TOPCon tandem PCE is better than PERC but lower than SHJ for PVSK-Si TSCs. These PCEs are mainly driven by higher V_{oc} and FF. Wright et al.[159] clearly pointed out the design flaws in PERC tandem design and claimed that lowering strict design requirements for PERC like single junction SCs could narrow down the PCE gap with SHJ. It also raises hopes for the design
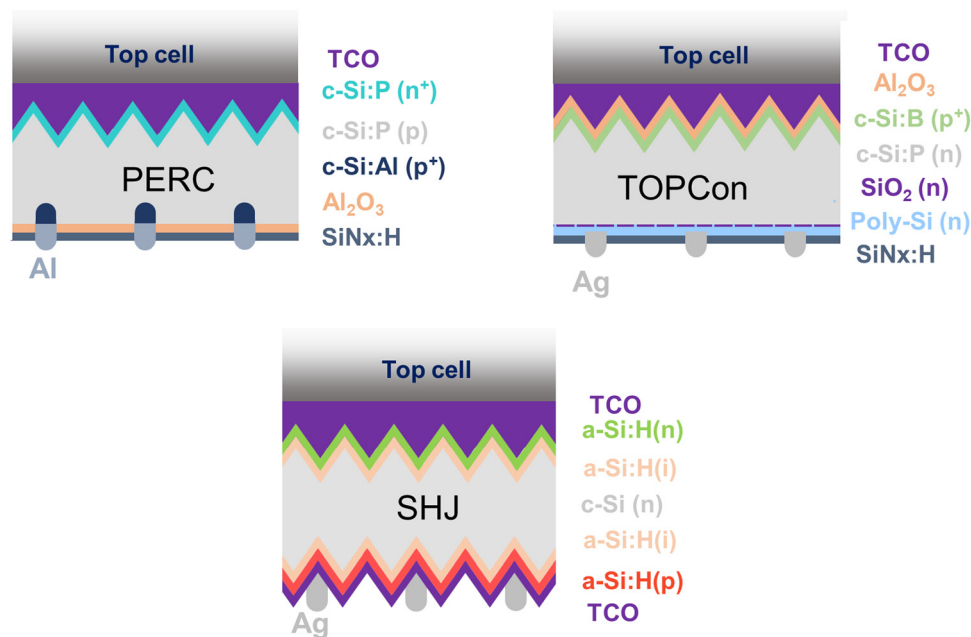
6908 | Energy Environ. Sci., 2025, **18**, 6899–6933

This journal is © The Royal Society of Chemistry 2025

Fig. 5 Possible 2T TSC design architecture for chalcogenide absorber layer with different Si-bottom cell technology.

consideration of PERC cells for emerging inorganic chalcogenide absorber-based Si TSCs.

The technological challenges in selecting suitable Si bottom cells for chalcogenide absorbers, considering their monolithic integration and the high-temperature processing of the top cell, have remained a significant concern. Popular HJS cells such as PERC and TOPCon exhibit high-temperature tolerance and can maintain thermal stability, while SHJ cells have a relatively lower temperature tolerance (<250 °C) due to a-Si:H layer.[162,163] Given the low-temperature fabrication feasibility of PSK materials, studies indicate that using SHJ devices in tandems leads to a remarkable PCE compared to HJS devices.[164] However, it is important to note that the limited temperature tolerance of SHJ cells due to the degradation of a-Si:H restricts subsequent processing of chalcogenide. In addition to temperature, solvent selection, solution processing, and passivation layers achieving high PCE is also a challenge. It makes a top absorber with a low-temperature process (*e.g.*, solution-processed absorber) feasible only for SHJ cells.[165] In contrast, during the fabrication of 2T TSCs, TOPCon and PERC are more suitable due to their compatibility with high-temperature processes. These high-temperature fabrication processes may also benefit the Si bottom cell by improving the bulk quality of the absorber layer.

While fabricating 4T TSCs, all Si architectures remain viable options. SHJ cells, however, are particularly attractive due to their higher efficiency and bifacial capability. SHJ cells exhibit lower recombination losses compared to PERC and Al-BSF cells. Moreover, careful optimization of TCO layers can reduce parasitic optical absorption losses from both the front and back sides, further enhancing their bifacial performance. This feature makes SHJ cells especially advantageous for bifacial 4T tandem configurations.

4.3. Challenges in existing Si-based TSC technologies

The inorganic III–V-Si TSCs are among the most successful and proven technologies to date and have shown outstanding PCE and long-term stability compared to other technologies such as the recent most efficient PSK-Si TSCs.[22] However, growing III–V materials over Si faces challenges due to the expensive fabrication process and epitaxial growth issue.[166,167] These include lattice, thermal coefficient mismatches, and high interface density defects. For instance, GaAs and Si have lattice constants of ~ 0.56 and 0.54 nm, respectively, resulting in a $\sim 4\%$ lattice mismatch and high dislocation density.[9,166] Nearly 2 orders of difference in thermal expansion coefficient add strain and lead to inferior crystallite quality.[168,169] To address these challenges, a combination of low and high-temperature growth modes in metal–organic chemical vapor deposition (MOCVD) is often used for effective epitaxial growth with a conformal deposition process.[166,170] The wafer bonding strategy is another approach, involving plasma or solution treatment, mechanical compression, and post-annealing steps to achieve strong wafer bonding, resulting in up to a 10% absolute enhancement in PCE of III–V-Si TSCs.[169,171,172] The inclusion of SiGe or GaAsP buffer layer for heteroepitaxial growth which provides a bridge between III–V and Si due to low lattice mismatch demonstrated promising pathways.[173] Record PCEs of 32.8 and 35.9% have been achieved with GaAsP-Si double junction and GaInP/GaAs/Si triple-junction grown with MOCVD and the above methods.[174] Mechanically stacked 4T GaInP/GaAs on Si triple junction with epoxy achieved PCE of $\sim 36\%$,[175] However, this method has a high-cost issue and a critical challenge due to

This journal is © The Royal Society of Chemistry 2025

Energy Environ. Sci., 2025, **18**, 6899–6933 | **6909**

adhesive epoxy materials.[176] Yet, it still exhibits challenges in the interface layer, surface roughness, and high interface R_s in III–V-Si TSCs.[9,166]

PSK-Si TSCs have recently gathered significant attention due to their unprecedentedly high PCEs over 34%.[20,23] Though, even with high PCE PSK-Si TSCs face widely recognized long-term stability issues.[13,23,33,177] The standard test conditions defined by the International Electrotechnical Commission 61215 standards remain a significant concern and need to be redefined for PSK SCs.[23,178,179] It includes standard test conditions (under 1000 W m^{-2}, 25 °C, and 1 Sun condition), the insulation tested under high applied voltage ± 1000 V, with 85 °C temperature and 85% humidity (damp heat test), field test, and light soaking conditions. They are sensitive to environmental factors such as light, temperature, humidity, and oxygen. To make an ideal E_g for tandems, the mixed halide cation ratios such as Br, iodine (I), and chlorine (Cl) are precisely tuned.[180,181] Among them, the Br and I are sensitive to light and are easily affected by light-induced degradation of the absorber layer with segregation of halide elements.[182,183] The Br segregation creates abundant vacancies in PSK. Multiple reports have claimed that at room temperature, the phases and shunting paths reduce long-term stability.[23] Large-scale fabrication and toxicity of Pb in high PCE devices are additional concerns, despite relatively low concentration in terms of a commercial perspective.[184–186] The degradation in J_{sc} of PSK-Si TSC is closely linked to the current mismatch.[187,188] The total J_{sc} in TSC is determined by the wide E_g top cell to achieve a high maximum power point. Therefore, the rapid degradation in wide E_g PSK SCs also leads to overall PCE degradation in TSCs.[189,190] Some wide E_g PVK SCs exhibit significant V_{oc} loss due to band alignment mismatches with the HTL and electron transport layer (ETL), as well as abundant defect densities.[191–194] Therefore, proper band alignment among the charge transport layers is crucial to avoid the V_{oc} loss. Additionally, the textured surfaces can cause local compositional inhomogeneities and affect quasi-Fermi level splitting.[23] Uncoated textured Si pyramids, non-uniform thickness, and high-density shunting paths are common in PSK-Si TSCs.[177,195,196] Despite the promising PCE of PSK-based TSCs, major challenges such as long-term stability and process compatibility with high-temperature annealing-based absorbers hinder their commercial viability.

4.4. Current progress in emerging chalcogenide–Si TSCs

So far, different types of Si-based TSCs have been extensively explored, but they are still far away from widespread commercial applications because of the limit of PCE in the top cells. An efficient top cell is crucial for improving the PCE of the total TSC system.[197] Beyond optimizing each sub-cell, there are several unique challenges to developing efficient monolithic multi-junction SCs. The present section summarizes the current progress in the fabrication of chalcogenide–Si TSCs and their PCE progress (Table S2, ESI†).

(a) Chalcopyrite compounds. Ironically, most Se-based compound photo-absorbers have narrow E_g characteristics.

The only Se-based absorber layer with a suitable wide E_g for TSC is CGSe with an ideal E_g of ~1.7 eV. Initial attempts by the National Renewable Energy Laboratory (NREL) achieved a promising device PCE of 5.1% for 2T CGSe-Si TSCs.[198] The absorber was fabricated at 550 °C on an ITO-covered Si substrate, with the device completed using sequential deposition of CdS/ZnO/Al layers. The device achieved a promising V_{oc} of 1.32 V with J_{sc} of ~9.0 mA cm^{-2} and FF of 43%. Jeong et al.[199] reported the fabrication of CGSe/ITO/Si structured 2T TSCs, achieving PCE of ~10%. Their study concluded that using the ITO as an RL between Si and CGSe in TSCs mitigates resistive losses without sacrificing electrical properties.[9] Both studies used CGSe and Si with E_g values of 1.7 and 1.12 eV, respectively. Furthermore, Kim et al.[200] simulated the CIGS E_g from 1.4 to 1.7 eV with respect to the absorber thickness ranging from 0.2 to 2.0 μm. They found that achieving current matching in CIGS top cell with E_g of 1.5 eV is difficult until a 200 nm thick absorber layer for ~19% Si bottom cell. Conversely, with a relatively wider E_g of 1.6–1.7 eV, it is achievable with higher PCE in TSCs. Since the CIGS top cell with E_g of 1.7 eV has a low PCE of ~12%, the overall PCE of TSCs is limited to that of the Si bottom cell (19.0–19.8%). Further, it has been reported that the high-temperature rapid thermal annealing (RTA) process during CIGS fabrication can degrade the Si bottom cell. The formation of GaO$_x$ near the ITO layer during the deposition of CIGS contributes to the resistive loss.[201] Therefore, a 4T device configuration can be a more suitable alternative for constructing the most efficient CIGS-Si TSCs.

(b) Kesterite-related compounds. Kesterite-based Cu$_2$-II–IV–VI$_4$ chalcogenide semiconductors, where II can be Zn, Cd, or Ba; IV can be Si, Ge, or Sn; and VI can be S and Se, have demonstrated potential PV applications due to their outstanding optical and electronic properties as discussed earlier. However, quaternary kesterite-based CZTSSe compounds have shown the highest PCE of >15.1% for 1.1 eV.[202] For Si-based TSCs, progress is limited due to the high-temperature (>500 °C) step in chalcogenide material synthesis, which can degrade the Si bottom cell. To address this issue, various intermediate barrier layers such as MoS$_2$[203] or TiN,[204,205] have been explored. Valentini et al.[203] applied the triple barrier layers of MoS$_2$/FTO/ZnO to prevent the degradation of Si bottom cells and elements interdiffusion, accomplishing a PCE of 3.5% with V_{oc} of 950 mV, and FF of 58.3%. Marthino et al.[204] reported effective control over elemental interdiffusion using ultrathin TiN and TiO$_x$N$_y$ interfacial layers (<10 nm) at the Si/CZTS interface. Additionally, the Al sandwiched TiN/Al/TiN layer showed a PCE of 3.9% with V_{oc} up to 1.06 V, indicating diffusion barrier layers can also serve as RLs in 2T Si-based TSCs. Cu has relatively high diffusivity, potentially forming abundant defects on Si surfaces or Cu$_5$Si precipitates that create mid-gap defects.[206] To overcome this, a thin TiN barrier on a double-sided TOPCon Si cell was found effective against the high-temperature RTA process and Cu-diffusion phenomenon.[205] Using TiN/Al/TiN triple barrier layers, CZTS was grown using pulsed laser deposition with oxide- and S-based precursors.[207] The study showed that oxide-based

6910 | Energy Environ. Sci., 2025, 18, 6899–6933
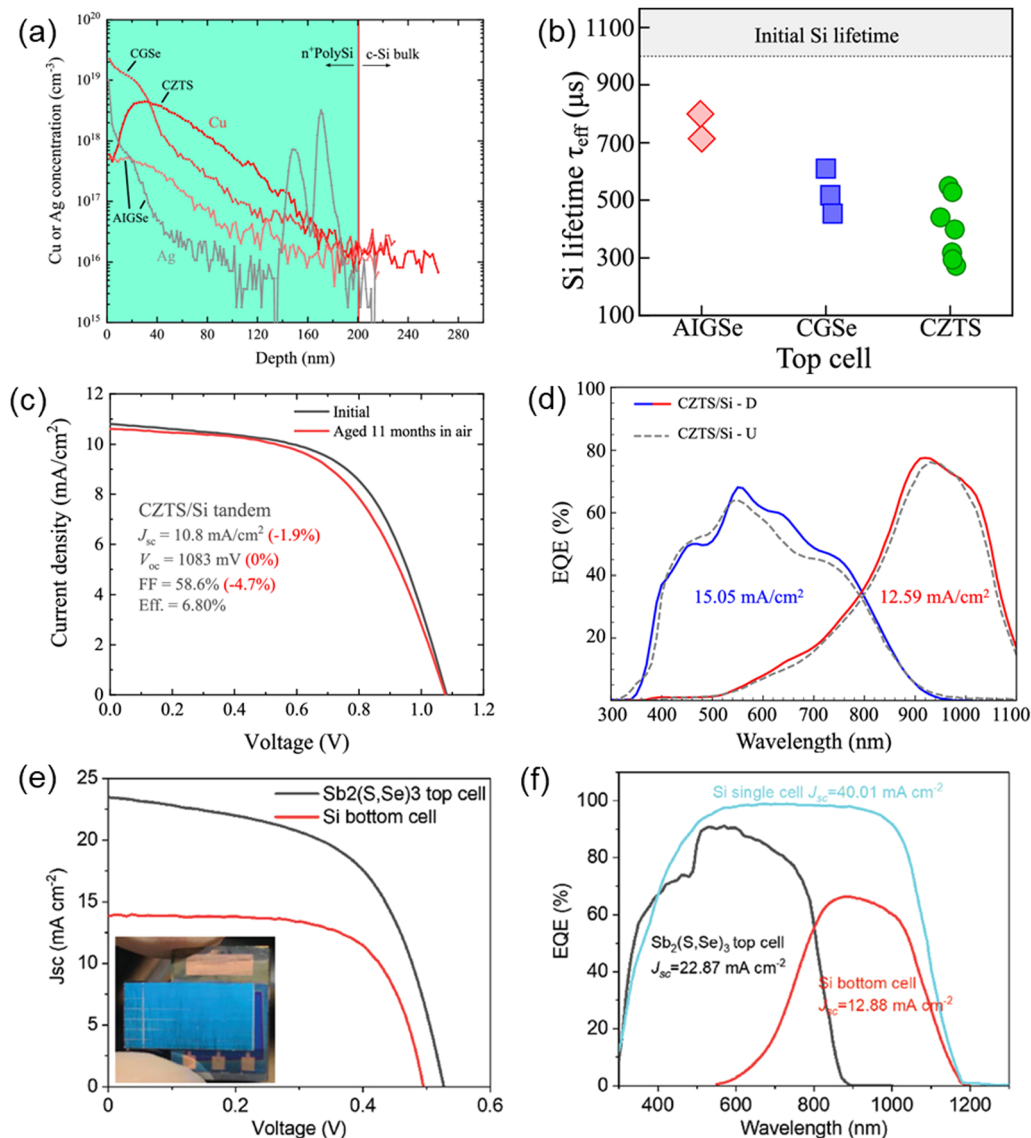
This journal is © The Royal Society of Chemistry 2025

Fig. 6 (a) Cu-diffusion gradient for CZTS, CGS, and Ag gradient for AIGSe, (b) Si carrier lifetime before and after fabrication of top cell, (c) $J–V$ curves, and (d) EQE spectra for the 2T CZTS-Si TSCs.[208] Reproduced with permission, Copyright 2022, American Chemical Society (e) $J–V$ curves and (f) EQE spectra for the 4T $Sb_2(S,Se)_3$-Si TSCs.[209] Reproduced with permission, Copyright 2023, Wiley-VcH.

precursors (*i.e.*, $Cu_{2−x}O_x$, ZnO, and SnO_2) exhibit higher Cu diffusivity than S-based precursors (*i.e.*, CuS, ZnS, and SnS). The oxide precursor also modified the barrier layer properties and transparency. The partial oxidation of the barrier layer improved transmittance, enhancing J_{sc} in Si bottom cells, though it decreased FF due to electrical property degradation. This approach achieved a PCE of 4.8% for 2T CZTS-Si TSCs. To further improve the Si bottom cell's thermal stability during top cell fabrication, poly-Si/SiO_x passivating contacts with varying thicknesses were applied, which improved carrier lifetime above 500 μs.[208] The barrier layer significantly decreased impurity diffusion in c-Si bulk during the RTA process, resulting in improved lifetime. In comparative studies with CGSe and (Ag,Cu)(In,Ga)Se_2 (AIGSe) layers, the barrier layer provided different Cu diffusion gradients for the absorber layer

(Fig. 6(a)). It indicated that AIGSe is less prone to Si degradation, while CGSe and CZTS are more susceptible during the RTA process, affecting Si carrier lifetime (Fig. 6(b)). Finally integrating a thinner TiN layer with poly-Si improved transmittance resulting in one of the highest reported PCEs of ~7% 2T CZTS-Si TSCs (Fig. 6(c and d)).

(c) **Binary chalcogenides.** The V_2VI_3 chalcogenides family includes compounds where V = As, Sb, Bi, and VI = S, Se, with very few reports on Te-based fabrication of the absorber layer.[210] Recently, widely researched and reported compounds in this family are Ag_2S, Bi_2S_3, SnS, Sb_2X_3, and GeS.[27] Among them, Sb_2S_3 is particularly suitable for use as a top cell in Si-based TSCs due to its nearly ideal E_g. Both Sb and S are earth-abundant, nontoxic, and low-cost elements, making them economically and environmentally viable for TSC applications

This journal is © The Royal Society of Chemistry 2025

Energy Environ. Sci., 2025, **18**, 6899–6933 | **6911**

as discussed earlier. The planner device configuration is more suitable for TSC fabrication with a low-temperature solution-based approach. Based on its strong candidacy, Gao et al.[211] reported the successful fabrication of an Sb_2S_3 absorber layer over an n-type Si substrate via a sputtering process at different substrate temperatures. Interestingly, the sputtered Sb_2S_3 absorber layer showed a direct E_g transition from 2.52 to 1.49 eV as the substrate temperatures increased from room temperature to 400 °C. The complete device, fabricated with Ag/ITO/i-ZnO/CdS/Sb_2S_3/Si based on an optimal deposition temperature of 350 °C, resulted in a V_{oc} of 367 mV, a J_{sc} of 0.01 mA cm^{-2}, and an FF of 28%, respectively. Xiao et al.[209] recently reported 4T TSCs with semi-transparent $Sb_2(S,Se)_3$ SCs with an E_g of 1.5 eV. The $Sb_2(S,Se)_3$ top cell achieved a PCE of around 7.05%, while the top cell filtered Si bottom cell had a PCE of 4.61%. As a result, the 4T $Sb_2(S,Se)_3$-Si TSCs demonstrated an excellent PCE of 11% (Fig. 6(e and f)). In addition to the fabrication of 2T and 4T TSCs, a simulation report is available on the design and analysis of Sb_2S_3-Si TSCs, summarizing that based on top cell optimization, PCE can reach up to 24–30% with top and bottom absorber thicknesses of 300–700 nm.[212]

4.5. Key challenges for emerging inorganic chalcogenide–Si TSCs

Emerging inorganic chalcogenide–Si TSCs have shown potential for significantly improved device performance than single-junction SCs.[27] Despite the promising optoelectronic properties and advancements in single-junction SCs as discussed in previous sections, inorganic chalcogenide–Si TSCs still exhibit inferior PCE compared to III–V-Si and PSK-Si TSCs. Previous studies have demonstrated that emerging inorganic chalcogenide–Si TSCs present several challenges in achieving competitive device performances.[9,197] These challenges include device fabrication processes, E_g tuning, stability, reducing non-radiative recombination losses, and maximizing light capture. The two largest challenges and design criteria are: (1) proper sub-cell selection for current matching with suitable E_g, and (2) multilayered process compatibility during TSC's fabrication process. In monolithically integrated 2T TSCs, the two sub-cells are connected in series, and J_{sc} in TSCs is limited by the cell having low J_{sc}, thus it becomes necessary to consider the current matching conditions in a 2T device's design. In another case, not all Si SCs are compatible with the thermal annealing process at high temperatures. In this regard, it should make sure that in the fabrication of the 2T tandem, the subsequent layers should be fabricated in such a way that the bottom Si cell does not degrade. The present section briefly discusses the above issues.

(a) **Device fabrication process.** In the case of monolithic 2T Si-based TSCs, critical issues in the fabrication process persist. The synthesis mechanism and/or systematic experimental results for chalcogenide absorber layers on Si bottom cells have not been established yet; thus, fabricating high-quality absorber layers with outstanding optoelectronic properties while suppressing defects and related defect clusters is of prime importance. Generally, the high quality of ternary and

quaternary chalcogenide-based absorbers requires a high-temperature annealing process above 300–500 °C for the crystallization. It can damage interconnecting layers and/or Si bottom cells in TSCs.[203,213] Different strategies have been made to suppress the annealing temperature and modify the annealing process through doping and others, but they result in the formation of secondary phases, voids, and pinholes.[214,215] Further, the use of non-stochiometric composition in the fabrication of the quaternary absorber layer such as CZTS and CIGS also results in the formation of defects and defect clusters.[216,217] This deep defect and defect cluster significantly contribute to the non-radiative losses via the defect-associated recombination mechanism. As discussed earlier, the Cu-based chalcogenide absorber layer presented high Cu diffusivity during the annealing process hampers the interface besides creates a compositional fluctuation in the absorber layer. On the contrary, the low-temperature processed binary chalcogenide absorber materials such as Sb_2S_3 or SnS demonstrated elemental loss at <450 °C annealing temperature.[218,219] The poor crystal quality of chalcogenides on Si bottom cells may lead to sub-E_g absorption and abundant defects, resulting in dramatically reduced carrier diffusion lengths due to the highly reactive chalcogen vapors (S and/or Se).[176] This issue necessitates the introduction of diffusion barriers or the development of lower-temperature synthesis methods for chalcogenides. Reduced transmittance and additional R_s from the diffusion barrier layer are believed to be the main causes of poor PCE in chalcogenide–Si TSCs.

(b) **Unoptimized transport layer and interfaces.** The chalcogenide-based TFSCs, as well as the TSCs carries multiple layers including the TCO and buffer layer. These charge transport layers and different interfaces must have optimal band alignment, lower lattice mismatch, smooth surface, and low interface defect density for efficient carrier transport.[220,221] The conventionally used CdS buffer layer exhibits cliff-like band offset issues with materials such as CZTS. The interdiffusion of elements from the buffer or absorber layer may provide lattice mismatch, uneven interface, and carrier recombination pathways.[221] Following the success of CdS layer, it is also used as ETL in binary and ternary absorber materials; however apart from the CdS layer only a few oxides-based TiO_2 or SnO_2 have shown some promising results in single junction SCs.[65] It shows the need for a promising ETL that provides optimal band offset and high-temperature stability for efficient carrier transport properties without sacrificing device PCE. Inspired by PSK SCs, different HTL layers employed such as poly(3,4-ethylenedioxythiophene)-poly(styrenesulfonate) (PEDOT:PSS), Spiro-OMeTAD, and ploy[bis(4-phenyl)(2,4,5-trimethylphenyl) amine used in absorber materials such as Sb_2S_3 and $AgBiS_2$.[65,222] They still face challenges with band alignment and long-term stability issues. The Spiro-OMeTAD layer, also known for its parasitic absorption, may also hamper the tandem performance due to its thickness and absorption of high-energy photons.[223] The segregation of secondary phases and the formation of interface defects are usually observed in most of the chalcogenide-based absorber layers.[224,225] The

6912 | Energy Environ. Sci., 2025, **18**, 6899–6933

This journal is © The Royal Society of Chemistry 2025

unpassivated grain boundary and interface defect significantly contribute to the non-radiative recombination losses. Another critical issue in the fabrication process of 2T chalcogenide–Si TSCs is poor adhesion between chalcogenides and Si bottom cells. The significantly different lattice constants and thermal expansion coefficients between chalcogenides and Si can easily cause thermally induced stress during the upright growth from Si, leading to poor adhesion.[213] Commonly, chalcogenide single-junction SCs are prepared on molybdenum (Mo) rear contacts, with interfacial $Mo(S,Se)_2$ layers forming irreversibly during the synthesis process. This interfacial layer aids adhesion between chalcogenides and Mo rear contact as well as the formation of ohmic contact.[32,226] A promising solution can be developing a suitable interconnection layer with diffusion barrier capabilities (*i.e.*, buffer role) in 2T TSCs, however detailed studies have not yet been reported. In a mechanically stacked 4T TSC, each cell's PCE is individually collected. This results in complex interconnections for module-level cells, increasing fabrication costs and limiting large-scale production. The difference in refractive index between top and bottom cells at the air gap in 4T TSCs causes optical losses (*i.e.*, parasitic absorption at both cell surfaces), significantly reducing PCE compared to theoretical values.[12] Developing functional layers (*i.e.*, interfacial layer) to minimize optical loss could replace the air gap in 4T TSCs, however, this technology has not yet been addressed. Additionally, there are some technical challenges for 4T TSCs, such as simultaneous measurement of both cells for coupling effects and measuring PCE in the same area for both cells.[43] Deep insights and understanding of device structures and characterization processes in 4T TSCs are crucial for developing higher PCE than single-junction SCs.

(c) E_g Tuning in chalcogenide. As explained earlier, TSCs consist of a top cell with a wide E_g and a bottom cell with a narrow E_g to achieve high device PCEs beyond the limits of single-junction SCs.[227] Fully sharing the solar spectrum requires matching E_g for each cell, which is crucial for high performance in TSCs. Fig. 7 shows the theoretical device performances for TSCs with various E_g in the bottom and top cells in both (a) monolithic 2T and (b) mechanically stacked 4T

configurations. Theoretically, the best-calculated performance is about 47% for TSCs with a combination of $E_g \sim 1.63$ eV in the top cells and $E_g \sim 0.96$ eV in the bottom cells.[65,228] For the well-established c-Si bottom cell with an E_g of 1.1 eV, the ideal top cell absorber E_g for 2T TSCs is about 1.65 eV, while 4T TSCs is 1.6 to 2.0 eV, achieving PECs over 44%.

In the case of the chalcogenide absorber family due to their narrow E_g of Se-based compounds such as CISe, CIGSe, AIGSe, and $Cu(In,Al)Se_2$, with $E_g < 1.2$ eV, are not well suited as top cells even if they have high PCE. However, pure 'S' based absorber layers such as CIS, CIGS, and CGS can be used as top cells. CIS ($E_g = 1.5$ eV) and CIGS ($E_g = 1.57$ eV) have a compatible E_g but still can achieve the PCE $\sim 30\%$ for 2T devices. In contrast, CGS has a wide E_g of 2.5 eV, suitable for use as a top cell in triple junction TSCs. The 'Se' based chalcopyrite CGSe has the most favorable E_g and can be tuned with a Ga/Se ratio from 1.65 to 1.85 eV, making it a promising top cell for Si TSCs.[229] In the case of the kesterite family, E_g values for Cu_2MgSnS_4, Cu_2FeSnS_4, Cu_2CoSnS_4, CBTS, and Cu_2SrSnS_4 are estimated to be approximately 1.6, 1.2, 1.11, 2.11, and 1.8 eV, respectively. Zn-substituted CXTS-inspired absorbers, such as those substituted by Mn, Mg, Fe, Ba, and Sr, appear promising as top cells with E_g close to 1.6 eV. The highest PCE pure 'S' based CZTS absorber has E_g around 1.55 eV, while the most efficient CZTSSe absorber with >15% PCE exhibits E_g around 1.1 eV.[57] Thus, pure S-based CXTS absorbers with tunable E_g via partial or complete cation substitution in CXTS have a strong potential to make in Si-based TSCs with predicted PCE $\sim 35\%$. Following, in binary chalcogenides, such as GeS, Sb_2S_3 has an experimentally reported E_g ranging from 1.6–1.9 eV. GeSe, Sb_2Se_3, and SnS have an E_g of 1.1–1.3 eV, eliminating them from top cell competition. The experimentally reported values for SnS lie between 1.1–1.7 eV, possibly due to the co-existence of a secondary phase like SnS_2, which has an E_g of 2.2–2.4 eV. Thus, for binary chalcogenides, like GeS and Sb_2S_3 with an E_g of around 1.7–1.8 eV, perfectly withstanding the ideal tandem top cell, though for high PCE Si-based TSCs, their E_g can be tuned with Se to match well with 1.65 eV required for bottom cell. They can also potentially deliver theoretically predicted PCE over 35–40%
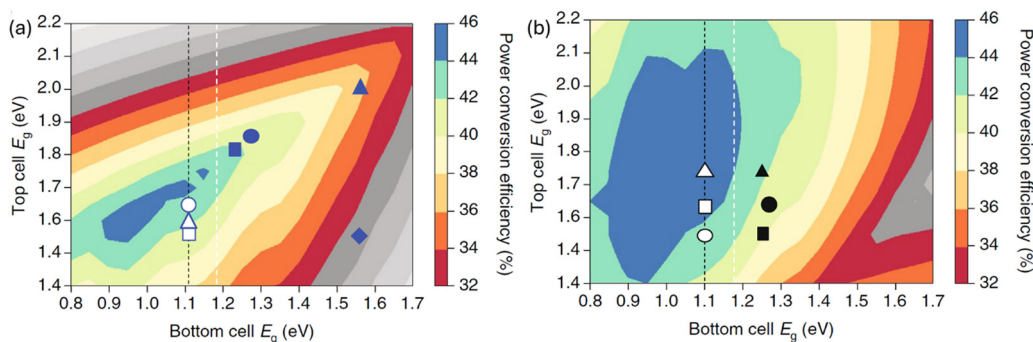

Fig. 7 Theoretical performance for (a) 2T and (b) 4T TSCs, calculated with different E_g for top and bottom cells. Grey shading regions show lower device performance of TSCs than that of Shockly–Queisser limit of 32% for single junction with E_g of 1.1 eV. The open symbols represent the E_g combination for the best performance of 2T and 4T PSK-Si TSCs.[13] Reproduced with permission, Copyright 2018, Nature Publishing Group.

This journal is © The Royal Society of Chemistry 2025

Energy Environ. Sci., 2025, **18**, 6899–6933 | **6913**

with a well-developed single-junction SCs device fabrication strategy.

Over the years perovskite-based absorbers in Si tandem technology present ease of fining tuning of E_g with the help of halide ions to achieve current matching in 2T TSCs.[230,231] Matter of fact in the chalcogenide community a well-established fine E_g tuning strategy is strongly needed to achieve the desired E_g. Different E_g grading strategies such as V-shape grading, grading in space charge region (front interface), or at the rear interface are reported to maximize PCE.[232] In the case of CIGS and CIGSe TFSCs different E_g grading strategies during absorber growth have shown some success with modification in In, Ga, and S ratios. But the elements such as S and Se which dominantly affect the band position and modify the E_g properties, haven't been proposed. Thus, GeS, Sb_2S_3, CXTS, and CGSe are the most promising absorber materials and are in line to be part of Si tandem technology with their E_g values. And it would be interesting to see their progress in single junction alongside Si-based TSCs technology.

(d) Achieving targeted J_{sc} V_{oc}, and PCE for the top cell. J_{sc}: The current matching is one of the key criteria in the design principle of 2T TSCs. In 2T TSCs, the maximum tandem PCE can only be achieved if the photocurrent generated by the top cell is consistent with that by the bottom cell. For 2T Si-based TSCs, under the best-case scenario, the top cell should absorb half of the available photons with energy higher than 1.1 eV and generate nearly half of the photocurrent of a single-junction Si bottom cell, while allowing the other half unabsorbed photons to enter the Si cell and generate the same amount of photocurrent density. Therefore, the top cell for Si-based TSCs should generate a photocurrent density of ~20–22 mA cm^{-2} and meanwhile be sufficiently transparent to allow the equivalent amount of low-energy photons to be harvested by the Si with an E_g of 1.1 eV. For 4T tandems, the current match limitation does not exist because each sub-cell operates independently. For the same Si bottom cell, the better (higher efficiency and transparency) the top cell, the better the 4T tandem PCE.

We now consider the emerging chalcogenide single junction SCs and their theoretically achievable $J_{sc(S–Q)}$ that can fulfill the current matching criteria. Interestingly, most chalcogenide-based absorbers have already achieved more than 75% of their $J_{sc(S–Q)}$, however, it is inferior to those of high-performance absorbers such as c-Si, PSK, GaAs, CIGS, and CdTe, which are well above 90%. Emerging absorber materials such as GeS, SnS, AgBiS$_2$, CGSe, and Sb$_2$(S,Se)$_3$ with relatively wider E_g (>1.5 eV) have their $J_{sc(S–Q)}$ nearly 70–80% range and still need further improvement. Nonetheless, the most efficient chalcogenide-based TFSCs generate enough J_{sc} that can be considered as the top cell for 2T and 4T Si-based TSCs. Materials with wider E_g like GeS, CGSe, or Sb$_2$S$_3$ currently have relatively lower J_{sc} than the 2T current matching criteria shown in Fig. 8(a), Table 3, and Table S3 in ESI,† but it can be tweaked further with fine E_g and thickness tuning and absorber properties improvement.

V_{oc}: 2T and 4T TSCs require all sub-cells to achieve their best V_{oc} to maximize tandem PCE. Some chalcogenides have outstanding optoelectronic properties for the required top-cell

absorber materials; however, their current PCEs lag the value needed for the top cell of efficient 2T TSCs (see Fig. 8(b)). The main reason for this inferior PCE is the high V_{oc}-deficit (defined as E_g/q-V_{oc}) characteristics.[27] Fig. 8(b) shows the V_{oc} of different chalcogenide TFSCs placed at a theoretically achievable $V_{oc(S–Q)}$ for their corresponding E_g. The overall scenario shows that only GaAs and PSK with recent PCE development have achieved more than 94% of their $V_{oc(S–Q)}$, while c-Si has achieved about 88% of its $V_{oc(S–Q)}$. A recent development from 'EMPA' and the 'First Solar' pushed the CIGSe and CdTe to $V_{oc(S–Q)}$ $>75\%$, while the rest of the chalcogenide, except CIGSe lies in the 50–75% limit. The chalcogenides with narrow E_g show lower V_{oc} loss, while wide E_g suffers higher V_{oc} loss. Among the emerging chalcogenide absorber layers like Sb$_2$(S,Se)$_3$, AgBiS$_2$, and CZTS remains near 50%, which needs concentrated development in the absorber layer to boost the V_{oc} and PCE.

PCE: The high PEC of the top cell is another critical factor because the top cell can provide a large fraction ($\sim 2/3$) of the energy of the total tandem system.[234] Fig. 8(c) shows the required efficiency of the top cell in 2T Si-based TSCs to yield 25, 27.5, and 30% PCE, respectively, based on top cell parameters like E_g, diffusion length, absorption coefficient, and FF.[21] Studies indicate that the top cell with a wide E_g only absorbs a small fraction of the incident photons, maximizing the PCE of the Si bottom cell. As a result, a top cell having E_g in the range of 1.5–1.7 eV must exhibit more than 15% to achieve 25% Si-based TSCs PCE. While reaching beyond 27.5 and 30% tandem efficiency, 17.5 and 20% top cell PCE are required in a similar E_g range. The gray shaded area shows that the current PCE of some chalcogenide TFSCs was reviewed by White *et al.*[21] has been upgraded further and is approaching the theoretical value required beyond 25% PCE of single junction Si SCs. Another factor to consider for TSC design is light management for the sub-cells. The bottom cell in the TSCs only receives the illumination transmitted through the top cell. A chalcogenide-based absorber layer typically has absorption coefficients above its E_g on the order of 10^4 to 10^5 cm^{-1},[235,236] and has discernible parasitic absorption below E_g due to defects and impurity phases. Consequently, the trade-off between sufficient absorption of high-energy photons and transmission of low-energy photons in the top cell needs to be tailored. Fig. 8(d) shows the transmittance of the top cell *vs.* the device PCEs of 4T Si-based TSCs under various top cell PCEs. Over 80% transmittances are required for the top cell with an E_g of 1.5 eV having PCE of 8%, to achieve a higher PCE in TSCs than in single-junction Si SCs. Ultimately, relaxed transmittance in the top cell achieves over 25% PCE in tandem configurations if the top cell exceeds 22% PCE.

The above situation gives an idea about the required top cell PCE while controlling transmittance. However, the current situation of single junction emerging chalcogenide-based SCs is well below the criteria. We have plotted the device parameters of some of the champion emerging chalcogenide-based SCs and well-established PV systems with respect to S–Q limit and categorized them into the different PV technologies, which are (i) high-performance $\eta_{S–Q}$ $>75\%$, (ii) moderate

6914 | *Energy Environ. Sci.*, 2025, **18**, 6899–6933

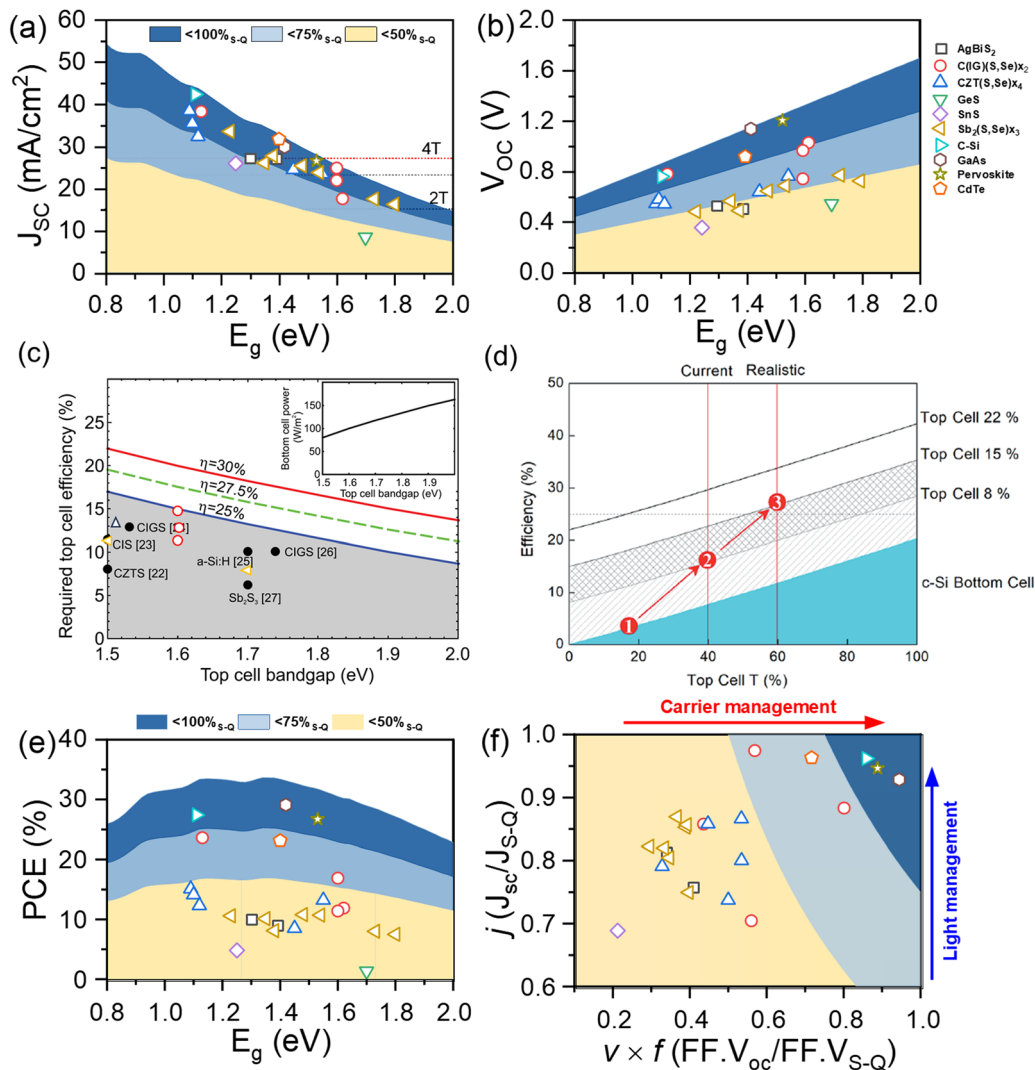This journal is © The Royal Society of Chemistry 2025

Fig. 8 Reported champion cell parameters compared to the detailed-balance limit of single-junction SCs as a function of E_g (a) Short-circuit current (J_{sc}), (b) open-circuit voltage (V_{oc}), (c) required top cell efficiency in Si-based TSCs to achieve 25, 27.5, and 30% efficiencies, respectively.[21] The filled symbol shows the previous chalcogenide PCE and the hollow symbol shows the recent PCE. Reproduced with permission, Copyright 2014, IEEE, (d) transmittances of top cell *vs.* the device performance of 4T Si-based TSCs under different efficiencies of top cell.[233] Reproduced with permission, Copyright 2019, Royal Society of Chemistry. Detailed-balance limit of single-junction SCs as a function of band gap for (e) PCE and (f) j *vs.* $v \times f$.

Table 3 Possible chalcogenide absorbers and their predicted PCE based on their E_g

Top cell material (example)	Top cell E_g (eV)	V_{oc} (V)	J_{sc} (mA cm^{-2})	Predicted tandem PCE
CGSe, BaZrS$_3$,	1.6–1.8 eV	1.1–1.3 V	15–20 mA cm^{-2}	30–33%
Sb$_2$S$_3$	1.7–1.8 eV	1.3–1.6 V	15–18 mA cm^{-2}	35–40%
CdTe, CZTS	1.5 eV	~1.0 V	~18–20 mA cm^{-2}	~30%

performance η_{S-Q} 75–50% and (iii) low-performance η_{S-Q} <50%. Fig. 8(e) shows that only PSK, c-Si, and GaAs have achieved more than η_{S-Q} >75%. On the other hand, the rest of the chalcogenide community struggles with PCE and resides below 50% of η_{S-Q}, except CIGSe, and CdTe. As explained earlier, the PCE of the emerging chalcogenide-based absorber layer must be improved to withstand competition in Si-based TSCs technology for top cell competition. We have calculated the S–Q limit for the

corresponding device for each device parameter based on their reported E_g value (see Table S3). The lower PCE compared with the S–Q limit can be clearly identified as a large V_{oc} loss. To further identify key issues in the poor performance reason and give ideas about further improvement, we plotted the $j(J_{sc}/J_{(S-Q)})$ versus $v \times f$ ($V_{oc} \times FF/V_{oc(S-Q)} \times FF_{(S-Q)}$) for all the reported champion emerging absorber materials along with ultra-high PCE PV materials (Fig. 8(f)). It provides insight into whether the PCE is limited by

This journal is © The Royal Society of Chemistry 2025

Energy Environ. Sci., 2025, **18**, 6899–6933 | **6915**

light management or charge carrier management. The ratio $j(J_{sc}/J_{(S-Q)})$ reveals the J_{sc} losses coming from the light coupling, absorption, and trapping in the active layers from the top cell, followed by its carrier collection efficiency. The voltage ratio $v = V_{oc}/V_{S-Q}$ shows the dominance of the carrier's recombination losses from the bulk, surfaces, and interfaces. Altogether $(v \times f)$, the voltage ratio and fill factor ratio $f = FF/FF_{S-Q}$ indicate the total electrical limitations of a cell. As expected, the j and $v \times f$ ratio approach unity for c-Si, GaAs, and PSK PVs and have good light and carrier management. In contrast, some chalcopyrites like CIGSe and CdTe are in moderate regions (0.5–0.75) situated in the upper regime, indicating these absorber materials have well-light management but need focused research on carrier management. This can be achieved through improved interface passivation, enhanced carrier extraction, and effective bulk defect suppression strategies to further boost V_{oc} and reach the theoretical maximum PCE limited by non-radiative losses. Interestingly, the rest of the chalcogenide absorber materials exhibit j well beyond 0.7, ranging from 0.7–0.9, but scattered across the $v \times f$ far below 0.6, indicating the poor PCE is mainly limited by the bulk and interfaces as shown in Fig. 8(f). In other words, the high concentration of intrinsic defects, related defect clusters, band tailing (especially kesterite-based compounds), inherent deep-level defects, and high interface-assisted recombination rates (*i.e.*, lattice mismatch, contamination of impurities, and dangling bonds at the interface) are believed to be the main causes of V_{oc} loss and poor absorber quality for chalcogenide-based top cells.[65,237,238] In particular, the abundant intrinsic defects and defect clusters can cause a significant downward shift of CB edge and non-radiative recombination, resulting in a large V_{oc} loss.[27,237] Moving forward, the typical minority carrier lifetime reported for high PCE devices remains in the range of 1–10 μs to 100–200 ns, while those for emerging chalcogenide absorber materials come several orders lower ∼1–10 ns or less due to dominant defect assisted non-radiative carrier recombination. The high carrier density, resulting from a large concentration of

shallow acceptor-like defects, along with low hole mobility, limits efficient charge transport in the absorber layer. This leads to increased non-radiative recombination, reducing carrier lifetime and extraction. In addition, the low hole mobility also lowers the carrier collection probability, which is very high in the emerging absorber layer. These factors show that better carrier management is needed for emerging chalcogenide absorber materials compared to light management.

5. Strategies to improve the PCE of emerging chalcogenide–Si TSCs

5.1. Low-temperature fabrication techniques to produce high-quality top cell

To produce high-quality 2T TSCs with high PCE, a key requirement is to produce a well-crystallized chalcogenide absorber layer with pure phase and low defect density. Despite the challenges in fabrication shown in Fig. 9, recent advancements in low-temperature processing of chalcogenide absorbers make it possible to develop efficient devices. These materials can be fabricated using both physical and chemical deposition methods, besides hybrid methods combining both techniques for optimized results, as explained below.

(a) ALD. ALD technique is known for its precision, which gives better control over material thickness and composition. By adjusting the number of precursor cycles and pulse sequence, one can control the film thickness composition meticulously.[239–242] Moreover, by controlling factors such as precursor pulse rates and substrate temperatures and others, high-quality thin films of binary and ternary chalcogenides can be produced. This method is particularly efficient for forming uniform layers with controlled stoichiometry. Similarly, this technique can also be employed in the fabrication of ETL and HTL layers that can prevent bottom cell degradation.[242] Further, the quality of the ALD-grown absorber can be
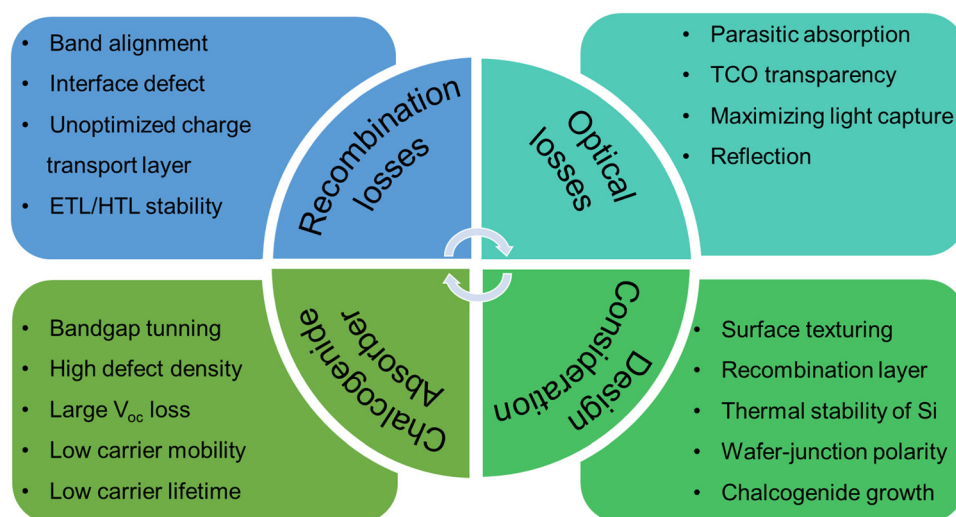

Fig. 9 Different challenges associated with emerging chalcogenide absorber top cell and Si bottom cell during TSC fabrication.

6916 | *Energy Environ. Sci.*, 2025, **18**, 6899–6933

This journal is © The Royal Society of Chemistry 2025

improved through post-treatment processes such as sulfurization in an S-rich environment or passivation with Cl and S which improves carrier transport and reduces defect density.[243,244]

(b) TE. TE is another effective physical technique that can grow a chalcogenide absorber layer with better uniformity and surface coverage, especially for materials with lower melting points. It is particularly suitable for materials such as Sb_2X_3 and GeS, as their melting points are relatively low (Sb_2Se_3: 611 °C, Sb_2S_3: 550 °C and GeS: 660 °C).[245–247] It provides options for single or multi-source evaporation of chalcogenide precursors, where the thickness of the thin film can be easily controlled with evaporation flux or applied current with the help of an in-built quartz crystal thickness monitor. TE can lead to high-quality absorber films with fewer secondary phases, pure phases, and low defect densities based on absorber type. These factors can be controlled via various process parameters such as substrate temperature, evaporation sequence, evaporation temperature, and time.[53,214,248,249]

(c) Vapor transport deposition (VTD). VTD involves the transport of chalcogenide vapors through a carrier gas to a substrate.[250–252] This method enables the controlled deposition of high-quality, uniform films, even at temperatures below 500 °C making it compatible with large-area fabrication. In this technique, the thickness and stoichiometry of thin films can be tuned through deposition temperature and time. The studies have demonstrated the successful fabrication of Sb_2X_3, GeS, SnS, and chalcogenides PSK at low temperatures (e.g., $BaZrS_3$ at 400–500 °C).[253]

(d) Spin coating and post-annealing. The spin coating is an efficient lab-scale method for fabricating chalcogenide absorber layers. This technique involves depositing precursor solutions onto substrates and then annealing at lower temperatures. The initial annealing of ∼100 °C is used for solvent removal, while the post-annealing of the films ∼300 to 500 °C is for crystallization and stoichiometry control.[254] Recently, various approaches have been demonstrated for phase, morphology, and stoichiometry control via engineering solvent systems with thiol-amine, dimethyl sulfoxide, and hydrazine, alongside precursors and additives.[30,255–257] The addition of dopants in solution has also been found to assist in low-temperature crystallization, improving film quality and grain growth.[30,258–261] In this method, the crystallization process and thickness can be precisely controlled during spin coating by adjusting parameters such as rotation speed, deposition cycles, and precursor coating sequence.

(e) Spray pyrolysis. Spray pyrolysis is a non-vacuum, solution-based method in which a precursor solution is sprayed onto heated substrates (300–400 °C).[262] This technique has shown promise for various binary, ternary, and quaternary chalcogenides, such as Sb_2X_3, CTS, and CZTS. During the process, the precursor undergoes chemical decomposition, while the solution is transferred through a pressurized nozzle.[262,263] The composition and phase purity in this technique can be controlled through careful selection of precursors, additives, and solvents. As a low-cost and scalable method,

spray pyrolysis is ideal for producing high-quality absorber layers with improved surface coverage and uniform thickness.

Overall, physical deposition methods are essential for the precise and controlled fabrication of high-quality chalcogenide absorber layers. The vapor-phase growth of chalcogenide-based absorbers involves crucial stages like sublimation, decomposition, evaporation, and nucleation growth.[264] During each of these steps, thermal energy is used to suppress energy barriers, and various techniques can modify these critical stages to optimize film quality. The melting temperature and vapor pressure of precursor materials significantly influence the deposition process. Materials like Sb_2X_3 and some chalcogenide PSK have lower melting points and higher vapor pressures compared to other absorbers like CIGS, CdTe, and Si. It makes them suitable for deposit via physical deposition techniques. Along with physical techniques, chemical methods can play a significant role in the fabrication of chalcogenide absorber layers. Solution-based approaches such as hydrothermal, spray pyrolysis, spin coating, and CBD have been shown to produce phase-pure, less-defective absorber films with promising PCEs (e.g., Sb_2X_3, and Cu-based chalcogenide).[256,265] Hybrid approaches, where molecular inks are spin-coated followed by post-sulfurization, have also been demonstrated to yield high-quality absorber layers. These methods can further reduce the defect density, improve grain growth, and enhance the overall PCE of the device. Techniques such as spin coating and hydrothermal are suitable for lab-scale production and demonstration of 2T TSC, while other physical techniques like TE, ALD, CVD, and VTD are scalable industrial processes.[266]

5.2. Passivation of interface defects

There are several critical factors for determining PCE in SCs. One effective strategy for improving V_{oc}-deficit characteristics in top cells is surface defect passivation. Passivation layers with favorable lattice constants and dielectric properties can significantly suppress non-radiative recombination at the heterojunction interface, thereby reducing V_{oc}-deficit characteristics.[267–269] Several materials, such as Al_2O_3, HfO_2, TiO_2, $Al(OH)_3$, SnO_2, $(Zn,Sn)O$, $(Cd,Zn)S$, CdO, Sb_2O_3, Sb_2Cl_3, $(Zn,Ti)O_2$, and $Zn(O,S)$ have been investigated as passivation layers at the heterojunction.[270–272] Some dielectric passivation layers provide both chemical as well as field effect passivation. Normally, the high densities of dangling bonds from the surface of chalcogenide-based thin films and lattice mismatch easily form defects. These defects mainly deteriorate the photogenerated charge transport characteristics and result in high carrier recombination near the interface between chalcogenides/buffer and chalcogenide/transparent conductive electrode (TCEs) layers. These high interface defects assisted carrier recombination significantly affect the overall PEC of chalcogenide-based SCs. It can be investigated through transient absorption, photoluminescence (PL), Raman, admittance, and deep-level transient spectroscopy techniques.[261,265,272–276] Several research articles have emphasized different interface defect passivation strategies and their mechanisms for chalcogenide-based SCs. Strategies such as the application of a dielectric passivation layer via ALD, solution

This journal is © The Royal Society of Chemistry 2025

Energy Environ. Sci., 2025, **18**, 6899–6933 | **6917**

sulfurization, heterojunction heat treatment, re-crystallization, and others, have been reported.[277–280] The previous reports suggest defects such as (i) CIGS; Cu-, Ga-vacancies and related defect clusters (ii) CZTSSe; Cu-vacancy, Cu_{Zn} and Zn_{Sn} anti-sites and related defect clusters, and (iii) $Sb_2(S,Se)_3$; Sb-, S- or Se- vacancies and Sb_S anti-sites are detrimental defects.[272,275,276,281,282]

Upon applying a passivation layer or treatment, it interacts differently or follows distinct mechanisms. For example, ALD-deposited dielectric passivation layers provide both chemical and field-effect passivation. During the process, the oppositely charged species from ALD precursor cycles (half ALD cycles) may absorb onto the chalcogenide absorber surface, passivating dangling bonds. The fixed negative charge neutralizes positively charged defects, while positive precursor ions counteract negatively charged defects at the interface. Additionally, the fixed negative charge repels electrons from the interface, suppressing recombination near positively charged defects. This dual effect enhances both chemical and field-effect

Fig. 10   Various interface passivation strategies in chalcogenide absorber layers: (a) ALD-grown Al_2O_3 passivation on the CZTS absorber layer,[286] Reproduced with permission, Copyright 2019, Royal Society of Chemistry, (b) photoluminescence spectra of ALD-passivated CZTS absorber layers with varying thicknesses and combinations with air annealing,[293] Reproduced with permission, Copyright 2016, Wiley-VCH, (c) atomic-scale TEM image of the CdS/CZTS interface after heterojunction heat treatment,[81] Reproduced with permission, Copyright 2018, Springer nature, (d) Sb and Cl iso-surface charge distribution around the (130) surface of Sb_2S_3 along with UPS spectra after Sb_2Cl_3 treatment,[294] Reproduced with permission, Copyright 2020, American Chemical Society, and (e) schematic of solution sulfurization treatment with thioacetamide on Sb_2S_3 absorber layer, with corresponding XPS spectra before and after treatment.[295] Reproduced with permission, Copyright 2019, Wiley-VCH.

passivation.[279,280,283–285] For example, applying an Al_2O_3 layer using the ALD process provides chemical passivation through the 'H' generated during the ALD cycles. Additionally, excess 'O' during the initial growth of non-stoichiometric Al_2O_3 creates a negative charge, contributing to field-effect passivation. In kesterite, 'Al' precursor half cycles with trimethylaluminum facilitate the formation of a Cu-depleted nanolayer with a high density of 'O' and 'Na' accumulation at the surface (Fig. 10(a)). Similarly, ALD passivation combined with the air annealing process showed passivation of interface defects and pinholes in the absorber layer, reducing interface defect-assisted recombination, as verified by enhanced PL (Fig. 10(b)). Processes like heterojunction heat treatment demonstrate elemental interdiffusion mechanisms near the junction region, where the atoms from the buffer get diffused in the absorber layer passivating the defects. The well-known example of CdS/CZTS heat treatment shows 'Cd' occupies the 'Zn' site and passivates Zn-related anti-site defects (Fig. 10(c)).[81] The solution-based treatment involves the spin coating of a passivation solution (cation or anion dissolved in aqueous or organic solvent) over the absorber layer followed by post-annealing steps. In Sb_2S_3, the coating of the $SbCl_3$ layer on the Sb_2S_3 absorber layer showed the accumulation of 'Sb' and 'Cl' ions near the (130) Sb_2S_3 plane and defects. It modifies the work function and VBM of the absorber layer favoring efficient carrier transport near the Sb_2S_3/HTL interface (Fig. 10(d)). Whereas thioacetamide (TA) treatment drove the 'S' ions from the TA solution to occupy the chalcogenide absorber passivating 'S' vacancy or 'O' site (Fig. 10(e)).[278] These strategies suppress the surface recombination velocity and improve the V_{oc} and FF values in the device.[286–292]

Fig. 11 shows V_{oc} improvements for proven and emerging chalcogenide top cells by introducing various passivation layers. Notably, the combination of a sputtered Cd(O,S) passivation layer with a CBTS absorber resulted in a V_{oc}
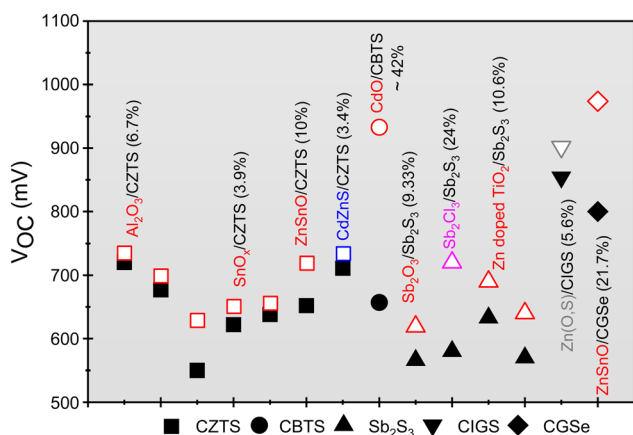
improvement of over 40%.[296] In the case of the Sb_2S_3-based top cells, V_{oc} improvements ranging from 9.3 to 24% were achieved by introducing Sb_2O_3,[297] $(Zn,Ti)O_2(ZTO)$,[298,299] or Sb_2Cl_3[300] as passivation layers. Additionally, the combinations of (i) Zn(O,S) with $Cu(In,Ga)S_2$ and (ii) ZTO with CGSe demonstrated V_{oc} improvements of 5.6 and 21.7%, respectively.[76,301] However, the V_{oc}-deficit values are still too large to achieve PCE over 16%. Previous reports suggest that complex deep-level defects in chalcogenides are the main reason for the V_{oc}-deficit.[268,296,302] Therefore, substantial efforts are needed to minimize defect-assisted recombination losses by developing and introducing novel and suitable passivation materials on chalcogenides.

5.3. Application of novel and excellent TCEs

TCEs are crucial components of TSCs. High optical transmittance ($>90\%$ in the visible wavelength) and low sheet resistance (10–25 Ω sq^{-1}) are essential factors, always presenting a trade-off. Excellent electrical properties usually come with increased light absorption, leading to lower light transmission.[296] In terms of device structure, the optoelectronic properties of top TCEs have a decisive influence on the PCE in 2T TSCs as both cells are electrically and mechanically connected.[65] Experimentally, parasitic absorption loss from TCEs contributed to a photocurrent density loss of $\sim$1 mA cm^{-2} in 2T[297] and 4–5 mA cm^{-2} in 4T[203] TSCs. The parasitic absorption losses at the front TCE in 2T TSCs occur below 550 nm, while in 4T TSCs, they mainly occur in the near-infrared region (>800 nm) due to free carrier intra-band absorption.[299] ZnO-based compounds such as i-ZnO/Al-doped ZnO (AZO) bi-layered TCEs, are typically used as top TCEs in chalcogenide single-junction SCs due to their low cost, excellent optoelectronic properties, and superior chemical and thermal stability. However, the preparation methods for ZnO-based top TCEs usually involve vacuum-based techniques (particularly the sputtering method), which can easily damage the thin buffer layer (typically less than 50–60 nm) during the deposition process.[300] Locally formed damages for CBD-CdS were observed after the sputtering process, which is shown in Fig. 12(a–d). This indicates that the sputtering-induced damage to the CBD-CdS buffer is unavoidable and can be critical, particularly for thin layers. Therefore, less or no damage preparation techniques, such as vacuum- and solution-based approaches, have been widely established.[301–304] These techniques should be deposited at low temperatures below 100 °C to avoid damaging the underlying layer. Another promising approach for minimizing damage during the preparation process involves two steps: (i) solution-based seed layer growth followed by (ii) vapor-based vacuum deposition growth.[11] These approaches minimize unfavorable defects at interfaces in 2T TSCs. Unfortunately, the widely used AZO has limitations, such as a relatively narrow E_g (3.3 eV) and poor electrical resistivity ($\sim 10^{-3}$ Ωcm), which restrict further improvements in PCE for chalcogenide-based single-junction SCs.[300,305] To address these drawbacks, several high-performance TECs have been developed, including conductive polymers (*i.e.*, PEDOT:PSS),[306–308]

Fig. 11 V_{oc} improvements observed in proven and emerging material-based SCs with various passivation layers. Hollow symbols represent V_{oc} without passivation layers, while filled symbols indicate V_{oc} with passivation layers. Colors denote different passivation types: Red for oxide-based, Blue for sulfur-based, Pink for chlorine-based, and Gray for oxy-sulfide-based layers.

This journal is © The Royal Society of Chemistry 2025
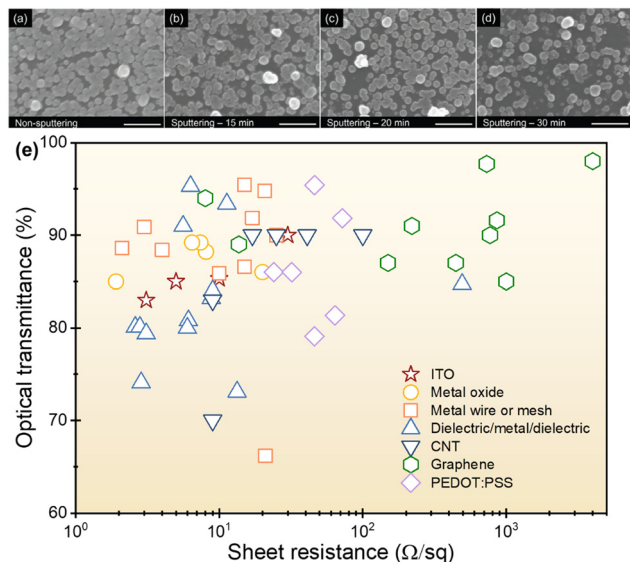
Energy Environ. Sci., 2025, **18**, 6899–6933 | **6919**

Fig. 12 Surface FE-SEM images of the CBD-CdS on a glass substrate after sputtering times of (a) 0, (b) 15, (c) 20, and (d) 30 min, respectively.[300] Reproduced with permission, Copyright 2023, Wiley-VCH, (e) Optical transmittance *vs.* sheet resistance of reported TCEs such as ITO, metal oxide, metal wire or mesh, dielectric/metal/dielectric, CNT, graphene, PEDOT:PSS.

metal (wire or mesh),[309–311] metal oxides (ZnO, TiO$_2$, or SnO$_x$ etc.),[302,312] carbon-based materials (carbon nanotube (CNT)) and graphene),[313,314] and dielectric/metal/dielectric structured materials.[305,315–317] Excellent reviews covering the fundamentals, benefits, challenges, and their applications of each material have been reported.[302,303,318–324] Fig. 12(e) shows the optical transmittance *vs.* sheet resistance of previously reported and representative TCE materials. Despite the development of TCEs with excellent optoelectronic properties, several challenges remain to be addressed for their use in TSCs:

(i) Metal-based TCEs. Vulnerability of oxygen, moisture, heat, light, and rough surfaces; rapid degradation of properties; poor long-term stability at high temperatures; and unclear degradation mechanism.[303,320]

(ii) Metal oxide-based TCEs. Challenges in achieving highly infrared-transparent conductive mechanisms; developing new metal-oxide TCE materials with controllable phase and morphology, high-crystalline quality over large areas, excellent adhesion, and flexibility in n- and p-type conductivity.[321,322]

(iii) Dielectric/metal/dielectric-based TCEs. Trade-off between optical transmittance and electrical conductivity; degradation of optoelectronic properties from mechanical stress; formation of interfacial layers at the dielectric and metal interface; chemical corrosion or oxidation.[317]

(iv) Carbon-based TCEs. Poor long-term stability of electronic properties; relatively poor conductivity; high sheet resistance; and sensitivity to water and/or oxygen.[177,302,325]

One promising approach to overcome these drawbacks is combining the outstanding conductivity of metallic nanostructures with conducting polymers or carbon-based materials to create hybrid TCEs. This combination can lead to improved electronic properties as well as mechanical stability.

5.4. Application of suitable RL

In 2T-TSCs, the RL acts as the interconnection between the top and bottom cells, it plays a crucial role in achieving high PCEs.[160] As both sub-cells are connected in series through their respective charge-collecting layers, efficient charge recombination is required for optimal performance. However, this 2T TSC configuration often leads to significant electrical losses due to interfacial resistance, which can reduce photocurrent collection and the V_{oc} of the device. To mitigate such losses, designing suitable RLs with excellent optoelectronic properties is essential. One can consider the following factors to design a suitable RL (intermediate) in highly efficient TSCs.

(i) Band alignment. Ideally, the optimal RLs should have an Ohmic contact between the emerging chalcogenide absorber-based top cell and the Si bottom cell. The proper band alignment with minimal band offset provides paths for efficient charge carrier transport and electron-hole recombination without compromising V_{oc}.

(ii) High carrier mobility and low sheet resistance. The best RLs are the ones that possess high carrier mobility, high carrier concentration, and minimal R_s. RLs with these properties provide minimal R_s and higher power output in TSCs. TCOs such as ITO or ZnO-based compounds are proven to be suitable for RLs.

(iii) Optimal thickness, transparency, and morphology. The RLs should have an optimal thickness to minimize absorption losses while maintaining high electrical conductivity. They should exhibit minimal refractive index mismatch with bottom cells, high optical transmittance, and minimal absorption at the desired thickness, as thicker RLs typically result in greater parasitic absorption losses. Additionally, RLs should have smooth morphology and maintain structural integrity to prevent shunting paths and leakage currents.

(iv) Chemical and thermal stability. The RLs should also have high thermal and chemical stability at elevated temperatures ($\sim$500 °C). As top cells like chalcogenide absorbers have relatively higher processing temperatures, the RLs must prevent oxidation, sulfurization/selenization of themselves as well as the bottom cell. Moreover, it should also prevent the interdiffusion of other elements from the top and bottom cells.

Fig. 13(a) shows the scheme, band alignment, and band position for CGSe-Si TSCs with a TCE interlayer as an RL (Intermediate). It shows a TCE interlayer with high conductivity that connects the top and bottom cells electrically, providing a high recombination site for charge carriers extracted from both cells. The introduction of reflective back contacts helps mitigate losses caused by differences in refractive index among the materials.[13] Bush *et al.*[11] successfully reported an extra J_{sc} of $\sim$1.5 mA cm^{-2} by introducing Si nanoparticles between a-Si and Ag reflector layers. In terms of band structure, photogenerated charge carriers move across each cell and then recombine at the TCE interlayer. The significant work function difference between the emitter material of the bottom Si cell
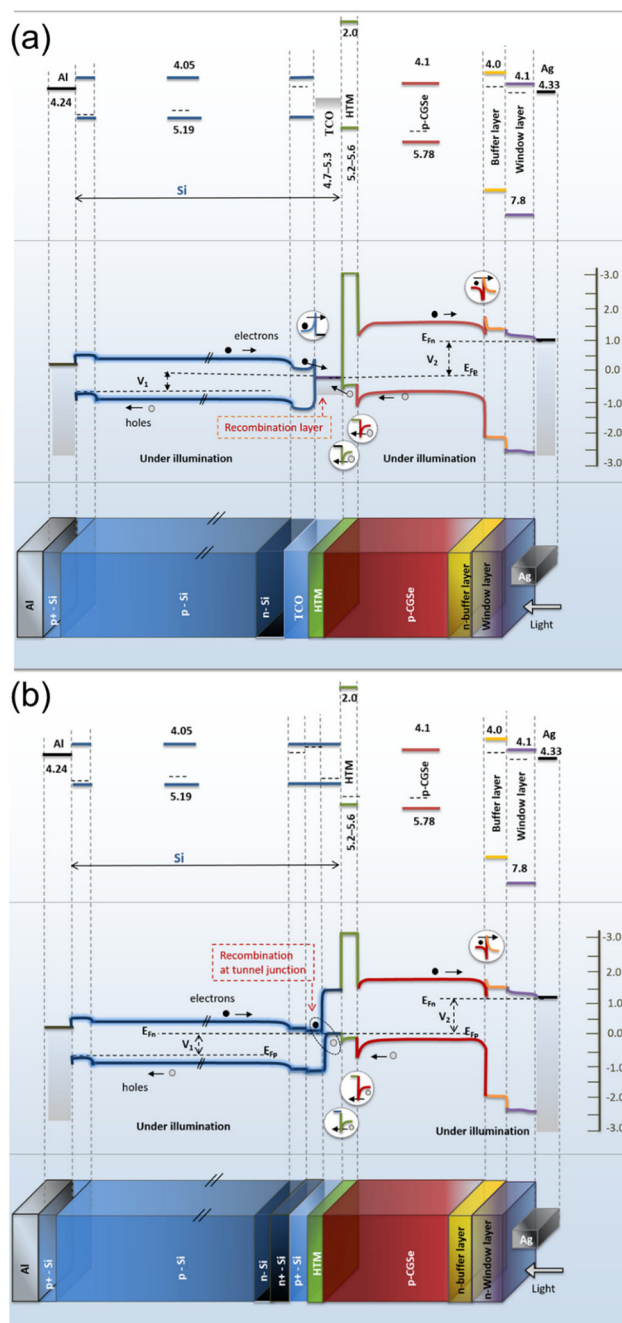
6920 | *Energy Environ. Sci.*, 2025, **18**, 6899–6933

This journal is © The Royal Society of Chemistry 2025

Fig. 13 Schemes, band alignments, and band positions for CGS-Si TSCs; (a) TEC and (b) tunnel junction as recombination junctions, respectively.[227] Reproduced with permission, Copyright 2021, Wiley-VCH.

recombination junction in all PSK and PSK-Si TSCs have been reported.[13,177,326–328] Practically, oxide-based TCEs (ITO-, ZnO-based compounds, TiO$_2$, and SnO$_2$), metallic arrays (meshes, nanowire, and ultrathin layer), conductive composite (metal-coated polymethyl methacrylate (PMMA) and oxide-metal-oxide/organic-metal–organic frameworks), and conducting polymers (poly-3-hexylthiophene, polythermide, PEDOT:PSS, phenyl-C$_{61}$-butyric acid methyl ester, Spiro-OMeTAD, carbon nanotubes, and graphene) have been utilized as RLs. Adaptable strategies for the intermediate layer as a recombination junction in chalcogenide–Si TSCs are as follows.

The oxide-based TCEs with reduced reflection loss on the bottom Si should be developed. Typically, oxide-based TCEs have <10% reflections, resulting in a J_{sc} loss of approximately ~2.2 mA cm^{-2}.[326,329] In this regard, hydrogen-doped ITO with reduced reflectance has been developed and applied to PSK-Si TSC by Knipp and co-workers.[330] The authors also supported the optical simulation process to determine a realistic description of TSCs and achieved a high J_{sc} of over 20 mA cm^{-2}. Normally, the preparation process of RLs includes vacuum-based techniques and they can mainly damage the Si bottom cells during the deposition process, resulting in poor performance in TSCs. Thus, promising strategies are introduced through low energy-based deposition processes such as solution-based approaches, ALD, soft sputtering, and CVD. The related research on outstanding performance has been investigated in TSCs.[331–335] Secondly, metal-based alloys can be considered as RL's materials to realize the 2T TSCs owing to their excellent conductivity. Metal-based RL has been introduced mainly in III–V-Si TSC.[160,336–338] Hidenori and co-workers reported the first meaningful demonstration by introducing Pd nanoparticles (less than 50 nm) between III–V and Si cells.[339] Similarly, other metal nanoparticles have been employed in between III–V and Si cells as RLs, and it suppressed the reflectance loss and exhibited low transmittance loss (~2%).[340,341] However, the light loss from contact shading is still challenging. Conductive polymers, which include either long conjugated polymer chains or large macromolecules with many conjugated carbon rings, have been studied at all PSK and PSK-Si TSCs. They can easily form mechanical bonding between top and bottom cells, provide efficient transmission of sub-E_g photons, and good carrier collection and conduction. Brabec and co-worker introduced PEDOT:PSS layer as RL between PSK and Si cells and they achieved an excellent FF value of over 80%, PCE of 21.0% as well as negligible V_{oc} loss compared to that of SC.[342] Similarly, conductive composites (i.e., normally a combination of polymers and metal alloys) can also be considered as promising RL materials owing to their strong bonding ability and excellent conductivity in TSCs, and they have good mechanical strength, easy processing, and a minimal requirement on the bonding surface. For example, Tamboli and co-workers introduced an Ag-PMMA conductive composite as RL between GaInP and Si cells and they achieved a PCE of 26.4%.[343] Here, Ag-PMMA conductive composite supported excellent carrier transport to each cell, high optical transmission, and good mechanical bonding. However, precise

and the TCE can create a high Schottky barrier, hindering electron flow from the emitter to the TCE and leading to poor device PCE. Minimizing the Schottky barrier by reducing the work function gap between the emitter in Si bottom cells and the TCE interlayer is essential. Unfortunately, the detailed studies on the band structure and alignments between recently developed TCEs as RL (intermediate) and emerging chalcogenide or buffer materials have not yet been sufficiently investigated. The excellent approaches for interconnecting layers as a

This journal is © The Royal Society of Chemistry 2025

Energy Environ. Sci., 2025, **18**, 6899–6933 | **6921**

optical and electrical property controls are essential to optimize the PCE of TSCs.

The tunnel junction approach is well developed and provides an alternative to the recombination junction, effectively suppressing the optoelectronic loss originating from the TCE interlayer in Si-based TSCs.[46,344] The low lateral conductivity of tunnel junction materials can effectively reduce the shunt path in TSC, which is a critical factor for the upscaling process. The high doping concentration in the P^+–Si layer as a tunnel junction, as shown in Fig. 13(b), creates a relatively narrow depletion region, effectively promoting charge carriers to tunnel through the junction to recombine. Furthermore, the work function of tunnel junction materials should be investigated to ensure effective ohmic contact, which suggests the formation of adjacent n-type and p-type layers simultaneously in the TSCs.[345] However, the recombination current density originating from the tunnel junction layer significantly suppresses the overall photocurrent density of tandems, which is a thorny challenge for improving PCE.

5.5. Maximizing light capture in TSCs

Light management, including reducing parasitic absorption losses and optimizing light incidence, is critical for further improving the overall PCE of TSCs. Firstly, parasitic absorption losses occur due to thick absorber layers and the absorbing characteristics of contact or interfacial layers and TCEs with high charge carrier absorption in near-infrared radiation.[346] The design involving optical modeling can minimize the reflection peaks, allowing infrared radiation and visible light to be effectively absorbed by the bottom and top cells, respectively.[347,348] However, challenges remain in the optical modeling, simulation, and practical experimental studies on suitable interfacial materials with various refractive indices to further improve PCE performance in emerging inorganic chalcogenide–Si TSCs.

Secondly, improving light incidence can be achieved by introducing wide E_g interfacial materials (i.e., buffer, hole transfer layers, and TCEs), increasing the transmittance of top cells, and surface texture in bottom Si cells. Commonly, CBD-CdS has been widely used as a buffer layer due to its suitable E_g (~2.4 eV) and favorable band alignment with a conduction band offset (CBO) value of +0.1–0.3 eV.[49,233,300,305] However, the high absorption coefficient of CdS buffer results in a J_{sc} loss of about 1–2 mA cm^{-2}.[233] Simulations for kesterite-Si TSCs suggest a 4–14% relative reduction in the theoretical J_{sc} value. To improve light incidence in TSCs, extensive research and development of buffer materials with lower absorption coefficients, and wider and adjustable E_g are highly desirable. Wider E_g buffer materials show higher transmittance in the 350–500 nm wavelength range, leading to higher EQE (Fig. 14(a)), enhanced V_{oc} value, and improved PCE performance. Although several investigations into wider E_g buffer materials have been conducted for emerging inorganic chalcogenide single-junction SCs, their PCE performance has not yet matched that of CdS buffer due to improper band alignments (i.e., large CBO value).

The incidence of light on the bottom Si cell is primarily limited by the E_g of the top cell, as only photons with energy greater than E_g can reach the bottom cell. The PCE of TSCs is determined by adjusting the E_g, CBO, and transmittance in the top cell, as shown in Fig. 14(b). The PCE for TSCs decreases with increasing E_g in the top cell. Top cells with PCE ranging from 13 to 15%, E_g from 1.55 to 1.7 eV, and high transmittance over 85% have already been achieved, increasing the PCE of TSCs from 0.4 to 1.5% compared to the bottom Si cell alone.[233] However, a wider E_g and over 80% of transmittance in the top cell are still insufficient to achieve PCE performance for TSCs over 26%.

5.6. Long-terms stability, large-scale production, and outdoor test

The PCE degradation of TSCs is a critical factor in producing low-cost electricity.[350,351] It is essential to have a deep understanding and insight into degradation mechanisms to achieve
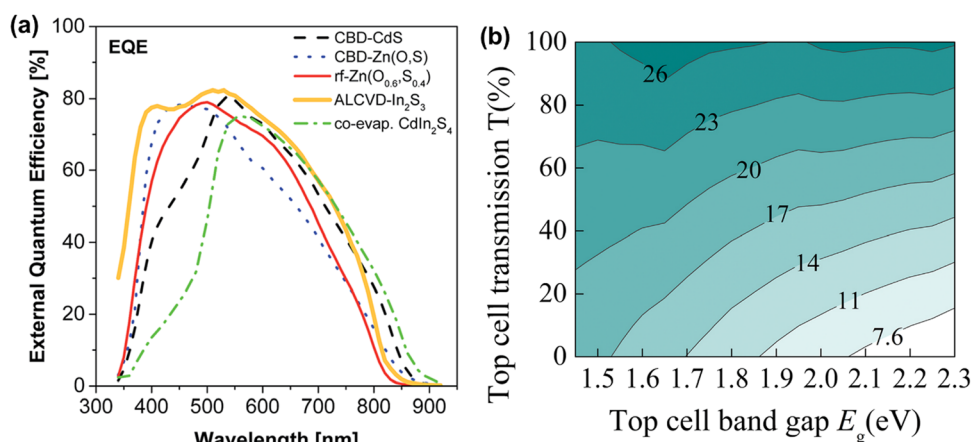

Fig. 14 (a) EQE spectra of kesterite-based single-junction SCs with different buffer layers.[233] Reproduced with permission, Copyright 2019, Royal Society of Chemistry, (b) device performances of TSCs as a function of E_g and transmittance of top cells.[349] Reproduced with permission, Copyright 2021, Elsevier.
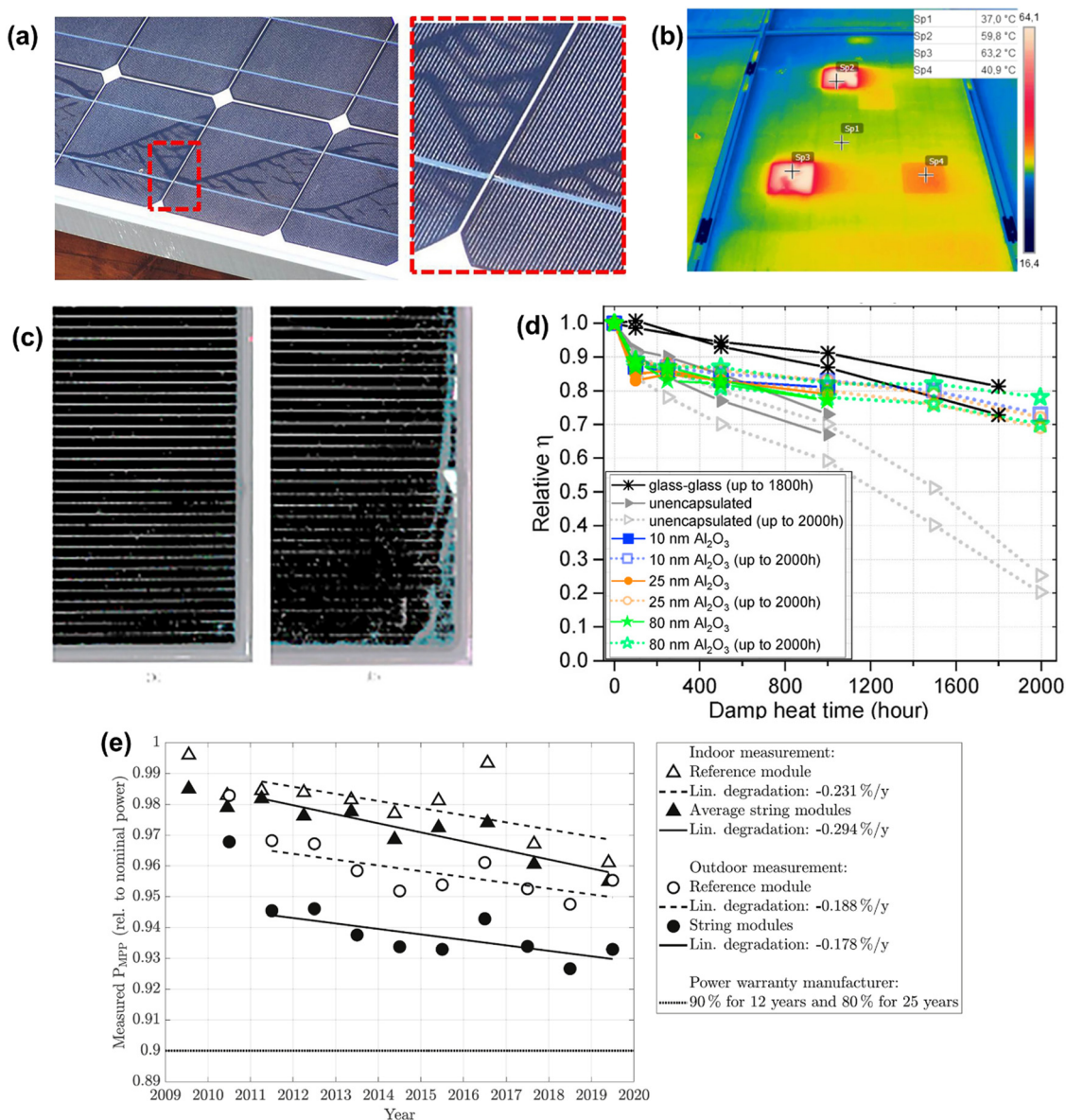
6922 | *Energy Environ. Sci.*, 2025, **18**, 6899–6933

This journal is © The Royal Society of Chemistry 2025

Fig. 15 (a) Photograph of snail trails,[357] Reproduced with permission, Copyright 2021, Elsevier. (b) Thermal infrared photograph on Si module.[352] Reproduced with permission, Copyright 2022, Willey-VCH (c) Photograph of CdTe module after voltage stress of −1000 V during 1043 h under damp heat test conditions, reproduced with permission, copyright 2021, SPIE.[358] (d) Damp heat test results for CIGS SCs without and with encapsulation and passivation of Al_2O_3.[359] Reproduced with permission, Copyright 2018, Elsevier, (e) Long-term device performance of Si SCs under indoor and outdoor conditions.[360] Reproduced with permission, Copyright 2021, Elsevier.

long-term stability. For Si-based single-junction SCs, degradation mechanisms have been extensively investigated, with the main causes being mechanical stress, cracked cells, snail trails, hot spots, and high voltage damage (Fig. 15(a–c)), potential induced degradation, light-induced degradation, and light and elevated temperature induced degradation.[352–356]

Most of these degradation issues have been resolved, and commercialized Si-based single-junction SCs can secure a PCE of over 80% with a warranted lifetime of over 25 years.[350] However, emerging inorganic chalcogenide-based single-junction SCs remain less extensively studied and have not achieved long-term stability like Si SCs. The stability failure

summary of chalcogenide absorbers, including CIGS, CZTSSe, and $Sb_2(S,Se)_3$, is shown in Table S4 and Note 2, ESI.† For kesterite and $Sb_2(S,Se)_3$ the instability of the charge transport layer (HTL/ETL) or the degradation of the TCO layer is reported as the main cause of stability failure. Among inorganic chalcogenides, the CIGSe-based single-junction SCs have been relatively well investigated.[352,359] Their common failure mode includes alkali elements migration and buffer, and TCO layer degradation. One promising approach for improving long-term stability involves introducing H_2O-resistant inorganic thin layers (i.e., Al_2O_3, TiO_2, and SnO_2) between polymeric front and back sheets as encapsulation materials (Fig. 15(d)).[361,362]

This journal is © The Royal Society of Chemistry 2025

Energy Environ. Sci., 2025, 18, 6899–6933 | 6923

The CIGS-based module without encapsulation shows a considerable loss in FF during the first 100 h of damp heat testing, primarily due to shunt paths from the degradation of AZO. In contrast, the ALD-Al_2O_3 encapsulated CIGSe-based module showed better long-term stability over 2000 h of damp heat testing due to reduced humidity penetration.

All PV devices are installed outdoors, making long-term stability investigations crucial for achieving cost-effective electricity. Carigiet et al.[363] reported an interesting review of long-term stability for Si-based modules under indoor and outdoor conditions. The annual degradation rate was estimated to be $0.29 \pm 0.06\%$ for a string in indoor conditions, while that of outdoor conditions ($0.18 \pm 0.06\%$) was lower, as shown in Fig. 15(e). However, the difference between indoor and outdoor conditions is negligible and represents only one site result. Therefore, more comparative research is needed to analyze various conditions comprehensively. Unfortunately, higher annual PCE degradation rates per year for single-junction SCs (i.e., HIT cells) have been reported, highlighting the need for in-depth investigation and insight into long-term stability for emerging inorganic chalcogenides.

6. Summary and perspective

This review discusses emerging inorganic chalcogenide-based Si TSCs as a promising solution to the PCE and long-term stability limitations faced by single-junction SCs. We began by outlining the current status and issues with single-junction SCs and existing TSC technologies needed for the development of emerging inorganic chalcogenide–Si TSCs. Subsequently, we briefly summarized the principles of TSCs (i.e., maximum light utilization of light, suitable interconnecting layers, optical design, E_g, and stacking orders) and current challenges for previously reported III–V-Si and PSK-Si TSCs. In Section 3, we focused on the optoelectronic properties (Table 1) and current PCE status (Fig. 2) of proven chalcogenides (i.e., chalcopyrite, kesterite, and Sb_2S_3), emerging chalcogenides (i.e., group IV metal binary and I–V–VI_2 ternary compounds), and chalcogenide PSKs. The different optoelectronic properties and single-junction SCs PCE progress give brief ideas and research directions for chalcogenide-based absorber materials suitable for TSCs. We then explored the opportunities for Si as a suitable bottom cell and potential top candidates in emerging chalcogenide–Si TSC. In addition to highlighting some promising progress in CZTS-Si, CGSe-Si, and Sb_2S_3-Si tandems, the E_g-based evaluation of different chalcogenide absorbers showed absorbers such as CGSe and Sb_2S_3 can be promising materials with close match E_g values of 1.65–1.75 eV. Finally, following the recent progress, we discussed the key challenges and potential solutions for emerging inorganic chalcogenide–Si TSCs including fabrication complexity, achieving well-matched E_g in each cell, improving top cell efficiency, reducing recombination losses, maximizing light capture, ensuring long-term stability, and the need for outdoor performance testing. This review not only provides new insights into promising inorganic material systems as top cells in the Si-based TSCs but also outlines further research direction for early-stage development and commercialization of these promising emerging inorganic chalcogenide–Si TSCs.

Data availability

No primary research results, software or code have been included, and no new data were generated or analyzed as part of this review.

Conflicts of interest

There are no conflicts to declare.

Acknowledgements

References

1 M. A. Green, Nat. Energy, 2016, 1, 1–4.
2 S. Sivaraj, R. Rathanasamy, G. V. Kaliyannan, H. Panchal, A. Jawad Alrubaie, M. Musa Jaber, Z. Said and S. Memon, Energies, 2022, 15, 8688.
3 W. Shockley and H. J. Queisser, J. Appl. Phys., 1961, 32, 510.
4 A. W. Y. Ho-Baillie, J. Zheng, M. A. Mahmud, F.-J. Ma, D. R. McKenzie and M. A. Green, Appl. Phys. Rev., 2021, 8, 041307.
5 P. Kumar, S. Thokala, S. P. Singh and R. Singh, Nano Energy, 2024, 121, 109175.
6 K. Alberi, J. J. Berry, J. J. Cordell, D. J. Friedman, J. F. Geisz, A. R. Kirmani, B. W. Larson, W. E. Mcmahon, L. M. Mansfield, P. F. Ndione, M. Owen-Bellini, A. F. Palmstrom, M. O. Reese, S. B. Reese, M. A. Steiner, A. C. Tamboli, S. Theingi and E. L. Warren, Joule, 2024, 8, 658–692.

7 H. Li and W. Zhang, *Chem. Rev.*, 2020, **120**, 9835–9950.

8 J. F. Geisz, R. M. France, K. L. Schulte, M. A. Steiner, A. G. Norman, H. L. Guthrey, M. R. Young, T. Song and T. Moriarty, *Nat. Energy*, 2020, **5**, 326–335.

9 M. N. Sharif, J. Yang, X. Zhang, Y. Tang and K. F. Wang, *Solar RRL*, 2023, **7**, 2300156.

10 X. Liu, J. Zhang, L. Tang, J. Gong, W. Li, Z. Ma, Z. Tu, Y. Li, R. Li, X. Hu, C. Shen, H. Wang, Z. Wang, Q. Lin, G. Fang, S. Wang, C. Liu, Z. Zhang, J. Li and X. Xiao, *Energy Environ. Sci.*, 2023, **16**, 5029–5042.

11 K. A. Bush, A. F. Palmstrom, Z. J. Yu, M. Boccard, R. Cheacharoen, J. P. Mailoa, D. P. McMeekin, R. L. Z. Hoye, C. D. Bailie, T. Leijtens, I. M. Peters, M. C. Minichetti, N. Rolston, R. Prasanna, S. Sofia, D. Harwood, W. Ma, F. Moghadam, H. J. Snaith, T. Buonassisi, Z. C. Holman, S. F. Bent and M. D. McGehee, *Nat. Energy*, 2017, **2**, 1–7.

12 C. U. Kim, E. D. Jung, Y. W. Noh, S. K. Seo, Y. Choi, H. Park, M. H. Song and K. J. Choi, *EcoMat*, 2021, **3**, e12084.

13 T. Leijtens, K. A. Bush, R. Prasanna and M. D. McGehee, *Nat. Energy*, 2018, **3**, 828–838.

14 K. Dolia, S. Neupane, S. Fu, Y. Yin, A. Abudulimu, A. Rahimi, M. Hattarki, B. Dokken, T. Zhu, A. Adhikari, M. K. Jamarkattel, R. E. Irving, A. B. Phillips, M. J. Heben, R. J. Ellingson, Y. Yan and Z. Song, *Solar RRL*, 2024, 2400148.

15 E.-B. Kim, M. S. Akhtar, C. Liu, Y. Wang and S. Ameen, *J. Mater. Chem. A*, 2024, **12**, 12262–12273.

16 HZB Sets New World Record for CIGS Perovskite Tandem Solar Cells – Helmholtz-Zentrum Berlin (HZB), **https://www.helmholtz-berlin.de/pubbin/news_seite?nid=28846&sprache=en&seitenid=1**, (accessed 15 March 2025).

17 H. Liang, J. Feng, C. D. Rodríguez-Gallegos, M. Krause, X. Wang, E. Alvianto, R. Guo, H. Liu, R. K. Kothandaraman, R. Carron, A. N. Tiwari, I. M. Peters, F. Fu and Y. Hou, *Joule*, 2023, **7**, 2859–2872.

18 Interactive Best Research-Cell Efficiency Chart|Photovoltaic Research|NREL, **https://www.nrel.gov/pv/interactive-cell-efficiency.html**, (accessed 25 May 2024).

19 M. A. Green, E. D. Dunlop, M. Yoshita, N. Kopidakis, K. Bothe, G. Siefer and X. Hao, *Prog. Photovoltaics Res. Appl.*, 2024, **32**, 3–13.

20 Longi claims 34.6% efficiency for perovskite-silicon tandem solar cell – pv magazine International, **https://www.pv-magazine.com/2024/06/14/longi-claims-34-6-efficiency-for-perovskite-silicon-tandem-solar-cell/**, (accessed 17 June 2024).

21 T. White, N. Lal and K. Catchpole, *IEEE J. Photovoltaics*, 2014, **4**, 208–214.

22 M. A. Fazal and S. Rubaiee, *Sol. Energy*, 2023, **258**, 203–219.

23 L. Duan, D. Walter, N. Chang, J. Bullock, D. Kang, S. P. Phang, K. Weber, T. White, D. Macdonald, K. Catchpole and H. Shen, *Nat. Rev. Mater.*, 2023, **8**, 261–281.

24 C. Messmer, B. S. Goraya, S. Nold, P. S. C. Schulze, V. Sittinger, J. Schön, J. C. Goldschmidt, M. Bivour, S. W. Glunz and M. Hermle, *Prog. Photovoltaics Res. Appl.*, 2021, **29**, 744–759.

25 H. Zhang, X. Fu, Y. Tang, H. Wang, C. Zhang, W. W. Yu, X. Wang, Y. Zhang and M. Xiao, *Nat. Commun.*, 2019, **10**, 1088.

26 W. Mao, C. R. Hall, S. Bernardi, Y. B. Cheng, A. Widmer-Cooper, T. A. Smith and U. Bach, *Nat. Mater.*, 2020, **20**, 55–61.

27 S. Hadke, M. Huang, C. Chen, Y. F. Tay, S. Chen, J. Tang and L. Wong, *Chem. Rev.*, 2022, **122**, 10170–10265.

28 F. Liu, Q. Zeng, J. Li, X. Hao, A. Ho-Baillie, J. Tang and M. A. Green, *Mater. Today*, 2020, **41**, 120–142.

29 B. Saparov, *Chem. Rev.*, 2022, **122**, 10575–10577.

30 J. W. Turnley and R. Agrawal, *Chem. Commun.*, 2024, **60**, 5245–5269.

31 M. A. Green, E. D. Dunlop, M. Yoshita, N. Kopidakis, K. Bothe, G. Siefer, X. Hao and J. Y. Jiang, *Prog. Photovoltaics Res. Appl.*, 2025, **33**, 3–15.

32 V. Karade, A. Lokhande, P. Babar, M. G. Gang, M. Suryawanshi, P. Patil and J. H. Kim, *Sol. Energy Mater. Sol. Cells*, 2019, **200**, 109911.

33 E. Raza and Z. Ahmad, *Energy Rep.*, 2022, **8**, 5820–5851.

34 F. Larsson, N. S. Nilsson, J. Keller, C. Frisk, V. Kosyak, M. Edoff and T. Törndahl, *Prog. Photovoltaics Res. Appl.*, 2017, **25**, 755–763.

35 G. Regmi, A. Ashok, P. Chawla, P. Semalti, S. Velumani, S. N. Sharma and H. Castaneda, *J. Mater. Sci.: Mater. Electron.*, 2020, **31**, 7286–7314.

36 M. Hermle, F. Feldmann, M. Bivour, J. C. Goldschmidt and S. W. Glunz, *Appl. Phys. Rev.*, 2020, **7**, 021305.

37 Z. Zhang, Z. Li, L. Meng, S. Y. Lien and P. Gao, *Adv. Funct. Mater.*, 2020, **30**, 2001904.

38 Z. Wang, Z. Song, Y. Yan, S. (Frank) Liu and D. Yang, *Adv. Sci.*, 2019, **6**, 1801704.

39 S. Resalati, T. Okoroafor, A. Maalouf, E. Saucedo and M. Placidi, *Appl. Energy*, 2022, **313**, 118888.

40 M. F. Mohamad Noh, N. A. Arzaee, C. C. Fat, T. Sieh Kiong, M. A. Mat Teridi and A. W. Mahmood Zuhdi, *Mater. Today Energy*, 2024, **39**, 101473.

41 S. Akhil, S. Akash, A. Pasha, B. Kulkarni, M. Jalalah, M. Alsaiari, F. A. Harraz and R. G. Balakrishna, *Mater. Des.*, 2021, **211**, 110138.

42 Y. Ko, H. Park, C. Lee, Y. Kang, Y. Jun, Y. Ko, C. Lee, Y. Kang, Y. Jun and H. Park, *Adv. Mater.*, 2020, **32**, 2002196.

43 J. H. Park, S. K. Hwang, S. G. Ji and J. Y. Kim, *Exploration*, 2023, **3**, 20220029.

44 H. Li and W. Zhang, *Chem. Rev.*, 2020, **120**, 9835–9950.

45 O. Ramírez, E. M. Lanzoni, R. G. Poeira, T. P. Weiss, R. Leturcq, A. Redinger and S. Siebentritt, *APL Mater.*, 2022, **10**, 61108.

46 M. Nakamura, K. Yamaguchi, Y. Kimoto, Y. Yasaki, T. Kato and H. Sugimoto, *IEEE J. Photovoltaics*, 2019, **9**, 1863–1867.

47 K. S. Gour, V. Karade, P. Babar, J. Park, D. M. Lee, V. N. Singh and J. H. Kim, *Solar RRL*, 2021, **5**, 2000815.

48 E. M. Mkawi, *Results Phys.*, 2020, **19**, 103603.

49 G. U. Kamble, S. W. Shin, S. W. Park, M. A. Gaikwad, V. C. Karade, J. S. Jang, Y. Park, U. V. Ghorpade, M. P. Suryawanshi and J. H. Kim, *Solar RRL*, 2023, **7**, 2300502.

This journal is © The Royal Society of Chemistry 2025

Energy Environ. Sci., 2025, **18**, 6899–6933 | **6925**

50 L. A. Burton, D. Colombara, R. D. Abellon, F. C. Grozema, L. M. Peter, T. J. Savenije, G. Dennler and A. Walsh, *Chem. Mater.*, 2013, **25**, 4908–4916.

51 E. Barrios Salgado, D. Eréndira Lara Llanderal, M. T. S. Nair, W. Zhang, Y. Cheng, J. Zhao, Y. Gupta, P. Arun, I. Suzuki, S. Kawanishi, T. Omata and H. Yanagi, *J. Phys.: Energy*, 2022, **4**, 042002.

52 L. Mehdaoui, R. Miloua, M. Khadraoui, M. O. Bensaid, D. Abdelkader, F. Chiker and A. Bouzidi, *Phys. B*, 2019, **564**, 114–124.

53 M. Choi, S. Kim, M. Lee, J. S. Yun, V. C. Karade, J. Lim, J. Y. Yang and J. Park, *J. Mater. Chem. A*, 2024, **12**, 16831–16838.

54 A. M. Medina-Gonzalez, B. A. Rosales, U. H. Hamdeh, M. G. Panthani and J. Vela, *Chem. Mater.*, 2020, **32**, 6085–6096.

55 M. Kumar, A. Singh, D. Gill and S. Bhattacharya, *J. Phys. Chem. Lett.*, 2021, **12**, 5301–5307.

56 K. V. Sopiha, C. Comparotto, J. A. Márquez and J. J. S. Scragg, *Adv. Opt. Mater.*, 2022, **10**, 2101704.

57 O. Almora, G. C. Bazan, C. I. Cabrera, L. A. Castriotta, S. Erten-Ela, K. Forberich, K. Fukuda, F. Guo, J. Hauch, A. W. Y. Ho-Baillie, T. J. Jacobsson, R. A. J. Janssen, T. Kirchartz, R. R. Lunt, X. Mathew, D. B. Mitzi, M. K. Nazeeruddin, J. Nelson, A. F. Nogueira, U. W. Paetzold, B. P. Rand, U. Rau, T. Someya, C. Sprau, L. Vaillant-Roca, C. J. Brabec, O. Almora, C. J. Brabec, G. C. Bazan and L. A. Castriotta, *Adv. Energy Mater.*, 2024, 2404386.

58 O. Almora, D. Baran, G. C. Bazan, C. I. Cabrera, S. Erten-Ela, K. Forberich, F. Guo, J. Hauch, A. W. Y. Ho-Baillie, T. J. Jacobsson, R. A. J. Janssen, T. Kirchartz, N. Kopidakis, M. A. Loi, R. R. Lunt, X. Mathew, M. D. McGehee, J. Min, D. B. Mitzi, M. K. Nazeeruddin, J. Nelson, A. F. Nogueira, U. W. Paetzold, B. P. Rand, U. Rau, H. J. Snaith, E. Unger, L. Vaillant-Roca, C. Yang, H. L. Yip and C. J. Brabec, *Adv. Energy Mater.*, 2022, **13**, 2203313.

59 O. Almora, C. I. Cabrera, S. Erten-Ela, K. Forberich, K. Fukuda, F. Guo, J. Hauch, A. W. Y. Ho-Baillie, T. J. Jacobsson, R. A. J. Janssen, T. Kirchartz, M. A. Loi, X. Mathew, D. B. Mitzi, M. K. Nazeeruddin, U. W. Paetzold, B. P. Rand, U. Rau, T. Someya, E. Unger, L. Vaillant-Roca and C. J. Brabec, *Adv. Energy Mater.*, 2024, **14**, 2303173.

60 R. K. Yadav, P. S. Pawar, Y. T. Kim, I. Sharma and J. Heo, *J. Mater. Chem. A*, 2024, **12**, 3265–3275.

61 S. Barthwal, R. Kumar and S. Pathak, *ACS Appl. Energy Mater.*, 2022, **5**, 6545–6585.

62 Y. Zhou, L. Wang, S. Chen, S. Qin, X. Liu, J. Chen, D. J. Xue, M. Luo, Y. Cao, Y. Cheng, E. H. Sargent and J. Tang, *Nat. Photonics*, 2015, **9**, 409–415.

63 R. Kondrotas, C. Chen and J. Tang, *Joule*, 2018, **2**, 857–878.

64 X. Liu, Z. Cai, L. Wan, P. Xiao, B. Che, J. Yang, H. Niu, H. Wang, J. Zhu, Y. T. Huang, H. Zhu, S. J. Zelewski, T. Chen, R. L. Z. Hoye and R. Zhou, *Adv. Mater.*, 2024, **36**, 2305841.

65 U. Ali Shah, S. Chen, G. Mohamed Gomaa Khalaf, Z. Jin, H. Song, U. A. Shah, S. Chen, G. M. G. Khalaf, Z. Jin and H. Song, *Adv. Funct. Mater.*, 2021, **31**, 2100265.

66 M. R. Filip, C. E. Patrick and F. Giustino, *Phys. Rev. B: Condens. Matter Mater. Phys.*, 2013, **87**, 205125.

67 S. Wang, Y. Zhao, B. Che, C. Li, X. Chen, R. Tang, J. Gong, X. Wang, G. Chen, T. Chen, J. Li and X. Xiao, *Adv. Mater.*, 2022, **34**, 2206242.

68 R. Tang, X. Wang, C. Jiang, S. Li, G. Jiang, S. Yang, C. Zhu and T. Chen, *J. Mater. Chem. A*, 2018, **6**, 16322–16327.

69 Y. Huang, H. Gao, X. Peng, G. Wang, P. Xiao, B. Che, R. Tang, C. Zhu and T. Chen, *Solar RRL*, 2023, **7**, 2201115.

70 L. Zhang, W. Lian, X. Zhao, Y. Yin, T. Chen and C. Zhu, *ACS Appl. Energy Mater.*, 2020, **3**, 12417–12422.

71 C. Jiang, R. Tang, X. Wang, H. Ju, G. Chen and T. Chen, *Solar RRL*, 2019, **3**, 1800272.

72 G. Shen, A. Ke, S. Chen, T. Ma, S. Ali, M. Li, H. Y. Hsu, C. Chen, P. Yang, H. Song and J. Tang, *Adv. Energy Mater.*, 2025, 2406051.

73 Y. Zhao, W. Xu, J. Wen, X. Wang, X. Chen, B. Che, H. Wang, J. Gong, T. Chen, X. Xiao, J. Li, Y. Zhao, X. Chen, J. Gong, X. Xiao, J. Li, W. Xu, J. Wen, X. Wang, B. Che, H. Wang and T. Chen, *Adv. Mater.*, 2024, **36**, 2410669.

74 S. Suresh and A. R. Uhl, *Adv. Energy Mater.*, 2021, **11**, 2003743.

75 B. J. Stanbery, *Crit. Rev. Solid State Mater. Sci.*, 2002, **27**, 73–117.

76 S. Shukla, M. Sood, D. Adeleye, S. Peedle, G. Kusch, D. Dahliah, M. Melchiorre, G. M. Rignanese, G. Hautier, R. Oliver and S. Siebentritt, *Joule*, 2021, **5**, 1816–1831.

77 S. Ishizuka, A. Yamada, P. J. Fons, H. Shibata and S. Niki, *Prog. Photovoltaics*, 2014, **22**, 821–829.

78 A. Walsh, S. Chen, S. H. Wei and X. G. Gong, *Adv. Energy Mater.*, 2012, **2**, 400–409.

79 T. Gershon, K. Sardashti, O. Gunawan, R. Mankad, S. Singh, Y. Seog Lee, J. A. Ott, A. Kummel and R. Haight, *Adv. Energy Mater.*, 2016, **6**, 1601182.

80 L. Weston and C. Stampfl, *Phys. Rev. Mater.*, 2018, **2**, 085407.

81 C. Yan, J. Huang, K. Sun, S. Johnston, Y. Zhang, H. Sun, A. Pu, M. He, F. Liu, K. Eder, L. Yang, J. M. Cairney, N. J. Ekins-Daukes, Z. Hameiri, J. A. Stride, S. Chen, M. A. Green and X. Hao, *Nat. Energy*, 2018, **3**, 764–772.

82 S. Das and P. Mahanandia, *Mater. Chem. Phys.*, 2022, **281**, 125878.

83 P. Fan, J. Lin, J. Hu, Z. Yu, Y. Zhao, S. Chen, Z. Zheng, J. Luo, G. Liang, Z. Su, P. Fan, J. Lin, J. Hu, Z. Yu, Y. Zhao, S. Chen, Z. Zheng, J. Luo, G. Liang and Z. Su, *Adv. Funct. Mater.*, 2022, **32**, 2207470.

84 P. Sinsermsuksakul, L. Sun, S. Woon Lee, H. Hejin Park, S. Bok Kim, C. Yang, R. G. Gordon, P. Sinermsuksakul, S. B. Kim, R. G. Gordon, L. Sun, H. H. Park, C. Yang and S. S. W. Lee, *Adv. Energy Mater.*, 2014, **4**, 1400496.

85 H. S. Yun, B. Wook Park, Y. C. Choi, J. Im, T. J. Shin and S. Il Seok, *Adv. Energy Mater.*, 2019, **9**, 1901343.

86 D. Lim, H. Suh, M. Suryawanshi, G. Yeom Song, J. Yu Cho, J. Hyeok Kim, J. Hyuck Jang, C.-W. Jeon, A. Cho, S. Ahn, J. Heo, D. Lim, M. Suryawanshi, G. Y. Song, J. Y. Cho, J. H. Kim, J. Heo, H. Suh, J. H. Jang, C. Jeon, A. Cho and S. Ahn, *Adv. Energy Mater.*, 2018, **8**, 1702605.

6926 | *Energy Environ. Sci.*, 2025, **18**, 6899–6933

This journal is © The Royal Society of Chemistry 2025

87 S. C. Liu, C. M. Dai, Y. Min, Y. Hou, A. H. Proppe, Y. Zhou, C. Chen, S. Chen, J. Tang, D. J. Xue, E. H. Sargent and J. S. Hu, *Nat. Commun.*, 2021, **12**, 1–7.

88 K. Wang, H. Ni, W. Zhao, X. Wu, Y. Hu, G. Xiao and F. Jiang, *Energy Environ. Sci.*, 2023, **16**, 1155–1165.

89 D. J. Xue, S. C. Liu, C. M. Dai, S. Chen, C. He, L. Zhao, J. S. Hu and L. J. Wan, *J. Am. Chem. Soc.*, 2017, **139**, 958–965.

90 P. Sinsermsuksakul, R. Chakraborty, S. B. Kim, S. M. Heald, T. Buonassisi and R. G. Gordon, *Chem. Mater.*, 2012, **24**, 4556–4562.

91 G. Radovsky, R. Popovitz-Biro, M. Staiger, K. Gartsman, C. Thomsen, T. Lorenz, G. Seifert, R. Tenne, M. Staiger, C. Thomsen, T. Lorenz and G. Seifert, *Angew. Chem.*, 2011, **123**, 12524–12528.

92 A. Rabkin, S. Samuha, R. E. Abutbul, V. Ezersky, L. Meshi and Y. Golan, *Nano Lett.*, 2015, **15**, 2174–2179.

93 P. Sinsermsuksakul, J. Heo, W. Noh, A. S. Hock and R. G. Gordon, *Adv. Energy Mater.*, 2011, **1**, 1116–1125.

94 Z. Deng, D. Cao, J. He, S. Lin, S. M. Lindsay and Y. Liu, *ACS Nano*, 2012, **6**, 6197–6207.

95 S. Sovizi, S. Angizi, S. A. Ahmad Alem, R. Goodarzi, M. R. R. Taji Boyuk, H. Ghanbari, R. Szoszkiewicz, A. Simchi and P. Kruse, *Chem. Rev.*, 2023, **123**, 13869–13951.

96 B. Mukherjee, E. S. Tok and C. H. Sow, *J. Appl. Phys.*, 2013, **114**, 134302.

97 S. C. Liu, C. M. Dai, Y. Min, Y. Hou, A. H. Proppe, Y. Zhou, C. Chen, S. Chen, J. Tang, D. J. Xue, E. H. Sargent and J. S. Hu, *Nat. Commun.*, 2021, **12**, 1–7.

98 Y. T. Huang, S. R. Kavanagh, M. Righetto, M. Rusu, I. Levine, T. Unold, S. J. Zelewski, A. J. Sneyd, K. Zhang, L. Dai, A. J. Britton, J. Ye, J. Julin, M. Napari, Z. Zhang, J. Xiao, M. Laitinen, L. Torrente-Murciano, S. D. Stranks, A. Rao, L. M. Herz, D. O. Scanlon, A. Walsh and R. L. Z. Hoye, *Nat. Commun.*, 2022, **13**, 1–13.

99 S. Akhil and R. G. Balakrishna, *J. Mater. Chem. A*, 2022, **10**, 8615–8625.

100 Y. Wang, S. R. Kavanagh, I. Burgués-Ceballos, A. Walsh, D. Scanlon and G. Konstantatos, *Nat. Photonics*, 2022, **16**, 235–241.

101 M. Bernechea, N. C. Miller, G. Xercavins, D. So, A. Stavrinadis and G. Konstantatos, *Nat. Photonics*, 2016, **10**, 521–525.

102 Y. Wang, L. Peng, Z. Wang and G. Konstantatos, *Adv. Energy Mater.*, 2022, **12**, 2200700.

103 S. L. Diedenhofen, M. Bernechea, K. M. Felter, F. C. Grozema and L. D. A. Siebbeles, *Solar RRL*, 2019, **3**, 1900075.

104 P. C. Huang, W. C. Yang and M. W. Lee, *J. Phys. Chem. C*, 2013, **117**, 18308–18314.

105 S. N. Guin and K. Biswas, *Chem. Mater.*, 2013, **25**, 3225–3231.

106 L. Mehdaoui, R. Miloua, M. Khadraoui, M. O. Bensaid, D. Abdelkader, F. Chiker and A. Bouzidi, *Phys. B*, 2019, **564**, 114–124.

107 F. Viñes, M. Bernechea, G. Konstantatos and F. Illas, *Phys. Rev. B*, 2016, **94**, 235203.

108 S. Geller and J. H. Wernick, *Acta Crystallogr.*, 1959, **12**, 46–54.

109 A. C. Glatz and A. Pinella, *J. Mater. Sci.*, 1968, **3**, 498–501.

110 F. Viñes, G. Konstantatos and F. Illas, *Phys. Chem. Chem. Phys.*, 2017, **19**, 27940–27944.

111 A. Zanatta and I. Chambouleyron, *Phys. Rev. B:Condens. Matter Mater. Phys.*, 1996, **53**, 3833.

112 L. Mehdaoui, R. Miloua, M. Khadraoui, M. O. Bensaid, D. Abdelkader, F. Chiker and A. Bouzidi, *Phys. B*, 2019, **564**, 114–124.

113 B. Pejova, I. Grozdanov, D. Nesheva and A. Petrova, *Chem. Mater.*, 2008, **20**, 2551–2565.

114 X. Li, H. Yu, X. Ma, Z. Liu, J. Huang, Y. Shen and M. Wang, *Chem. Eng. J.*, 2024, **495**, 153328.

115 R. Syam Kumar, A. Akande, F. El-Mellouhi, H. Park and S. Sanvito, *Phys. Rev. Mater.*, 2020, **4**, 075401.

116 L. P. A. Maia, J. S. Souza, A. F. Lima and M. V. Lalic, *Opt. Mater.*, 2024, **148**, 114927.

117 B. A. Rosales, M. A. White and J. Vela, *J. Am. Chem. Soc.*, 2018, **140**, 3736–3742.

118 Y. T. Huang, M. Schleuning, H. Hempel, Y. Zhang, M. Rusu, T. Unold, A. Musiienko, O. Karalis, N. Jung, S. J. Zelewski, A. J. Britton, N. Ngoh, W. Song, L. C. Hirst, H. Sirringhaus, S. D. Stranks, A. Rao, I. Levine and R. L. Z. Hoye, *Adv. Funct. Mater.*, 2024, 2310283.

119 B. V. Gabrel'yan, A. A. Lavrentiev, I. Y. Nikiforov and V. V. Sobolev, *J. Struct. Chem.*, 2008, **49**, 788–794.

120 A. M. Medina-Gonzalez, P. Yox, Y. Chen, M. A. S. Adamson, B. A. Rosales, M. Svay, E. A. Smith, R. D. Schaller, K. Wu, A. J. Rossini, K. Kovnir and J. Vela, *Chem. Mater.*, 2022, **34**, 7357–7368.

121 A. D. Jodlowski, D. Rodríguez-Padrón, R. Luque, G. de Miguel, A. D. Jodlowski, G. De Miguel and D. Rodríguez, *Adv. Energy Mater.*, 2018, **8**, 1703120.

122 D. Tiwari, O. S. Hutter and G. Longo, *J. Phys.: Energy*, 2021, **3**, 034010.

123 A. Swarnkar, W. J. Mir, R. Chakraborty, M. Jagadeeswararao, T. Sheikh and A. Nag, *Chem. Mater.*, 2019, **31**, 565–575.

124 Y. Nishigaki, T. Nagai, M. Nishiwaki, T. Aizawa, M. Kozawa, K. Hanzawa, Y. Kato, H. Sai, H. Hiramatsu, H. Hosono and H. Fujiwara, *Solar RRL*, 2020, **4**, 1900555.

125 S. Niu, H. Huyan, Y. Liu, M. Yeung, K. Ye, L. Blankemeier, T. Orvis, D. Sarkar, D. J. Singh, R. Kapadia, J. Ravichandran, S. Niu, H. Huyan, Y. Liu, K. Ye, T. Orvis, J. Ravichandran, M. Yeung, L. Blankemeier, D. Sarkar, R. Kapadia, M. Hsieh and D. J. Singh, *Adv. Mater.*, 2017, **29**, 1604733.

126 M. T. Hörantner and H. J. Snaith, *Energy Environ. Sci.*, 2017, **10**, 1983–1993.

127 J. A. Brehm, J. W. Bennett, M. R. Schoenberg, I. Grinberg and A. M. Rappe, *J. Chem. Phys.*, 2014, **140**, 224703.

128 K. C. Vincent, S. Agarwal, J. W. Turnley and R. Agrawal, *Adv. Energy Sustainability Res.*, 2023, **4**, 2300010.

129 T. Gupta, D. Ghoshal, A. Yoshimura, S. Basu, P. K. Chow, A. S. Lakhnot, J. Pandey, J. M. Warrender, H. Efstathiadis, A. Soni, E. Osei-Agyemang, G. Balasubramanian, S. Zhang,

This journal is © The Royal Society of Chemistry 2025

Energy Environ. Sci., 2025, **18**, 6899–6933 | **6927**

S. F. Shi, T. M. Lu, V. Meunier and N. Koratkar, *Adv. Funct. Mater.*, 2020, **30**, 2001387.

130 Y. Y. Sun, M. L. Agiorgousis, P. Zhang and S. Zhang, *Nano Lett.*, 2015, **15**, 581–585.

131 W. Meng, B. Saparov, F. Hong, J. Wang, D. B. Mitzi and Y. Yan, *Chem. Mater.*, 2016, **28**, 821–829.

132 J. A. Márquez, M. Rusu, H. Hempel, I. Y. Ahmet, M. Kölbach, I. Simsek, L. Choubrac, G. Gurieva, R. Gunder, S. Schorr and T. Unold, *J. Phys. Chem. Lett.*, 2021, **12**, 2148–2153.

133 X. Wei, H. Hui, C. Zhao, C. Deng, M. Han, Z. Yu, A. Sheng, P. Roy, A. Chen, J. Lin, D. F. Watson, Y. Y. Sun, T. Thomay, S. Yang, Q. Jia, S. Zhang and H. Zeng, *Nano Energy*, 2020, **68**, 104317.

134 Y. Han, J. Xu, Y. Liang, X. Chen, M. Jia, J. Zhang, L. Lian, Y. Liu, X. Li and Z. Shi, *Chem. Eng. J.*, 2023, **473**, 145351.

135 E. Osei-Agyemang, N. Koratkar and G. Balasubramanian, *J. Mater. Chem. C*, 2021, **9**, 3892–3900.

136 V. K. Ravi, S. H. Yu, P. K. Rajput, C. Nayak, D. Bhattacharyya, D. S. Chung and A. Nag, *Nanoscale*, 2021, **13**, 1616–1623.

137 U. V. Ghorpade, M. P. Suryawanshi, M. A. Green, T. Wu, X. Hao and K. M. Ryan, *Chem. Rev.*, 2023, **123**, 327–378.

138 F. Palazon, *Solar RRL*, 2022, **6**, 2100829.

139 I. Caño, J. W. Turnley, P. Benítez, C. López-Álvarez, J. M. Asensi, D. Payno, J. Puigdollers, M. Placidi, C. Cazorla, R. Agrawal and E. Saucedo, *J. Mater. Chem. C*, 2024, **12**, 3154–3163.

140 J. He, X. Hu, Z. Liu, W. Chen and G. Longo, *Adv. Funct. Mater.*, 2023, **33**, 2306075.

141 Y. C. Choi and K. W. Jung, *Nanomaterials*, 2020, **10**, 2284.

142 D. Savytskii, M. Sanders, R. Golovchak, B. Knorr, V. Dierolf and H. Jain, *J. Am. Ceram. Soc.*, 2014, **97**, 198–205.

143 Y. Wang, X. Dai, C. Dong, W. Guo, Z. Xu, Y. Chen, H. Xiang and R. Zhang, *Adv. Mater.*, 2022, **34**, 2106773.

144 K. T. Butler, S. McKechnie, P. Azarhoosh, M. Van Schilfgaarde, D. O. Scanlon and A. Walsh, *Appl. Phys. Lett.*, 2016, **108**, 112103.

145 H. Akkus, A. M. Mamedov, A. Kazempour and H. Akbarzadeh, *Cent. Eur. J. Phys.*, 2008, **6**, 64–75.

146 R. Nitsche and W. J. Merz, *J. Phys. Chem. Solids*, 1960, **13**, 154–155.

147 Solar - IEA, https://www.iea.org/energy-system/renewables/solar-pv, (accessed 22 May 2024).

148 B. V. Stefani, M. Kim, Y. Zhang, B. Hallam, M. A. Green, R. S. Bonilla, C. Fell, G. J. Wilson and M. Wright, *Joule*, 2023, **7**, 2684–2699.

149 H. Lin, M. Yang, X. Ru, G. Wang, S. Yin, F. Peng, C. Hong, M. Qu, J. Lu, L. Fang, C. Han, P. Procel, O. Isabella, P. Gao, Z. Li and X. Xu, *Nat. Energy*, 2023, **8**, 789–799.

150 LONGi sets new world record with 27.30% for heterojunction back contact cells and renames next generation silicon tera wafer to TaiRay Wafer, https://www.longi.com/eu/news/2730-hbc-world-record/, (accessed 15 March 2025).

151 G. M. Wilson, M. Al-Jassim, W. K. Metzger, S. W. Glunz, P. Verlinden, G. Xiong, L. M. Mansfield, B. J. Stanbery, K. Zhu, Y. Yan, J. J. Berry, A. J. Ptak, F. Dimroth, B. M. Kayes, A. C. Tamboli, R. Peibst, K. Catchpole, M. O. Reese, C. S. Klinga, P. Denholm, M. Morjaria, M. G. Deceglie, J. M. Freeman, M. A. Mikofski, D. C. Jordan, G. Tamizhmani and D. B. Sulas-Kern, *J. Phys. D: Appl. Phys.*, 2020, **53**, 493001.

152 P. G. V. Sampaio and M. O. A. González, *Renewable Sustainable Energy Rev.*, 2017, **74**, 590–601.

153 J. Day, S. Senthilarasu and T. K. Mallick, *Renew Energy*, 2019, **132**, 186–205.

154 M. C. Raval, S. M. Reddy and A. Hegedus, Industrial Silicon Solar Cells, in *Solar Cells*, ed. H. S. Nalwa, IntechOpen, London, 2019, ch. 1.

155 T. G. Allen, J. Bullock, X. Yang, A. Javey and S. De Wolf, *Nat. Energy*, 2019, **4**, 914–928.

156 D. K. Ghosh, S. Bose, G. Das, S. Acharyya, A. Nandi, S. Mukhopadhyay and A. Sengupta, *Surf. Interfaces*, 2022, **30**, 101917.

157 E. Aydin, T. G. Allen, M. De Bastiani, A. Razzaq, L. Xu, E. Ugur, J. Liu and S. De Wolf, *Science*, 1979, **2024**(383), 1–13.

158 M. I. Elsmani, N. Fatima, M. P. A. Jallorina, S. Sepeai, M. S. Suait, N. A. Ludin, M. A. M. Teridi, K. Sopian and M. A. Ibrahim, *Nanomaterials*, 2021, **11**, 3186.

159 M. Wright, B. Vicari Stefani, T. W. Jones, B. Hallam, A. Soeriyadi, L. Wang, P. Altermatt, H. J. Snaith, G. J. Wilson and R. S. Bonilla, *Energy Environ. Sci.*, 2023, **16**, 4164–4190.

160 P. Zhang, C. Li, M. He, Z. Liu and X. Hao, *Small Methods*, 2024, **8**, 2300432.

161 M. De Bastiani, A. S. Subbiah, E. Aydin, F. H. Isikgor, T. G. Allen and S. De Wolf, *Mater. Horiz.*, 2020, **7**, 2791–2809.

162 S. De Wolf and M. Kondo, *J. Appl. Phys.*, 2009, **105**, 103707.

163 J. H. Park, S. G. Ji, Y. S. Yoon, M. A. Park, S. H. Lee, K. H. Kim and J. Y. Kim, *Adv. Mater. Technol.*, 2023, **8**, 2201006.

164 F. Fu, J. Li, T. C. J. Yang, H. Liang, A. Faes, Q. Jeangros, C. Ballif and Y. Hou, *Adv. Mater.*, 2022, **34**, 2106540.

165 G. Nogay, F. Sahli, J. Werner, R. Monnard, M. Boccard, M. Despeisse, F. J. Haug, Q. Jeangros, A. Ingenito and C. Ballif, *ACS Energy Lett.*, 2019, **4**, 844–845.

166 S. Yu, M. Rabelo and J. Yi, *Trans. Electr. Electron. Mater.*, 2022, **23**, 327–336.

167 Y. Du, B. Xu, G. Wang, Y. Miao, B. Li, Z. Kong, Y. Dong, W. Wang and H. H. Radamson, *Nanomaterials*, 2022, **12**, 741.

168 Philipps: McEvoy's Handbook of Photovoltaics - Google Scholar, https://scholar.google.com/scholar_lookup?hl=en&publication_year=2018&pages=439-472&author=S.+P.+Philipps&author=F.+Dimroth&author=A.+W.+Bett&title=McEvoy%27s+Handbook+of+Photovoltaics, (accessed 25 May 2024).

169 X. Li, Q. Xu, L. Yan, C. Ren, B. Shi, P. Wang, S. Mazumdar, G. Hou, Y. Zhao and X. Zhang, *Nanophotonics*, 2021, **10**, 2001–2022.

6928 | *Energy Environ. Sci.*, 2025, **18**, 6899–6933

This journal is © The Royal Society of Chemistry 2025

170 M. Akiyama, Y. Kawarada and K. Kaminishi, *J. Cryst. Growth*, 1984, **68**, 21–26.

171 K. Derendorf, S. Essig, E. Oliva, V. Klinger, T. Roesener, S. P. Philipps, J. Benick, M. Hermle, M. Schachtner, G. Siefer, W. Jäger and F. Dimroth, *IEEE J. Photovoltaics*, 2013, **3**, 1423–1428.

172 R. Cariou, J. Benick and P. Beutel, *IEEE J. Photovoltaics*, 2017, **7**, 367–373.

173 Y. Zeng, Z. Ding, Z. Liu, Q. Zhou, X. Liu, Z. Liu, S. M. Iftiquar, J. Jung and J. Yi, *J. Phys. D: Appl. Phys.*, 2018, **51**, 133002.

174 S. Essig, C. Allebé, T. Remo, J. F. Geisz, M. A. Steiner, K. Horowitz, L. Barraud, J. S. Ward, M. Schnabel, A. Descoeudres, D. L. Young, M. Woodhouse, M. Despeisse, C. Ballif and A. Tamboli, *Nat. Energy*, 2017, **2**, 1–9.

175 P. Schygulla, R. Müller, D. Lackner, O. Höhn, H. Hauser, B. Bläsi, F. Predan, J. Benick, M. Hermle, S. W. Glunz and F. Dimroth, *Prog. Photovoltaics Res. Appl.*, 2022, **30**, 869–879.

176 M. N. Sharif, J. Yang, X. Zhang, Y. Tang and K. F. Wang, *Solar RRL*, 2023, **7**, 2300156.

177 C. Gao, D. Du, D. Ding, F. Qiao and W. Shen, *J. Mater. Chem. A*, 2022, **10**, 10811–10828.

178 IEC 61215-1:2016 | IEC Webstore | rural electrification, solar power, solar panel, photovoltaic, PV, smart city, LVDC, https://webstore.iec.ch/publication/24312, (accessed 25 May 2024).

179 New method allows perovskite solar cells to meet IEC testing requirements, https://www.iec.ch/blog/new-method-allows-perovskite-solar-cells-meet-iec-testing-requirements, (accessed 25 May 2024).

180 A. K. Jena, A. Kulkarni and T. Miyasaka, *Chem. Rev.*, 2019, **119**, 3036–3103.

181 R. Wang, T. Huang, J. Xue, J. Tong, K. Zhu and Y. Yang, *Nat. Photonics*, 2021, **15**, 411–425.

182 J. Wei, Q. Wang, J. Huo, F. Gao, Z. Gan, Q. Zhao and H. Li, *Adv. Energy Mater.*, 2021, **11**, 2002326.

183 Z. Wang, Z. Zhang, L. Xie, S. Wang, C. Yang, C. Fang and F. Hao, *Adv. Opt. Mater.*, 2022, **10**, 2101822.

184 P. Roy, N. Kumar Sinha, S. Tiwari and A. Khare, *Sol. Energy*, 2020, **198**, 665–688.

185 C. Ran, Y. Wang, W. Gao, Y. Xia, Y. Chen and W. Huang, *Solar RRL*, 2021, **5**, 2100665.

186 M. Ren, X. Qian, Y. Chen, T. Wang and Y. Zhao, *J. Hazard. Mater.*, 2022, **426**, 127848.

187 J. Qian, *Sustainable Energy Fuels*, 2019, **3**, 1439–1447.

188 R. Witteck, J. F. Geisz, E. L. Warren and W. E. McMahon, *Solar RRL*, 2024, **8**, 2300782.

189 G. Ji, M.-A. Park, H. Jang, J. Y. Kim, I. J. Park, J. H. Park, S. G. Ji and J. H. Jang, *Joule*, 2019, **3**, 807–818.

190 Y. Shi, J. J. Berry and F. Zhang, *ACS Energy Lett.*, 2024, **9**, 1305–1330.

191 M. Abbas, X. Xu, M. Rauf and A. K. K. Kyaw, *Photonics*, 2024, **11**, 87.

192 P. Chen, Y. Bai and L. Wang, *Small Struct.*, 2021, **2**, 2000050.

193 S. Mahesh, J. M. Ball, R. D. J. Oliver, D. P. McMeekin, P. K. Nayak, M. B. Johnston and H. J. Snaith, *Energy Environ. Sci.*, 2020, **13**, 258–267.

194 C. Zhang, Y. N. Lu, W. Q. Wu and L. Wang, *Nano Energy*, 2021, **81**, 105634.

195 M. Jošt, E. Köhnen, A. B. Morales-Vilches, B. Lipovšek, K. Jäger, B. Macco, A. Al-Ashouri, J. Krč, L. Korte, B. Rech, R. Schlatmann, M. Topič, B. Stannowski and S. Albrecht, *Energy Environ. Sci.*, 2018, **11**, 3511–3523.

196 M. De Bastiani, R. Jalmood, J. Liu, C. Ossig, A. Vlk, K. Vegso, M. Babics, F. H. Isikgor, A. S. Selvin, R. Azmi, E. Ugur, S. Banerjee, A. J. Mirabelli, E. Aydin, T. G. Allen, A. Ur Rehman, E. Van Kerschaver, P. Siffalovic, M. E. Stuckelberger, M. Ledinsky and S. De Wolf, *Adv. Funct. Mater.*, 2023, **33**, 2205557.

197 S. Lu, C. Chen and J. Tang, *Front. Optoelectron.*, 2020, **13**, 246–255.

198 (PDF) Toward A 25%-efficient polycrystalline thin-film tandem solar cell: Practical issues, https://www.researchgate.net/publication/4078364_Toward_A_25-efficient_polycrystalline_thin-film_tandem_solar_cell_Practical_issues, (accessed 23 May 2024).

199 A. R. Jeong, S. Bin Choi, W. M. Kim, J. K. Park, J. Choi, I. Kim and J. H. Jeong, *Sci. Rep.*, 2017, **7**, 1–10.

200 K. Kim, J. Gwak, S. K. Ahn, Y. J. Eo, J. H. Park, J. S. Cho, M. G. Kang, H. E. Song and J. H. Yun, *Sol. Energy*, 2017, **145**, 52–58.

201 T. Hölscher, M. Placidi, I. Becerril-Romero, R. Fonoll-Rubio, V. Izquierdo-Roca, A. Thomere, E. Bailo, T. Schneider, H. Kempa, R. Scheer and A. Pérez-Rodríguez, *Sol. Energy Mater. Sol. Cells*, 2023, **251**, 112169.

202 Y. Li, C. Cui, H. Wei, Z. Shao, Z. Wu, S. Zhang, X. Wang, S. Pang and G. Cui, *Adv. Mater.*, 2024, 2400138.

203 M. Valentini, C. Malerba, L. Serenelli, M. Izzi, E. Salza, M. Tucci and A. Mittiga, *Sol. Energy*, 2019, **190**, 414–419.

204 F. Martinho, A. Hajijafarassar, S. Lopez-Marino, M. Espíndola-Rodríguez, S. Engberg, M. Gansukh, F. Stulen, S. Grini, S. Canulescu, E. Stamate, A. Crovetto, L. Vines, J. Schou and O. Hansen, *ACS Appl. Energy Mater.*, 2020, **3**, 4600–4609.

205 A. Hajijafarassar, F. Martinho, F. Stulen, S. Grini, S. López-Mariño, M. Espíndola-Rodríguez, M. Döbeli, S. Canulescu, E. Stamate, M. Gansukh, S. Engberg, A. Crovetto, L. Vines, J. Schou and O. Hansen, *Sol. Energy Mater. Sol. Cells*, 2020, **207**, 110334.

206 E. R. Weber, Impurity Precipitation, Dissolution, Gettering and Passivation in PV Silicon: Final Technical Report, 30 January 1998–29 August 2001.

207 M. Gansukh, A. Assar, F. Martinho, S. L. Mariño, M. Espíndola-Rodríguez, S. Engberg, E. Stamate, J. Schou, O. Hansen and S. Canulescu, *Appl. Phys. A:Mater. Sci. Process.*, 2022, **128**, 1–6.

208 A. Assar, F. Martinho, J. Larsen, N. Saini, D. Shearer, M. V. Moro, F. Stulen, S. Grini, S. Engberg, E. Stamate, J. Schou, L. Vines, S. Canulescu, C. Platzer-Björkman and O. Hansen, *ACS Appl. Mater. Interfaces*, 2022, **14**, 14342–14358.

This journal is © The Royal Society of Chemistry 2025

Energy Environ. Sci., 2025, **18**, 6899–6933 | **6929**

209 C. Qian, K. Sun, J. Cong, H. Cai, J. Huang, C. Li, R. Cao, Z. Liu, M. Green, B. Hoex, T. Chen and X. Hao, *Adv. Mater.*, 2023, **35**, 2303936.

210 Z. Xia, J. Zhong, M. Leng, L. Hu, D. J. Xue, B. Yang, Y. Zhou, X. Liu, S. Qin, Y. B. Cheng and J. Tang, *Chem. Mater.*, 2015, **27**, 8048–8057.

211 C. Gao, M. Xu, B. K. Ng, L. Kang, L. Jiang, Y. Lai and F. Liu, *Mater. Lett.*, 2017, **195**, 186–189.

212 M. Okil, A. Shaker, I. S. Ahmed, T. M. Abdolkader and M. S. Salem, *Sol. Energy Mater. Sol. Cells*, 2023, **253**, 112210.

213 F. Martinho, *Energy Environ. Sci.*, 2021, **14**, 3840–3871.

214 L. P. Mwakyusa, X. Jin, E. Müller, R. Schneider, D. Gerthsen, M. Rinke, U. W. Paetzold, B. S. Richards and M. Hetterich, *J. Appl. Phys.*, 2021, **129**, 153104.

215 P. Punathil, E. Artegiani, S. Zanetti, L. Lozzi, V. Kumar and A. Romeo, *Sol. Energy*, 2022, **236**, 599–607.

216 M. Kumar, A. Dubey, N. Adhikari, S. Venkatesan and Q. Qiao, *Energy Environ. Sci.*, 2015, **8**, 3134–3159.

217 Q. Cao, O. Gunawan, M. Copel, K. B. Reuter, S. J. Chey, V. R. Deline and D. B. Mitzi, *Adv. Energy Mater.*, 2011, **1**, 845–853.

218 U. Chalapathi, B. Poornaprakash and S. H. Park, *Superlattices Microstruct.*, 2020, **141**, 106500.

219 D. Alagarasan, S. S. Hegde, S. Varadharajaperumal, K. D. Arun Kumar, R. Naik, S. P. Panjalingam, E. E. S. Massoud and R. Ganesan, *J. Mater. Sci.: Mater. Electron.*, 2022, **33**, 4794–4805.

220 M. D. K. Jones, J. A. Dawson, S. Campbell, V. Barrioz, L. D. Whalley and Y. Qu, *Front. Chem.*, 2022, **10**, 920676.

221 M. He, C. Yan, J. Li, M. P. Suryawanshi, J. Kim, M. A. Green and X. Hao, *Adv. Sci.*, 2021, **8**, 2004313.

222 S. Akhil and R. G. Balakrishna, *J. Mater. Chem. A*, 2022, **10**, 8615–8625.

223 A. J. Bett, K. M. Winkler, M. Bivour, L. Cojocaru, Ö. Kabakli, P. S. C. Schulze, G. Siefer, L. Tutsch, M. Hermle, S. W. Glunz and J. C. Goldschmidt, *ACS Appl. Mater. Interfaces*, 2019, **11**, 45796–45804.

224 X. Zhang, D. Han, S. Chen, C. Duan and J. Chu, *J. Energy Chem.*, 2018, **27**, 1140–1150.

225 D. Colombara, H. Elanzeery, N. Nicoara, D. Sharma, M. Claro, T. Schwarz, A. Koprek, M. H. Wolter, M. Melchiorre, M. Sood, N. Valle, O. Bondarchuk, F. Babbe, C. Spindler, O. Cojocaru-Miredin, D. Raabe, P. J. Dale, S. Sadewasser and S. Siebentritt, *Nat. Commun.*, 2020, **11**, 1–14.

226 B. Shin, N. A. Bojarczuk and S. Guha, *Appl. Phys. Lett.*, 2013, **102**, 091907.

227 S. Prathapani and Y. Zhan, *Energy Technol.*, 2021, **9**, 2100193.

228 S. P. Bremner, M. Y. Levy and C. B. Honsberg, *Prog. Photovoltaics Res. Appl.*, 2008, **16**, 225–233.

229 B. Mahmoudi, F. Caddeo, T. Lindenberg, T. Schneider, T. Hölscher, R. Scheer and A. W. Maijenburg, *Electrochim. Acta*, 2021, **367**, 137183.

230 M. H. Miah, M. U. Khandaker, M. B. Rahman, M. Nur-E-Alam and M. A. Islam, *RSC Adv.*, 2024, **14**, 15876–15906.

231 S. Tao, I. Schmidt, G. Brocks, J. Jiang, I. Tranca, K. Meerholz and S. Olthof, *Nat. Commun.*, 2019, **10**, 1–10.

232 I. Sharma, P. S. Pawar, R. Kumar Yadav, R. Nandi and J. Heo, *Sol. Energy*, 2022, **246**, 152–180.

233 B. Vermang, G. Brammertz, M. Meuris, T. Schnabel, E. Ahlswede, L. Choubrac, S. Harel, C. Cardinaud, L. Arzel, N. Barreau, J. Van Deelen, P. J. Bolt, P. Bras, Y. Ren, E. Jaremalm, S. Khelifi, S. Yang, J. Lauwaert, M. Batuk, J. Hadermann, X. Kozina, E. Handick, C. Hartmann, D. Gerlach, A. Matsuda, S. Ueda, T. Chikyow, R. Félix, Y. Zhang, R. G. Wilks and M. Bär, *Sustainable Energy Fuels*, 2019, **3**, 2246–2259.

234 M. B. Salim, R. Nekovei and R. Jeyakumar, *Sol. Energy*, 2020, **198**, 160–166.

235 D. B. Mitzi and Y. Kim, *Faraday Discuss.*, 2022, **239**, 9–37.

236 F. Werlinger, C. Segura, J. Martínez, I. Osorio-Roman, D. Jara, S. J. Yoon and A. F. Gualdrón-Reyes, *Energies*, 2023, **16**, 5868.

237 D. Shin, B. Saparov and D. B. Mitzi, *Adv. Energy Mater.*, 2017, **7**, 1602366.

238 A. Crovetto, S. Kim, M. Fischer, N. Stenger, A. Walsh, I. Chorkendorff and P. C. K. Vesborg, *Energy Environ. Sci.*, 2020, **13**, 3489–3503.

239 J. A. Van Delft, D. Garcia-Alonso and W. M. M. Kessels, *Semicond. Sci. Technol.*, 2012, **27**, 074002.

240 M. A. Hossain, K. T. Khoo, X. Cui, G. K. Poduval, T. Zhang, X. Li, W. M. Li and B. Hoex, *Nano Mater. Sci.*, 2020, **2**, 204–226.

241 S. M. George, *Chem. Rev.*, 2010, **110**, 111–131.

242 J. A. Oke, O. O. Olotu and T. C. Jen, *J. Mater. Res. Technol.*, 2022, **20**, 991–1019.

243 M. A. Farhana, A. Manjceevan and J. Bandara, *J. Sci.:Adv. Mater. Devices*, 2023, **8**, 100533.

244 U. Chalapathi, S. Sangaraju, Y. B. K. Kumar, R. Cheruku, P. Kondaiah, M. Lavanya, V. Gonuguntla, S. Alhammadi, M. D. Albaqami, M. Sheikh and S. H. Park, *Opt. Mater.*, 2024, **152**, 115492.

245 M. Nakamura, H. Nakamura, Y. Matsushita, K. Shimamura and N. Ohashi, *J. Cryst. Growth*, 2020, **547**, 125813.

246 N. Spalatu, R. Krautmann, A. Katerski, E. Karber, R. Josepson, J. Hiie, I. O. Acik and M. Krunks, *Sol. Energy Mater. Sol. Cells*, 2021, **225**, 111045.

247 R. Krautmann, N. Spalatu, R. Josepson, R. Nedzinskas, R. Kondrotas, R. Gržibovskis, A. Vembris, M. Krunks and I. Oja Acik, *Sol. Energy Mater. Sol. Cells*, 2023, **251**, 112139.

248 R. W. Miles, O. E. Ogah, G. Zoppi and I. Forbes, *Thin Solid Films*, 2009, **517**, 4702–4705.

249 S. Das, R. N. Bhattacharya and K. C. Mandal, *Sol. Energy Mater. Sol. Cells*, 2016, **144**, 347–351.

250 K. Li, R. Tang, C. Zhu and T. Chen, *Adv. Sci.*, 2024, **11**, 2304963.

251 M. A. Scarpulla, B. McCandless, A. B. Phillips, Y. Yan, M. J. Heben, C. Wolden, G. Xiong, W. K. Metzger, D. Mao, D. Krasikov, I. Sankin, S. Grover, A. Munshi, W. Sampath, J. R. Sites, A. Bothwell, D. Albin, M. O. Reese, A. Romeo,

6930 | *Energy Environ. Sci.*, 2025, **18**, 6899–6933

This journal is © The Royal Society of Chemistry 2025

M. Nardone, R. Klie, J. M. Walls, T. Fiducia, A. Abbas and S. M. Hayes, *Sol. Energy Mater. Sol. Cells*, 2023, **255**, 112289.

252 I. Sharma, P. S. Pawar, R. K. Yadav, Y. T. Kim, N. Bisht, P. R. Patil and J. Heo, *Chem. Eng. J.*, 2024, **491**, 152086.

253 R. Yang, J. Nelson, C. Fai, H. A. Yetkin, C. Werner, M. Tervil, A. D. Jess, P. J. Dale and C. J. Hages, *Chem. Mater.*, 2023, **35**, 4743–4750.

254 J. W. Turnley and R. Agrawal, *Chem. Commun.*, 2024, **60**, 5245–5269.

255 V. V. Akshay, S. Benny and S. V. Bhat, *Sol. Energy*, 2022, **241**, 728–737.

256 W. Li, J. M. R. Tan, S. W. Leow, S. Lie, S. Magdassi and L. H. Wong, *Energy Technol.*, 2018, **6**, 46–59.

257 D. B. Mitzi, *Adv. Mater.*, 2009, **21**, 3141–3158.

258 D. Tiwari, T. Koehler, X. Lin, R. Harniman, I. Griffiths, L. Wang, D. Cherns, R. Klenk and D. J. Fermin, *Chem. Mater.*, 2016, **28**, 4991–4997.

259 M. Zhang, D. Yoo, Y. Kang, W. Park, J. In Lee, Y. Kim, Y. H. Hwang and D. Lee, *Appl. Surf. Sci.*, 2023, **607**, 155022.

260 J. Fu, D. Kou, W. Zhou, Z. Zhou, S. Yuan, Y. Qi and S. Wu, *J. Mater. Chem. A*, 2020, **8**, 22292–22301.

261 S. Benny, A. V. Vidyanagar and S. V. Bhat, *Energy and Fuels*, 2024, **38**, 61–72.

262 K. V. Gunavathy, K. Tamilarasan, C. Rangasami and A. M. S. Arulanantham, *Int. J. Energy Res.*, 2019, **43**, 7716–7754.

263 P. S. Patil, *Mater. Chem. Phys.*, 1999, **59**, 185–198.

264 A. Giri, G. Park and U. Jeong, *Chem. Rev.*, 2023, **123**, 3329–3442.

265 J. Chen, G. Li, Z. Xu, C. Xu, F. Naveed, B. Liu, Y. Zhang, R. Zhou, C. Chen, M. Wang, J. Xu, L. Li, J. Chen, G. Li, Z. Xu, C. Xu, B. Liu, Y. Zhang, J. Xu, F. Naveed, C. Chen, M. Wang, R. Zhou and L. Li, *Adv. Funct. Mater.*, 2024, **34**, 2313676.

266 K. J. Huang, L. Li and E. A. Olivetti, *Joule*, 2018, **2**, 1642–1647.

267 P. Bü, F. Scheler, C. Pointer, D. Döhler, T. Yokosawa, E. Spiecker, P. P. Boix, E. R. Young, I. Mínguez-Bacho and J. Bachmann, *ACS Appl. Mater. Interfaces*, 2021, **13**, 11861–11868.

268 A. Wang, M. He, M. A. Green, K. Sun and X. Hao, *Adv. Energy Mater.*, 2023, **13**, 2203046.

269 H. Li, J. Chen, Y. Zhang, W. Wang and H. Gu, *ACS Appl. Energy Mater.*, 2020, **3**, 9459–9467.

270 X. Liu, Y. Feng, H. Cui, F. Liu, X. Hao, G. Conibeer, D. B. Mitzi and M. Green, *Prog. Photovoltaics Res. Appl.*, 2016, **24**, 879–898.

271 M. He, K. Sun, M. P. Suryawanshi, J. Li and X. Hao, *J. Energy Chem.*, 2021, **60**, 1–8.

272 Nisika, K. Kaur and M. Kumar, *J. Mater. Chem. A*, 2020, **8**, 21547–21584.

273 A. Wang, M. He, M. A. Green, K. Sun and X. Hao, *Adv. Energy Mater.*, 2023, **13**, 2203046.

274 M. Kangsabanik and R. N. Gayen, *Solar RRL*, 2023, **7**, 2300670.

275 L. Wang, J. Ban, L. Han, Z. Zhou, W.-H. Zhou, D. Kou, Y.-N. Meng, Y. Qi, S. Yuan and S.-X. Wu, *J. Mater. Chem. A*, 2024, **12**, 25643–25677.

276 S. Barthwal, S. Singh, A. K. Chauhan, N. S. Prabhu, A. G. Prabhudessai and K. Ramesh, *Mater. Adv.*, 2023, **4**, 5998–6030.

277 K. Jagadish, G. K. Rahane, B. S. Kumar, D. R. Borkar, K. Chordiya, S. R. Kavanagh, A. Roy, T. Debnath, S. Kolekar, M. U. Kahaly, S. S. Mali, S. Pal, N. Gasparini, D. P. Dubal and S. R. Rondiya, *Small*, 2024, **20**, 2402048.

278 A. Maiti, S. Chatterjee and A. J. Pal, *ACS Appl. Energy Mater.*, 2020, **3**, 810–821.

279 A. Debono, F. Martinho, J. Schou and S. Canulescu, *ACS Omega*, 2024, **9**, 50439–50445.

280 M. A. Curado, J. P. Teixeira, M. Monteiro, E. F. M. Ribeiro, R. C. Vilão, H. V. Alberto, J. M. V. Cunha, T. S. Lopes, K. Oliveira, O. Donzel-Gargand, A. Hultqvist, S. Calderon, M. A. Barreiros, W. Chiappim, J. P. Leitão, A. G. Silva, T. Prokscha, C. Vinhais, P. A. Fernandes and P. M. P. Salomé, *Appl Mater. Today*, 2020, **21**, 100867.

281 V. C. Karade, M. P. Suryawanshi, J. S. Jang, K. S. Gour, S. Jang, J. Park, J. H. Kim and S. W. Shin, *J. Mater. Chem. A*, 2022, **10**, 8466–8478.

282 J. de Wild, R. Scaffidi, G. Brammertz, G. Birant and B. Vermang, *Adv. Energy Sustainability Res.*, 2023, **4**, 2200132.

283 R. Scaffidi, D. G. Buldu, G. Brammertz, J. de Wild, T. Kohl, G. Birant, M. Meuris, J. Poortmans, D. Flandre and B. Vermang, *Phys. Status Solidi A*, 2021, **218**, 2100073.

284 M. E. Erkan, V. Chawla and M. A. Scarpulla, *J. Appl. Phys.*, 2016, **119**, 54.

285 F. Werner, B. Veith-Wolf, M. Melchiorre, F. Babbe, J. Schmidt and S. Siebentritt, *Sci. Rep.*, 2020, **10**, 1–14.

286 X. Cui, K. Sun, J. Huang, J. S. Yun, C. Y. Lee, C. Yan, H. Sun, Y. Zhang, C. Xue, K. Eder, L. Yang, J. M. Cairney, J. Seidel, N. J. Ekins-Daukes, M. Green, B. Hoex and X. Hao, *Energy Environ. Sci.*, 2019, **12**, 2751–2764.

287 K. Li, C. Chen, S. Lu, C. Wang, S. Wang, Y. Lu, J. Tang, K. Li, C. Chen, S. Lu, C. Wang, S. Wang, Y. Lu and J. Tang, *Adv. Mater.*, 2019, **31**, 1903914.

288 K. Sun, J. Huang, C. Yan, A. Pu, F. Liu, H. Sun, X. Liu, Z. Fang, J. A. Stride, M. Green and X. Hao, *Chem. Mater.*, 2018, **30**, 4008–4016.

289 N. Ahmad, Y. Zhao, F. Ye, J. Zhao, S. Chen, Z. Zheng, P. Fan, C. Yan, Y. Li, Z. Su, X. Zhang and G. Liang, *Adv. Sci.*, 2023, **10**, 2302869.

290 C. Yan, J. Huang, K. Sun, S. Johnston, Y. Zhang, H. Sun, A. Pu, M. He, F. Liu, K. Eder, L. Yang, J. M. Cairney, N. J. Ekins-Daukes, Z. Hameiri, J. A. Stride, S. Chen, M. A. Green and X. Hao, *Nat. Energy*, 2018, **3**, 764–772.

291 T. K. Todorov, J. Tang, S. Bag, O. Gunawan, T. Gokmen, Y. Zhu and D. B. Mitzi, *Adv. Energy Mater.*, 2013, **3**, 34–38.

292 Y. Gong, Q. Zhu, B. Li, S. Wang, B. Duan, L. Lou, C. Xiang, E. Jedlicka, R. Giridharagopal, Y. Zhou, Q. Dai, W. Yan, S. Chen, Q. Meng and H. Xin, *Nat. Energy*, 2022, **7**, 966–977.

This journal is © The Royal Society of Chemistry 2025

Energy Environ. Sci., 2025, **18**, 6899–6933 | **6931**

293 Y. S. Lee, T. Gershon, T. K. Todorov, W. Wang, M. T. Winkler, M. Hopstaken, O. Gunawan, J. Kim, Y. S. Lee, T. Gershon, T. K. Todorov, W. Wang, M. T. Winkler, M. Hopstaken, O. Gunawan and J. Kim, *Adv. Energy Mater.*, 2016, **6**, 1600198.

294 J. Han, S. Wang, J. Yang, S. Guo, Q. Cao, H. Tang, X. Pu, B. Gao and X. Li, *ACS Appl. Mater. Interfaces*, 2020, **12**, 4970–4979.

295 Y. C. Choi, D. U. Lee, J. H. Noh, E. K. Kim and S. Il Seok, *Adv. Funct. Mater.*, 2014, **24**, 3587–3592.

296 H. Liu, V. Avrutin, N. Izyumskaya, Ü. Özgr and H. Morkoç, *Superlattices Microstruct.*, 2010, **48**, 458–484.

297 D. A. Jacobs, M. Langenhorst, F. Sahli, B. S. Richards, T. P. White, C. Ballif, K. R. Catchpole and U. W. Paetzold, *J. Phys. Chem. Lett.*, 2019, **10**, 3159–3170.

298 M. Schultes, T. Helder, E. Ahlswede, M. F. Aygüler, P. Jackson, S. Paetel, J. A. Schwenzer, I. M. Hossain, U. W. Paetzold and M. Powalla, *ACS Appl. Energy Mater.*, 2019, **2**, 7823–7831.

299 S. A. U. Hasan and J. Yi, *Energy Technol.*, 2024, **12**, 2300832.

300 J. Kim, J. S. Jang, S. W. Shin, H. Park, W. L. Jeong, S. H. Mun, J. H. Min, J. Ma, J. Heo, D. S. Lee, J. J. Woo, J. H. Kim and H. J. Kim, *Small*, 2023, **19**, 2207966.

301 V. H. Nguyen, D. T. Papanastasiou, J. Resende, L. Bardet, T. Sannicolo, C. Jiménez, D. Muñoz-Rojas, N. D. Nguyen, D. Bellet, V. H. Nguyen, D. T. Papanastasiou, L. Bardet, C. Jiménez, D. Muñoz-Rojas, D. Bellet, J. Resende, A. Colab, M. Parque and N. D. Nguyen, *Small*, 2022, **18**, 2106006.

302 D. A. Ilatovskii, E. P. Gilshtein, O. E. Glukhova and A. G. Nasibulin, *Adv. Sci.*, 2022, **9**, 2201673.

303 M.-R. Azani, A. Hassanpour, T. Torres, M.-R. Azani, A. Hassanpour and T. Torres, *Adv. Energy Mater.*, 2020, **10**, 2002536.

304 E. Aydin, C. Altinkaya, Y. Smirnov, M. A. Yaqin, K. P. S. Zanoni, A. Paliwal, Y. Firdaus, T. G. Allen, T. D. Anthopoulos, H. J. Bolink, M. Morales-Masis and S. De Wolf, *Matter*, 2021, **4**, 3549–3584.

305 J. S. Jang, V. C. Karade, M. P. Suryawanshi, D. M. Lee, J. Kim, S. Jang, M. C. Baek, M. He, J. H. Kim and S. W. Shin, *Solar RRL*, 2023, **7**, 2300199.

306 K. Ellmer, *Nat. Photonics*, 2012, **6**, 809–817.

307 W. Greenbank, L. Hirsch, G. Wantz and S. Chambon, *Appl. Phys. Lett.*, 2015, **107**, 263301.

308 A. I. Hofmann, W. T. T. Smaal, M. Mumtaz, D. Katsigiannopoulos, C. Brochon, F. Schütze, O. R. Hild, E. Cloutet and G. Hadziioannou, *Angew. Chem.*, 2015, **127**, 8626–8630.

309 T. Cheng, Y. Zhang, W. Y. Lai and W. Huang, *Adv. Mater.*, 2015, **27**, 3349–3376.

310 J. W. Seo, M. Joo, J. Ahn, T. I. Lee, T. S. Kim, S. G. Im and J. Y. Lee, *Nanoscale*, 2017, **9**, 3399–3407.

311 D. S. Hecht, L. Hu and G. Irvin, *Adv. Mater.*, 2011, **23**, 1482–1513.

312 Y. Wang, T. Brezesinski, M. Antonietti and B. Smarsly, *ACS Nano*, 2009, **3**, 1373–1378.

313 J. Du, S. Pei, L. Ma and H. M. Cheng, *Adv. Mater.*, 2014, **26**, 1958–1991.

314 X. M. Feng, R. M. Li, Y. W. Ma, R. F. Chen, N. E. Shi, Q. L. Fan and W. Huang, *Adv. Funct. Mater.*, 2011, **21**, 2989–2996.

315 D. C. Lim, J. H. Jeong, K. Hong, S. Nho, J. Y. Lee, Q. V. Hoang, S. K. Lee, K. Pyo, D. Lee and S. Cho, *Prog. Photovoltaics Res. Appl.*, 2018, **26**, 188–195.

316 D. K. Choi, D. H. Kim, C. M. Lee, H. Hafeez, S. Sarker, J. S. Yang, H. J. Chae, G. W. Jeong, D. H. Choi, T. W. Kim, S. Yoo, J. Song, B. S. Ma, T. S. Kim, C. H. Kim, H. J. Lee, J. W. Lee, D. Kim, T. S. Bae, S. M. Yu, Y. C. Kang, J. Park, K. H. Kim, M. Sujak, M. Song, C. S. Kim and S. Y. Ryu, *Nat. Commun.*, 2021, **12**, 1–11.

317 J. Yun, *Adv. Funct. Mater.*, 2017, **27**, 1606641.

318 N. N. Rosli, M. A. Ibrahim, N. Ahmad Ludin, M. A. Mat Teridi and K. Sopian, *Renewable Sustainable Energy Rev.*, 2019, **99**, 83–99.

319 F. Qiao, H. Chu, Y. Xie and Z. Weng, *Int. J. Energy Res.*, 2022, **46**, 4071–4087.

320 G. Xu and Y. Li, *Nano Select*, 2020, **1**, 169–182.

321 A. I. Hofmann, E. Cloutet and G. Hadziioannou, *Adv. Electron. Mater.*, 2018, **4**, 1700412.

322 C. Cui, Q. Ding, S. Yu, C. Yu, D. Jiang, C. Hu, Z. Gu and J. Zhu, *Prog. Mater. Sci.*, 2023, **136**, 101112.

323 A. Anand, M. Moidul Islam, R. Meitzner, U. S. Schubert, H. Hoppe, A. Anand, M. M. Islam, R. Meitzner, U. S. Schubert and H. Hoppe, *Adv. Energy Mater.*, 2021, **11**, 2100875.

324 R. K. Kothandaraman, Y. Jiang, T. Feurer, A. N. Tiwari, F. Fu, R. K. Kothandaraman, Y. Jiang, T. Feurer, A. N. Tiwari and F. Fu, *Small Methods*, 2020, **4**, 2000395.

325 E. Muchuweni, B. S. Martincigh and V. O. Nyamori, *Adv. Energy Sustainability Res.*, 2021, **2**, 2100050.

326 Z. Ying, X. Yang, X. Wang and J. Ye, *Adv. Mater.*, 2024, **36**, 2311501.

327 K. Mun Yeom, S. Un Kim, M. Young Woo, J. Hong Noh, S. Hyuk Im, K. M. Yeom, M. Y. Woo, J. H. Noh, S. U. Kim and S. H. Im, *Adv. Mater.*, 2020, **32**, 2002228.

328 C. Yan, J. Huang, D. Li and G. Li, *Mater. Chem. Front.*, 2021, **5**, 4538–4564.

329 M. T. Winkler, W. Wang, O. Gunawan, H. J. Hovel, T. K. Todorov and D. B. Mitzi, *Energy Environ. Sci.*, 2014, **7**, 1029–1036.

330 M. I. Hossain, W. Qarony, V. Jovanov, Y. H. Tsang and D. Knipp, *J. Mater. Chem. A*, 2018, **6**, 3625–3633.

331 J. P. Mailoa, C. D. Bailie, E. C. Johlin, E. T. Hoke, A. J. Akey, W. H. Nguyen, M. D. McGehee and T. Buonassisi, *Appl. Phys. Lett.*, 2015, **106**, 121105.

332 F. Sahli, B. A. Kamino, J. Werner, M. Bräuninger, B. Paviet-Salomon, L. Barraud, R. Monnard, J. P. Seif, A. Tomasi, Q. Jeangros, A. Hessler-Wyser, S. De Wolf, M. Despeisse, S. Nicolay, B. Niesen and C. Ballif, *Adv. Energy Mater.*, 2018, **8**, 1701609.

333 F. Sahli, J. Werner, B. A. Kamino, M. Bräuninger, R. Monnard, B. Paviet-Salomon, L. Barraud, L. Ding,

6932 | *Energy Environ. Sci.*, 2025, **18**, 6899–6933

This journal is © The Royal Society of Chemistry 2025

J. J. Diaz Leon, D. Sacchetto, G. Cattaneo, M. Despeisse, M. Boccard, S. Nicolay, Q. Jeangros, B. Niesen and C. Ballif, *Nat. Mater.*, 2018, **17**, 820–826.

334 W. Yoon, D. Scheiman, Y. W. Ok, Z. Song, C. Chen, G. Jernigan, A. Rohatgi, Y. Yan and P. Jenkins, *Sol. Energy Mater. Sol. Cells*, 2020, **210**, 110482.

335 Z. Yang, A. Rajagopal, S. B. Jo, C. C. Chueh, S. Williams, C. C. Huang, J. K. Katahara, H. W. Hillhouse and A. K. Y. Jen, *Nano Lett.*, 2016, **16**, 7739–7747.

336 K. Makita, Y. Kamikawa, H. Mizuno, R. Oshima, Y. Shoji, S. Ishizuka, R. Müller, P. Beutel, D. Lackner, J. Benick, M. Hermle, F. Dimroth and T. Sugaya, *Prog. Photovoltaics Res. Appl.*, 2021, **29**, 887–898.

337 K. Makita, H. Mizuno, T. Tayagaki, T. Aihara, R. Oshima, Y. Shoji, H. Sai, H. Takato, R. Müller, P. Beutel, D. Lackner, J. Benick, M. Hermle, F. Dimroth and T. Sugaya, *Prog. Photovoltaics Res. Appl.*, 2020, **28**, 16–24.

338 S. Mirabella, S. Cosentino, A. Gentile, G. Nicotra, N. Piluso, L. V. Mercaldo, F. Simone, C. Spinella and A. Terrasi, *Appl. Phys. Lett.*, 2012, **101**, 11911.

339 H. Mizuno, K. Makita and K. Matsubara, *Appl. Phys. Lett.*, 2012, **101**, 191111.

340 E. Yablonovitch, T. Sands, D. M. Hwang, I. Schnitzer, T. J. Gmitter, S. K. Shastry, D. S. Hill and J. C. C. Fan, *Appl. Phys. Lett.*, 1991, **59**, 3159–3161.

341 H. Mizuno, K. Makita, T. Mochizuki, T. Tayagaki, T. Sugaya and H. Takato, *ACS Appl. Energy Mater.*, 2020, **3**, 3445–3453.

342 C. O. Ramírez Quiroz, G. D. Spyropoulos, M. Salvador, L. M. Roch, M. Berlinghof, J. Darío Perea, K. Forberich, L. I. Dion-Bertrand, N. J. Schrenker, A. Classen, N. Gasparini, G. Chistiakova, M. Mews, L. Korte, B. Rech, N. Li, F. Hauke, E. Spiecker, T. Ameri, S. Albrecht, G. Abellán, S. León, T. Unruh, A. Hirsch, A. Aspuru-Guzik and C. J. Brabec, *Adv. Funct. Mater.*, 2019, **29**, 1901476.

343 M. Schnabel, H. Schulte-Huxel, M. Rienäcker, E. L. Warren, P. F. Ndione, B. Nemeth, T. R. Klein, M. F. A. M. Van Hest, J. F. Geisz, R. Peibst, P. Stradins and A. C. Tamboli, *Sustainable Energy Fuels*, 2020, **4**, 549–558.

344 C. Luderer, C. Reichel, F. Feldmann, M. Bivour and M. Hermle, *Appl. Phys. Lett.*, 2019, **115**, 182105.

345 M. K. Siddiki, J. Li, D. Galipeau and Q. Qiao, *Energy Environ. Sci.*, 2010, **3**, 867–883.

346 G. Y. Margulis, B. E. Hardin, I.-K. Ding, E. T. Hoke, M. D. McGehee, G. Y. Margulis, I. Ding, E. T. Hoke, M. D. McGehee and B. E. Hardin, *Adv. Energy Mater.*, 2013, **3**, 959–966.

347 P. Lö, M. Stuckelberger, B. Niesen, J. Jere, J. Werner, M. Filipič, S.-J. Moon, J.-H. Yum, M. Topič, S. De Wolf and C. Ballif, *J. Phys. Chem. Lett.*, 2015, **6**, 66–71.

348 Q. Lin, A. Armin, R. Nagiri, P. Burn and P. Meredith, *Nat. Photonics*, 2015, **9**, 106–112.

349 S. Khelifi, G. Brammertz, L. Choubrac, M. Batuk, S. Yang, M. Meuris, N. Barreau, J. Hadermann, H. Vrielinck, D. Poelman, K. Neyts, B. Vermang and J. Lauwaert, *Sol. Energy Mater. Sol. Cells*, 2021, **219**, 110824.

350 D. Atsu, I. Seres, M. Aghaei and I. Farkas, *Renew Energy*, 2020, **162**, 285–295.

351 E. Annigoni, A. Virtuani, M. Caccivio, G. Friesen, D. Chianese and C. Ballif, *Prog. Photovoltaics Res. Appl.*, 2019, **27**, 760–778.

352 J. Kettle, M. Aghaei, S. Ahmad, A. Fairbrother, S. Irvine, J. J. Jacobsson, S. Kazim, V. Kazukauskas, D. Lamb, K. Lobato, G. A. Mousdis, G. Oreski, A. Reinders, J. Schmitz, P. Yilmaz and M. J. Theelen, *Prog. Photovoltaics Res. Appl.*, 2022, **30**, 1365–1392.

353 A. Ndiaye, C. M. F. Kébé, A. Charki, P. A. Ndiaye, V. Sambou and A. Kobi, *Sol. Energy*, 2014, **103**, 70–77.

354 A. Ndiaye, A. Charki, A. Kobi and C. Kébé, *Sol. Energy*, 2014, **103**, 70–77.

355 M. A. Munoz, M. C. Alonso-García, N. Vela and F. Chenlo, *Sol. Energy*, 2011, **85**, 2264–2274.

356 V. Sharma and S. S. Chandel, *Sol. Energy*, 2016, **134**, 32–44.

357 H. Yang, W. He, H. Wang, J. Huang and J. Zhang, *Sol. Energy Mater. Sol. Cells*, 2018, **187**, 61–68.

358 P. Hacke, K. Terwilliger, S. H. Glick, G. Perrin, J. H. Wohlgemuth, S. R. Kurtz, K. Showalter, J. D. Sherwin, E. Schneller, S. Barkaszi and R. M. Smith, *J. Photonics Energy*, 2015, **5**, 053083.

359 S. T. Zhang, M. Guc, O. Salomon, R. Wuerz, V. Izquierdo-Roca, A. Pérez-Rodríguez, F. Kessler, W. Hempel, T. Hildebrandt and N. Schneider, *Sol. Energy Mater. Sol. Cells*, 2021, **222**, 110914.

360 M. Lybbert, Z. Ghaemi, A. K. Balaji and R. Warren, *Renewable Sustainable Energy Rev.*, 2021, **144**, 111004.

361 D. Yu, Y. Yang, Z. Chen, Y. Tao and Y. Liu, *Opt. Commun.*, 2016, **362**, 43–49.

362 K. L. Jarvis and P. J. Evans, *Thin Solid Films*, 2017, **624**, 111–135.

363 F. Carigiet, C. J. Brabec and F. P. Baumgartner, *Renewable Sustainable Energy Rev.*, 2021, **144**, 111005.

This journal is © The Royal Society of Chemistry 2025

Energy Environ. Sci., 2025, **18**, 6899–6933 | 6933